

CHARACTERIZATION, BIOACTIVITY AND ANTIOXIDANT  
CAPACITY OF YTTRIUM AND CERIUM DOPED GLASS-CERAMICS

BY

LANA PLACEK

A THESIS

SUBMITTED TO THE FACULTY OF

ALFRED UNIVERSITY

IN PARTIAL FULFILLMENT OF THE REQUIREMENTS  
FOR THE DEGREE OF

DOCTOR OF PHILOSOPHY

IN

MATERIALS SCIENCE AND ENGINEERING

ALFRED, NEW YORK

MARCH, 2016

Alfred University theses are copyright protected and may be used for education or personal research only. Reproduction or distribution in part or whole is prohibited without written permission from the author.

Signature page may be viewed at Scholes Library, New York State College of Ceramics, Alfred University, Alfred, New York.

CHARACTERIZATION, BIOACTIVITY AND ANTIOXIDANT  
CAPACITY OF YTTRIUM AND CERIUM DOPED GLASS-CERAMICS

BY

LANA PLACEK

B.S. ALFRED UNIVERSITY (2010)

M.S. ALFRED UNIVERSITY (2012)

SIGNATURE OF AUTHOR \_\_\_\_\_

APPROVED BY \_\_\_\_\_

ANTHONY WREN, ADVISOR

\_\_\_\_\_  
ALEXIS CLARE, ADVISORY COMMITTEE

\_\_\_\_\_  
MATTHEW HALL, ADVISORY COMMITTEE

\_\_\_\_\_  
NATHAN MELLOTT, ADVISORY COMMITTEE

\_\_\_\_\_  
STEVEN TIDROW, CHAIR, ORAL THESIS DEFENSE

ACCEPTED BY \_\_\_\_\_

DOREEN D. EDWARDS, DEAN  
KAZUO INAMORI SCHOOL OF ENGINEERING

ACCEPTED BY \_\_\_\_\_

NANCY J. EVANGELISTA, ASSOCIATE PROVOST  
FOR GRADUATE AND PROFESSIONAL PROGRAMS  
ALFRED UNIVERSITY

## ACKNOWLEDGMENTS

Over the course of my graduate work there have been many people who have helped me reach this point beginning with Dr. Tony Wren who took me on as his first graduate student and I am proud to call my advisor. I have been fortunate to know Dr. Wren as a post-doc, where he was a mentor and great friend, through becoming a Professor and my advisor. He has created an environment within the BMES department that fosters independent problem solving, creativity, and comradery enabling me to grow as both a student and researcher. I would also like to thank my committee members: Dr. Hall, who began as my advisor when I arrived at Alfred University as an undergrad, and has since been an invaluable mentor over these many years, Dr. Alexis Clare, who was also a member of my MS committee, and Dr. Mellott, for their advice and guidance throughout the course of my project. I would also like to thank Katie Decker for making the entire process from entering the graduate program to thesis review and scheduling, immensely easier. She is amazing at her job and vital to the engineering department here at Alfred.

To everyone in the BMES group, past and present, particularly, Dr. Aisling Coughlan, and Dr. Tim Keenan, a friend with whom I have worked alongside my entire Alfred career, thanks for all the brainstorming, motivation and laughs we have shared along the way, I could not have done this without all your help. In addition to the help I received at school I have had a tremendous support and patience from my friends, both old and new, parents and siblings. You have all been completely amazing and have been there for me through the good and the bad, motivating me to be better and do more than I thought I was capable of.

# TABLE OF CONTENTS

	<u>Page</u>
Acknowledgments.....	iii
Table of Contents.....	iv
List of Tables .....	ix
List of Figures.....	x
Abstract.....	xiii
Chapter 1 - INTRODUCTION .....	1
1.1 The Spine and Spinal Injury.....	1
1.1.1. Vertebral Structure.....	1
1.1.2. Vertebral Composition.....	2
1.1.3. Maintaining Vertebra Integrity .....	4
1.1.4. Spinal Cord .....	5
1.1.5. Regenerative processes in the Spinal Cord.....	6
1.1.6. Traumatic Spine Injury .....	7
1.2 Silicate Bioactive Glass.....	12
1.2.1. Composition.....	13
1.2.2. Bioactivity.....	15
1.2.3. pH and Ion Release .....	16
1.2.4. Sintering of Bioactive Glasses .....	19
1.3 Surface Properties of Biomaterials and Cell Attachment.....	20
1.3.1. Surface Features.....	21
1.3.2. Surface Chemistry and Charge .....	21
1.4 Objective .....	21
Chapter 2 - Characterization of Y <sub>2</sub> O <sub>3</sub> and CeO <sub>2</sub> doped SiO <sub>2</sub> -SrO-Na <sub>2</sub> O glasses. ....	23

2.1	ABSTRACT .....	23
2.2	INTRODUCTION.....	24
2.3	EXPERIMENTAL .....	26
2.3.1.	Glass Synthesis .....	26
2.3.2.	Glass Characterization .....	27
2.4	RESULTS.....	30
2.4.1.	Particle Size Analysis .....	30
2.4.2.	X-Ray Diffraction (XRD).....	30
2.4.3.	Network Connectivity (NC).....	30
2.4.4.	Thermal Analysis .....	31
2.4.5.	Vickers Hardness (HV).....	33
2.4.6.	Magic Angle Spinning-Nuclear Magnetic Resonance (MAS-NMR).....	33
2.4.7.	X-ray Photoelectron Spectroscopy (XPS) .....	33
2.4.8.	Preliminary Cell Compatibility.....	39
2.5	DISCUSSION .....	39
2.6	CONCLUSION .....	45
Chapter 3 - Solubility, cytocompatibility and antioxidant capacity of Y <sub>2</sub> O <sub>3</sub> and CeO <sub>2</sub> doped SiO <sub>2</sub> -SrO-Na <sub>2</sub> O glasses.....		47
3.1	ABSTRACT .....	47
3.2	INTRODUCTION.....	48
3.3	EXPERIMENTAL .....	50
3.3.1.	Glass Synthesis .....	50
3.3.2.	Glass Solubility.....	50
3.3.3.	Glass Cytocompatibility.....	52
3.3.4.	Antioxidant Capacity .....	53

3.3.5.	Preliminary Cell Adhesion.....	54
3.4	RESULTS.....	54
3.4.1.	Scanning Electron Microscopy (SEM)/Energy Dispersive X-ray (EDX) ..	54
3.4.2.	Surface Area Analysis.....	54
3.4.3.	pH Analysis.....	54
3.4.4.	Ion Release.....	56
3.4.5.	Fibroblast and Osteoblast Viability .....	57
3.4.6.	Bacterial Inhibition .....	59
3.4.7.	Antioxidant Capacity .....	60
3.4.8.	Fibroblast Adhesion .....	61
3.5	DISCUSSION .....	62
3.6	CONCLUSION .....	66
Chapter 4 -	Effect of Crystallization on the Solubility and Antioxidant Potential of Y <sub>2</sub> O <sub>3</sub> and CeO <sub>2</sub> doped SiO <sub>2</sub> -SrO-Na <sub>2</sub> O glass-ceramics.....	68
4.1	ABSTRACT.....	68
4.2	INTRODUCTION.....	69
4.3	EXPERIMENTAL .....	70
4.3.1.	Glass Synthesis .....	70
4.3.2.	Thermal Analysis .....	71
4.3.3.	Disk Production .....	71
4.3.4.	X-Ray Diffraction (XRD) of A/S Disks .....	72
4.3.5.	Scanning Electron Microscopy (SEM).....	72
4.3.6.	ICP-OES Ion Release.....	73
4.3.7.	Antioxidant Capacity .....	74
4.4	RESULTS.....	74

4.4.1.	Thermal Analysis .....	74
4.4.2.	Shrinkage .....	75
4.4.3.	X-Ray Diffraction(XRD) and Scanning Electron Microscopy(SEM).....	75
4.4.4.	Ion-Release .....	81
4.4.5.	Antioxidant Capacity .....	83
4.5	DISCUSSION .....	85
4.6	CONCLUSION .....	90
Chapter 5 - Bioactivity of Y <sub>2</sub> O <sub>3</sub> and CeO <sub>2</sub> doped SiO <sub>2</sub> -SrO-Na <sub>2</sub> O glass-ceramics.....		91
5.1	ABSTRACT.....	91
5.2	INTRODUCTION.....	92
5.3	EXPERIMENTAL .....	94
5.3.1.	Disk Synthesis.....	94
5.3.2.	pH Analysis.....	95
5.3.3.	Inductively Coupled Plasma-Optical Emission Spectroscopy (ICP-OES). 95	
5.3.4.	Osteoblast Viability .....	96
5.3.5.	Bioactivity.....	97
5.3.6.	Cell Adhesion.....	97
5.4	RESULTS.....	97
5.4.1.	pH Analysis.....	97
5.4.2.	Inductively Coupled Plasma-Optical Emission Spectroscopy (ICP-OES). 98	
5.4.3.	Osteoblast Viability .....	100
5.4.4.	Bioactivity.....	100
5.4.5.	Cell Adhesion.....	101
5.5	DISCUSSION .....	102
5.6	CONCLUSION .....	114

Chapter 6 - Summary.....	116
6.1 BASIS & HYPOTHESIS.....	116
6.2 THESIS OBJECTIVES.....	116
6.3 THESIS CONCLUSIONS.....	116
6.3.1. Ch. 2 Characterization of Glasses.....	116
6.3.2. Ch. 3 Solubility Cytocompatibility & Antioxidant Capacity of Glasses ..	117
6.3.3. Ch. 4 Effect of Crystallization on Solubility & Antioxidant Potential .....	117
6.3.4. Ch. 5 Bioactivity and Cytocompatibility of Glass-Ceramics.....	118
6.4 FUTURE WORK.....	119
References.....	121

## LIST OF TABLES

Table 1-1.	45S5 Glass Composition.....	13
Table 2-1.	Glass Compositions (XPS Comp.) in mol%, Particle Size & Hardness.....	27
Table 2-2.	Network Connectivity (using XPS comp.) .....	36
Table 2-3.	High Resolution XPS Peak Locations .....	36
Table 3-1.	Glass Compositions in mol% and Surface Area (SA) .....	50
Table 4-1.	Glass Compositions in mol%.....	71
Table 4-2.	PDF and Molecular Formulas (MF) for XRD Identified Phases .....	81
Table 5-1.	Glass Compositions in mol% and Characteristic Temperatures (°C).....	95

## LIST OF FIGURES

Figure 1-1. Spinal column and dermatome showing nerves associated with sensory and motor functions throughout the body. Adapted from Silva et al. <sup>3</sup> and Ellis. <sup>4</sup> .....	2
Figure 1-2. Vertical cross section of the spine. <sup>7</sup> .....	3
Figure 1-3. Microstructure of bone. Adapted from Rho et al. <sup>8</sup> and Sprio et al. <sup>12</sup> .....	4
Figure 1-4. Cross-section of the spinal cord and vertebra. <sup>1</sup> .....	6
Figure 1-5. (A) Microlesion (B) Contusive Lesion (C) Stab Lesion. Adapted from Silver et al. <sup>24</sup> .....	8
Figure 1-6. Ternary phase diagram of the soda-lime-silica system. Region A - glasses capable of bond formation with both hard and soft tissues. Region B - bioactive glasses. Region C - inert glasses where the high former content prevents reaction in physiological fluids. Region D - glasses that resorb within 30 days in the body. Region E - glasses that are not practical due to the high modifier content. From Tilocca. <sup>87</sup> .....	14
Figure 1-7. Sequence of interfacial reactions for bonding between tissue and bioactive glass-ceramics. <sup>95,97</sup> .....	16
Figure 2-1. X-ray scattering of each glass powder. ....	31
Figure 2-2. (Left) Network connectivity from the molar concentrations given in Table 2-1. (Right) Glass transition temperature ( $T_g$ ) for each glass. ....	31
Figure 2-3. SDT curves for each glass with relevant temperatures labeled. Glass transition temperature ( $T_g$ ), Crystallization temperature ( $T_c$ ), Melting temperature ( $T_m$ ). ....	32
Figure 2-4. <sup>29</sup> Si MAS-NMR of each glass. ....	34
Figure 2-5. XPS survey scans of each glass. ....	35
Figure 2-6. High resolution scans of the Y 3d peak for yttrium containing glasses, <i>LY</i> , <i>HY</i> , and <i>YCe</i> . ....	37
Figure 2-7. High resolution scans of the Ce 3d peak for cerium containing glasses, <i>LCe</i> , <i>HCe</i> , and <i>YCe</i> . ....	37
Figure 2-8. High resolution scans of the O1s peak for <i>Con</i> , <i>YCe</i> , <i>HCe</i> and <i>HY</i> . ....	38
Figure 2-9. Bridging to non-bridging oxygen ratio as determined using O1s high res-XPS for <i>Con</i> , <i>YCe</i> , <i>HCe</i> and <i>HY</i> glasses. ....	39
Figure 2-10. SEM images of Schwann cells fixed on each polished glass surface at 200X. ....	40
Figure 3-1. SEM images of glass particles at 1000X and EDX generated oxides list. ....	55

Figure 3-2.	pH of liquid extracts from Y/Ce glass series over 1, 7 and 30 days incubation.....	56
Figure 3-3.	Ion release from each glass extract over 1, 7 and 30 days.....	57
Figure 3-4.	Fibroblast viability after incubation with glass extracts at 9%, 20% and 33% concentrations by volume over 1, 7 and 30 days. * indicates a significant difference ( $P < 0.05$ ) between the control Fibroblast population and the extract incubated populations.....	58
Figure 3-5.	Osteoblast viability after incubation with glass extracts at 9%, 20% and 33% concentrations by volume over 1, 7 and 30 days. * indicates a significant difference ( $P < 0.05$ ) between the control Osteoblast population and the extract incubated populations.....	59
Figure 3-6.	<i>E. coli</i> and <i>S. aureus</i> inhibition after incubation with glass extracts at 9% concentration by volume. * indicates a significant difference ( $P < 0.05$ ) between the control <i>E. coli</i> or <i>S. aureus</i> population and the extract incubated populations. ....	60
Figure 3-7.	Antioxidant capacity of glass extracts relative to Trolox <sup>®</sup> . * indicates a significant difference ( $P < 0.05$ ) between time periods for each glass; † indicates non-significance between glasses. ....	61
Figure 3-8.	SEM images of Fibroblast cells after 24 hr incubation on <i>Con</i> , <i>HY</i> and <i>HCe</i> disks at 500X. ....	62
Figure 4-1.	Thermal treatment profile and processing temperatures for annealed and sintered disks. ....	73
Figure 4-2.	Weight change of PVA and glass-PVA powders up to 500°C. ....	75
Figure 4-3.	% shrinkage of disks after thermal treatment. ....	76
Figure 4-4.	XRD patterns and SEM images at 30X, 500X and high magnification of thermally treated <i>Con</i> disks. ....	77
Figure 4-5.	XRD patterns and SEM images at 30X, 500X and high magnification of thermally treated <i>HY</i> disks.....	78
Figure 4-6.	XRD patterns and SEM images at 30X, 500X and high magnification of thermally treated <i>YCe</i> disks. ....	79
Figure 4-7.	XRD patterns and SEM images at 30X, 500X and high magnification of thermally treated <i>HCe</i> disks. ....	80
Figure 4-8.	Si on release from each disk extracts over 1, 7, and 14 days.....	82
Figure 4-9.	Sr ion release from each disk extracts over 1, 7, and 14 days. ....	82
Figure 4-10.	Change in Na <sup>+</sup> content relative to SBF-only samples after 1, 7, and 14 day disk incubation. ....	83

Figure 4-11. Antioxidant capacity of disk particulate after thermal treatment and 7 day incubation in SBF. * indicates a significant difference ( $P < 0.05$ ) between time periods and sample type for each glass. ....	84
Figure 4-12. Antioxidant capacity of disk extracts relative to Trolox <sup>®</sup> . * indicates a significant difference ( $P < 0.05$ ) between time periods for each sample. ....	85
Figure 5-1. pH of liquid extracts from Y/Ce disk series over 1, 7 and 14 days incubation.....	98
Figure 5-2. % Ca ions remaining in solution after 1, 7, and 14 day disk incubation relative to SBF-only samples.....	99
Figure 5-3. % P ions remaining in solution after 1, 7, and 14 day disk incubation relative to SBF-only samples.....	99
Figure 5-4. Osteoblast viability after incubation with disk extracts at 9%, 20% and 33% concentrations by volume over 1, 7 and 14 days. * indicates a significant difference ( $P < 0.05$ ) between time periods for each sample. ....	100
Figure 5-5. SEM images of t = 0, 1, and 14 day SBF incubated disks at 500X and EDX generated oxides list for <i>Con</i> .....	103
Figure 5-6. SEM images of t = 0, 1, and 14 day SBF incubated disks at 500X and EDX generated oxides list for <i>HY</i> .....	104
Figure 5-7. SEM images of t = 0, 1, and 14 day SBF incubated disks at 500X and EDX generated oxides list for <i>YCe</i> .....	105
Figure 5-8. SEM images of t = 0, 1, and 14 day SBF incubated disks at 500X and EDX generated oxides list for <i>HCe</i> . ....	106
Figure 5-9. Optical images at 4X of 14 day incubated disk-Osteoblast interface after 24 hr incubation.....	107
Figure 5-10. Optical images at 4X of 14 day incubated disk-Schwann interface after 24 hr incubation. ....	108
Figure 5-11. SEM images at 1kX after disk incubation with Osteoblasts and fixation.....	109
Figure 5-12. SEM images at after disk incubation with Schwann cells and fixation.....	110

## ABSTRACT

Compositional modifications of traditional bioactive glasses were investigated to address adversity associated with the biological response after spinal cord injury (SCI); specifically the accumulation of calcium (Ca) and subsequent generation of reactive oxygen species (ROS). Studies have shown yttria and ceria to have direct antioxidant scavenging capacity and provide neuroprotection under *in vitro* conditions of oxidative stress. Therefore in this work, Ca is replaced by strontium (Sr) and yttrium (Y) and cerium (Ce) are incorporated at the expense of sodium (Na) in a  $0.52\text{SiO}_2\text{-}0.24\text{SrO}\text{-}(0.24\text{-}x)\text{Na}_2\text{O}\text{-}x\text{MO}$  (where  $x = 0.08$ ;  $\text{MO} = \text{Y}_2\text{O}_3$  and  $\text{CeO}_2$ ) glass series. The structure, dissolution behavior and antioxidant capacity are first investigated for the glass series where excessive dissolution was found to cause fibroblast and osteoblast toxicity. In an effort to reduce dissolution, thermal processing was employed to create a glass-ceramic series. The glass-ceramic structure reduced solubility and eliminated osteoblast toxicity while maintaining a degree of ROS scavenging capacity. Studies evaluating the glass-ceramic bioactivity and *in vitro* observation of the interaction of these glass-ceramics with osteoblast and Schwann cells were then completed.

# CHAPTER 1 - INTRODUCTION

Spinal cord injury (SCI) is the combination of primary physical damage to the nerve tissue and secondary biochemical processes that can cause further damage. These processes often result in loss of motor and sensory functions where current methods of treatment produce minimal recovery of these faculties. This work focuses on the development of a glass/glass-ceramic to be used in nerve conduits or as scaffolds that can stabilize the injury site and deliver therapeutic factors aimed at reducing the adverse effects associated with the biological SCI response to encourage and/or guide the regeneration of nerves for successful reconnection and restoration of function. The proposed methodology in this research involves the development and characterization of calcium (Ca) free bioactive glass and glass-ceramics containing yttrium (Y) and cerium (Ce). Y and Ce have known neuro-protective properties which may be imparted within the glass-ceramics.

## 1.1 The Spine and Spinal Injury

The spine consists of the spinal column and the spinal cord. Vertebral bones, connective tissues, and muscles of the spinal column serve as the main physical support for the body and provide protection for the spinal cord.<sup>1,2</sup> Nerves composing the spinal cord branch from each vertebra to allow exchange of motor and sensory information between the brain and specific regions of the body.<sup>1</sup> Upon injury both the vertebrae and nerves may be compromised. Loss of motor and/or sensory function with injury often occurs at and below the affected vertebrae; the regions of the body associated with the spinal nerves at each are shown in Figure 1-1.<sup>2</sup>

### 1.1.1. Vertebral Structure

The 29 individual vertebrae of the spinal column each have two segments, the vertebral body, anteriorly located, and the neural arch with spinous and transverse processes posteriorly.<sup>1</sup> These processes serve as sites for muscle and ligament attachment. Adjacent vertebral bodies (depicted in Figure 1-2) are connected by intervertebral disks which serve to transmit shifts in body weight with anterior and posterior longitudinal ligaments serving to support and stabilize the disk.<sup>2</sup> Posteriorly,

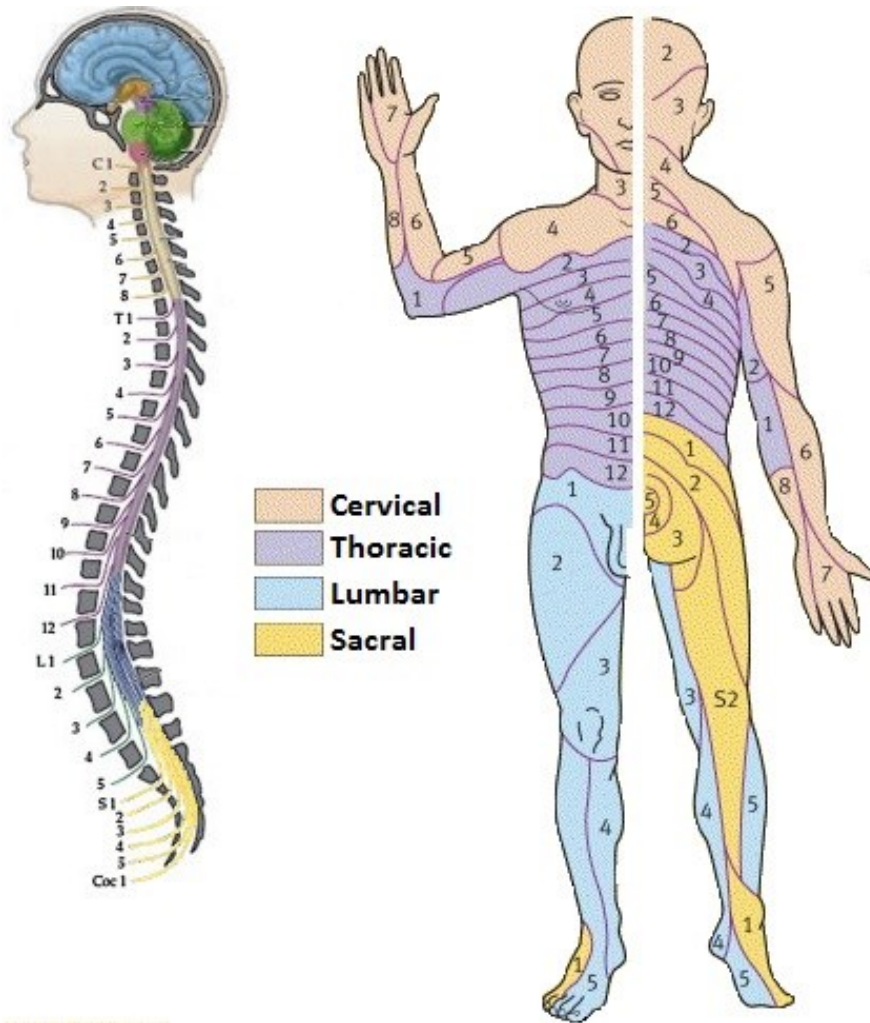


Figure 1-1. Spinal column and dermatome showing nerves associated with sensory and motor functions throughout the body. Adapted from Silva et al.<sup>3</sup> and Ellis.<sup>4</sup>

the neural arch features various facets, serving as synovial joints, and connecting ligaments between adjacent vertebrae.<sup>1</sup> Stacked vertebrae produce a continuous vertebral foramen (spinal canal) and aligned notches that form the intervertebral foramen to house the spinal cord and spinal nerves exiting the spinal column, respectively.<sup>1,2</sup>

### 1.1.2. Vertebral Composition

Chemically, bones are composed of two main phases: amorphous carbonated calcium phosphate that, when crystallized, is commonly referred to as hydroxyapatite (HA), and collagen molecules.<sup>5,6</sup> HA is the mineral phase of bone and consists primarily of calcium (Ca) and phosphate (P). It is formed in small needle or plate like

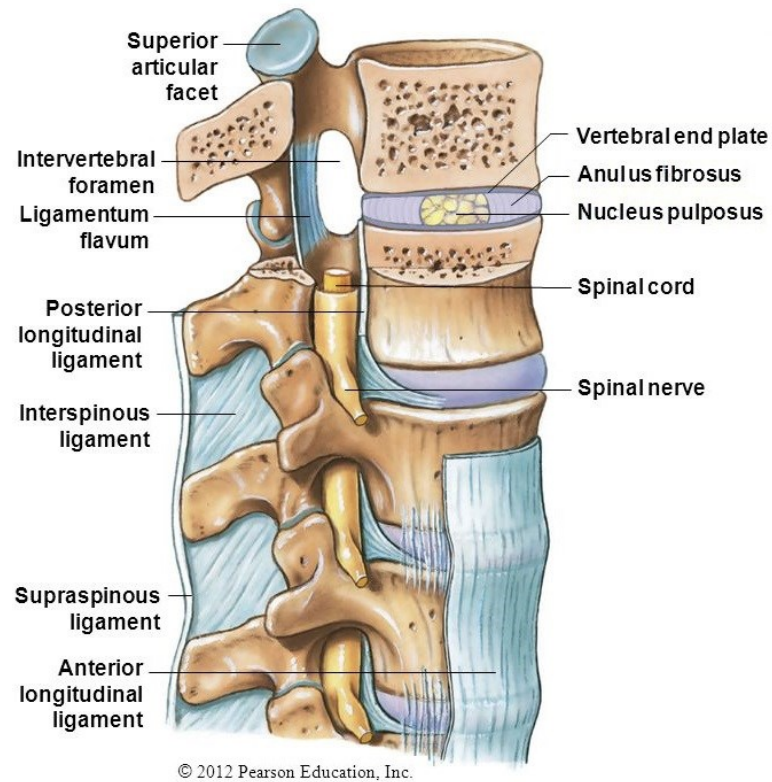


Figure 1-2. Vertical cross section of the spine.<sup>7</sup>

crystals depending on the type, location and load conditions of the bone being formed.<sup>6,8</sup> The size of the crystals can range from 200 Å - 50 nm during formation.<sup>8,9</sup> Collagen is the primary organic phase of bone and serves as the nucleation site for the HA crystals and as the matrix that tightly binds them together.<sup>10</sup> Figure 1-3 shows the nanostructure of the collagen-crystal composite, where the crystals are formed along the individual collagen molecules, and the progression of packing to form a collagen fiber.<sup>8</sup> The collagen fibers form sheets that make up the microstructure of bone; these sheets are called lamellae and are the base material for both cortical bone and cancellous bone.<sup>10</sup> Cortical bone or compact bone is the dense, outer layer of most bones. Lamellae in cortical bone are layered in concentric circles with the direction of collagen fibers at varied angles to those of the previous sheets.<sup>8</sup> Spaces between the lamellae layers are referred to as lacuni and are occupied by osteocytes. Osteocytes are mature bone cells that monitor and maintain the protein and mineral content of bone matrix by communication through canaliculi (small canals between lacuni).<sup>11</sup> The layered lamellae

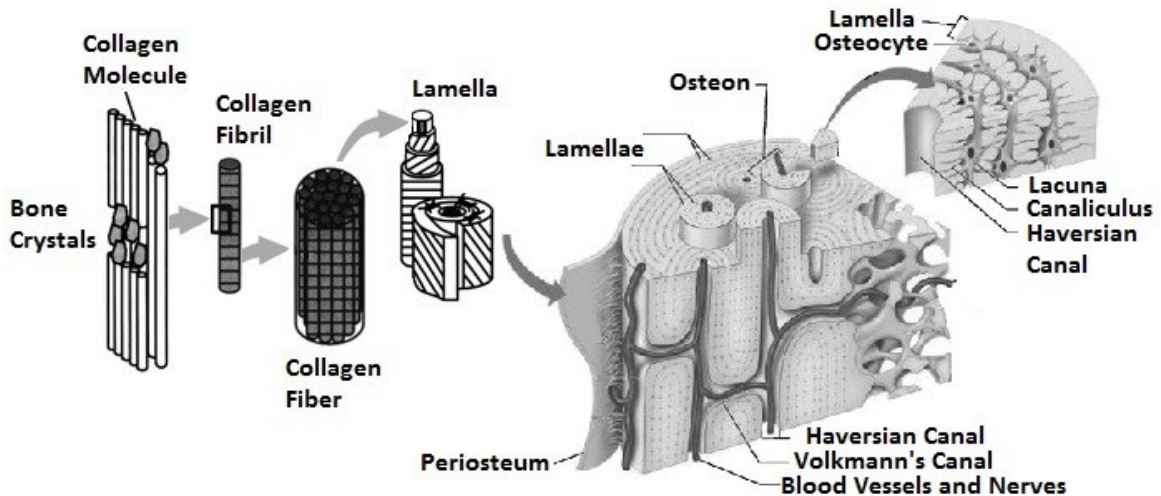


Figure 1-3. Microstructure of bone. Adapted from Rho et al.<sup>8</sup> and Sprio et al.<sup>12</sup>

and associated osteocytes are known as osteons. Osteons form around a central canal or haversian canal that run longitudinally along the load-bearing direction and contain the bone tissue's blood supply and nerves. Perpendicular to the haversian canals are the volkmann's canals that connect the various haversian canals and the bone center. This network of canals allows the blood supply and nerves to run throughout the bone tissue and marrow. Cancellous or spongy bone does not possess the density and strength of cortical bone but still provides support. Cancellous bone is the porous interior of bone which reduces weight, and can help absorb transverse loads which might otherwise cause fracture. It is formed from lamellae that roll upon themselves, still allowing for osteocyte residence, and interconnect with one another to form a trabecular network.<sup>8,11</sup> The outer cortical tissue in combination with the interior cancellous tissue allows for a balance between strength and weight to create bones that are both load bearing and light weight.

### 1.1.3. Maintaining Vertebra Integrity

Bones are constantly being regenerated to maintain an optimal ratio between strength and weight. This occurs through a process of resorption and re-mineralization. When osteocytes on the surface of the bone detect the need for remodeling they release factors such as the receptor activator for nuclear factor K (RANK) to recruit osteoclasts.<sup>13</sup> Osteoclasts are bone resorption cells derived from monocyte/macrophage cells and activated by the RANK pathway. Once recruited, osteoclasts will attach to the bone

surface and release collagenase, among other degradation enzymes to dissolve the bone at the site.<sup>11,14</sup> As the osteoclasts disperse, the cavity they created in the bone surface will be populated by the surrounding osteocytes that have since differentiated into osteoblasts.<sup>13</sup> Osteoblasts reform the collagen and re-mineralize to initiate new bone formation at the remodeling site. Once the site is saturated with Ca-PO<sub>4</sub> molecules the nucleation and growth of hydroxyapatite crystallites is dependent on a variety of factors, some of which are believed to be non-collagenous proteins (osteocalcin, osteopontin, osteonectin, and sialoprotein) of the bone matrix.<sup>15,16</sup> This process also allows bone to repair after injury, given that the site is stabilized and continued damage from bone fragments or abrasion is minimal.

#### **1.1.4. Spinal Cord**

As mentioned, the spinal cord (depicted in Figure 1-4) occupies the vertebral foramen (spinal canal) within the vertebral column, which provides an initial level of protection.<sup>2</sup> Secondary protection is afforded through the three meninges where the first, dura mater, is separated from the bone by the epidural space containing fat and vertebral veins.<sup>1</sup> The dura mater lines the skull and spinal nerves in the intervertebral foramen and is continuous to the fused sacral vertebrae. Between the dura mater and the second membrane, the arachnoid mater, is the subdural space which can accommodate blood after injury or byproducts from an immune response.<sup>1</sup> The subarachnoid space containing cerebrospinal fluid surrounds the spinal cord and brain buffered only by the third membrane, the pia mater. The pia mater and spinal cord ends at the L2 vertebra becoming a mass of nerve roots in the subarachnoid space to the coccyx.<sup>1</sup> The spinal cord itself is composed of two regions (depicted in Figure 1-4 and identified in Figure 1-5) the inner grey matter and surrounding white matter. The color differential arises from the un-myelinated nuclei of the grey matter nerve cell bodies and the myelinated extended axons of nerve tissue found in the white matter, and in turns corresponds to functional differences.<sup>1</sup> While the grey matter is responsible for senses and muscle control, the white matter is necessary to convey these messages throughout the body due to the lack of extended axons in grey matter. The axons of white matter are also responsible for monitoring and maintaining homeostasis through unconscious mechanisms such as temperature, heart rate, digestion and hormone release.<sup>1</sup>

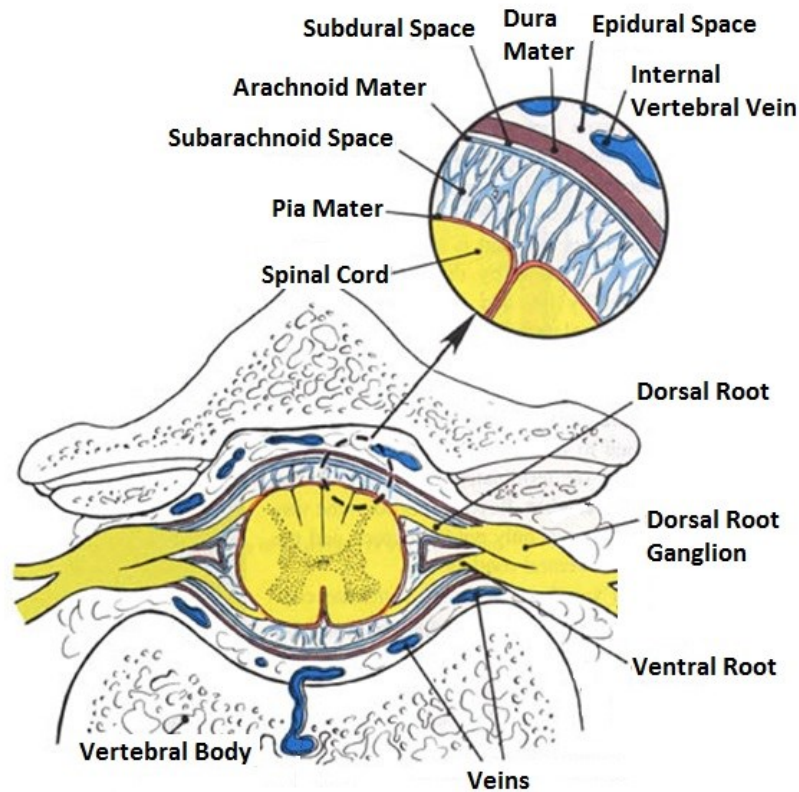


Figure 1-4. Cross-section of the spinal cord and vertebra.<sup>1</sup>

### 1.1.5. Regenerative processes in the Spinal Cord

Regenerative capabilities in the central nervous system (CNS) are inherently limited as nerve cells do not divide nor are they created through differentiation processes.<sup>17-20</sup> This requires the close monitoring of the Cerebral Spinal Fluid (CSF) and spinal cord by microglial cells which serve as the CNS immune system. The blood-brain barrier inhibits both antibodies and infectious agents from entering the CSF, however if the barrier is compromised, microglial cells are the last line of defense. Therefore, microglial cells constantly monitor the neuronal environment for signs of infection and damage and will act to neutralize the aberrant molecules or agents.<sup>1</sup> If a problem is detected they signal an inflammatory response and serve to eliminate the infectious agents or debris and subsequently deactivate the inflammatory response.<sup>17,21</sup> Through maintenance of the CSF and action of microglial cells the neuronal environment can be preserved to allow proper nerve function throughout a lifetime. However, if infection,

degenerative disease or injury physically compromises the nerves, recovery can only be achieved through existing nerve regeneration and reconnection.<sup>17</sup>

### **1.1.6. Traumatic Spine Injury**

Sudden traumatic events including motor vehicle accidents (38%), falls (30%), violence (14%), and sports injury (9%), are the primary causes of spinal damage.<sup>22,23</sup> Injuries limited to the vertebra can heal over time, often requiring immobilization or surgery to remove or repair the damaged bone tissue, which can lead to recovery of structural integrity, with the possibility of some loss of spinal flexion.<sup>23</sup> However, if the spinal cord is impacted, both mobility and sensory functions can be lost where 45% of individuals with SCI experience incomplete tetraplegia (paralysis of all four limbs or entire body below the neck), 21% experience incomplete paraplegia (paralysis of the legs and lower body) and 34% experience either complete para/tetraplegia.<sup>22</sup>

#### *1.1.6.1. Primary Spinal Damage*

The spinal cord is encased in the spinal column and contains a few interfacial layers between the nerve tissue and the inner vertebra. Thus, the vertebrae will be the first impacted when experiencing compression, contusion, shear, distraction and dislocation forces resulting from trauma and may or may not be able to sustain them without damage.<sup>24</sup> While injury to the vertebrae does not have to be significant for SCI to occur, computerized tomography (CT) and magnetic resonance imaging (MRI) scans show it is associated with 79% of SCIs. Common spinal column injuries associated with SCIs are minor fractures 10% (including compression fractures), dislocations 45%, and burst fractures 30% (bone fragments).<sup>23</sup> Besides incidents of trauma, general age related wearing of the disks including: disk dehydration, shrinkage, bone spurs, or osteoarthritis are other physical indicators that have been linked to SCI.<sup>23</sup> These mechanisms which compromise the structural integrity of the vertebrae often translates to physical damage of the spinal cord. Common SCI injuries result from compression, impact/projectile, laceration, and shearing of the nerve tissue or its protective mater with varying degrees of severity (Figure 1-5).<sup>23,24</sup>

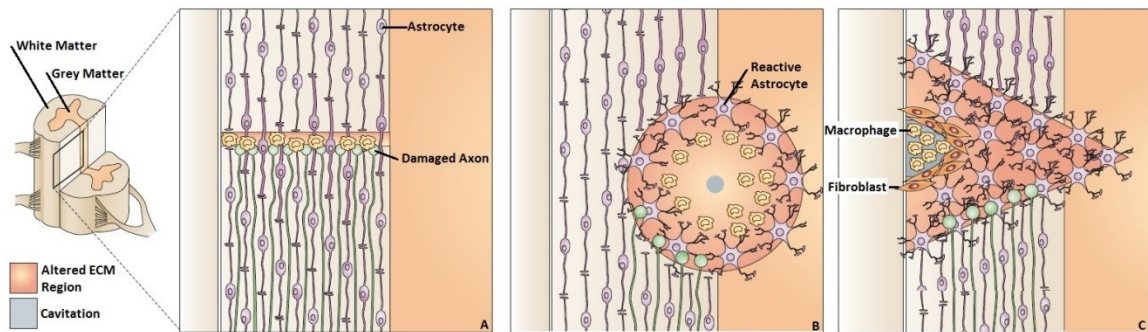


Figure 1-5. (A) Microlesion (B) Contusive Lesion (C) Stab Lesion. Adapted from Silver et al.<sup>24</sup>

### 1.1.6.2. Neurological Response

Shortly after a traumatic spinal injury biochemical cascades begin to first notify damage has occurred, and subsequently to mediate repair. The initial cell response is dependent on calcium (Ca). Damaged axons are no longer able to maintain the intracellular concentration gradient of Ca and thus an influx of Ca occurs. This influx triggers a retrograde signal to the soma<sup>25</sup> to initiate the mitogen-activated protein kinase (MAPK) pathway, specifically dual leucine kinase-1 (DLK-1), essential for growth cone formation and regeneration.<sup>26,27</sup> Secondary signals are delivered to the cell body that perceives axonal damage has occurred by transmission of an array of proteins. Proteins including  $\beta$ 1-importin, Map kinase ERK, CREB2, RanBP1, Smads, c-Jun, NH2-terminal kinase (JNK), JNK signaling molecules, and ATF3,<sup>21</sup> are responsible for providing secondary information about the location of the damage or activating genes to code for regenerative proteins. Outside of the cell, these signaling protein factors initiate the body's inflammatory response and glial cell activation. Thus the bio-chemical and cellular processes initiate in an effort to repair damage to the neuronal tissue in the spinal cord.<sup>28</sup> These secondary processes commonly induce edema, ischemia, inflammation, excitotoxicity (Ca mediated),<sup>29</sup> loss of ionic homeostasis/fluid-electrolyte imbalance, excessive cytokine release and generation of radical oxygen species (ROS) (through glutamate, aspartate, iron<sup>28,30</sup> and lipid peroxidation), which can result in further damage to the affected tissues or necrosis. In addition, severe damage involves the inflow of blood containing monocytes, lymphocytes, and inflammatory mediators. While these

processes occur as a means to heal damaged nerve tissue regeneration from surviving cells can be significantly limited as a result. One example is the balance between the inflammatory cytokines localized near the neuronal cell body which support axonal growth,<sup>31</sup> and the suppressor of cytokine signaling (SOCS) proteins. SOCS proteins are key mediators of the inflammatory response, however, in their role, also suppress cytokines promoting axonal growth.<sup>32</sup> In addition to the inflammatory response, activation of microglia and astrocytes in the damaged tissue leads to the formation of scar tissue, referred to as the glial scar which serves as a physical impediment to reconnection of nerves. Other physical aspects affecting the reconnection of nerves is the structure and composition of the extracellular matrix (ECM) produced, where inherent differences between the new and old may not properly support and guide the regenerating axon.<sup>18,33</sup> These biochemical and physical responses to SCI result in the progressive loss of neurons and oligodendroglial cells proximal to the injury site with ensuing axonal demyelination leading to degeneration of the axon at the site of severance and cell death.<sup>33-37</sup> Ultimately the ability of spinal nerves to regenerate depends upon initial survival and the ability to express growth-related genes, the availability of neurotropic factors, the presence of growth inhibiting/apoptosis inducing molecules, and the characteristics of the glial scar and ECM.<sup>24</sup>

#### *1.1.6.3. Current Treatment Methods*

Current methods addressing SCI focus on pharmaceuticals, neurotrophic factors, cell delivery, grafts and conduits providing a combination of therapies. However, over distances greater than 5 cm these methods show only minor improvements, reconnection does not often occur properly, and sensory or motor function is not recovered.

##### *Pharmaceuticals:*

In an attempt to correct these secondary mechanisms of spinal cord damage after injury, many pharmaceuticals have been evaluated. The default standard of care is methylprednisolone sodium succinate (MPSS) which is given in high doses within 3 hours of injury, though studies have shown that beneficial effects are modest.<sup>18,23</sup> MPSS is a corticosteroid which is widely known for its neuro-protective properties including antioxidant properties, enhancement of spinal cord blood flow, reduction of calcium influx, attenuated lipid peroxidation and reduced posttraumatic axonal die back.

However, studies by Bracken et al. only show MPSS to support improved neurological function between 6 weeks and 6 months, at a year the function was not improved compared to the placebo group.<sup>38,39</sup> Other treatments include inhibition of myelin-associated inhibitory molecules (MAIM) that have been shown to collapse axonal growth cones.<sup>40</sup> There have been multiple factors investigated with the aim of inhibiting the MAIMs, one of the most studied being the antibody IL-1, shown to effectively neutralize the MAIM inhibitory effect.<sup>41,42</sup> In a clinical trial by Fehlings et al., Cethrin, a protein based MAIM inhibitor reported no significant side effects and 30% of patients recovered sensory and some motor function below the level of injury.<sup>43</sup> Another significant inhibitory factor of axonal regeneration is the glial scar consisting of reactive astrocytes, microglia/macrophages, and ECM molecules, including chondroitin sulfate proteoglycans (CSPGs) that vary greatly in number and composition, and thus biological activity.<sup>28</sup> Multiple studies have documented the inhibitory effect of the CSPGs on axonal regeneration and others have suggested their removal attenuates this inhibition. Chondroitinase ABC has been investigated regarding its ability to degrade the CSPGs and found to potentially enable motor and sensory function recovery in the damaged spinal cord of rats and cats in studies by Bradbury et al. and Tester et al., respectively.<sup>44,45</sup> Other pharmacotherapy treatments that have drawn favorable attention include ganglioside GM-1 (glycolipids found to promote neural repair and functional recovery),<sup>46</sup> minocycline (inhibits apoptosis associated with human neurological diseases and attenuates secondary injury in SCI in animal models),<sup>47,48</sup> estrogen,<sup>49</sup> and the neuroimmunophilin ligand (improved motor function and long distance nerve regeneration in rats).<sup>50</sup> However, these pharmaceutical therapies have not been proven significantly effective or reproducible in multiple studies, and independently are unable to encourage effective regeneration and reconnection of spinal cord nerves.

#### *Cell Delivery:*

Another area of significant interest in the treatment of SCI is the delivery of various types of cells to the injury site. In numerous studies, olfactory ensheathing cells (OECs), bone marrow stromal cells (BMSC), human embryonic stem cells, and specific astrocytes have shown potential to aid in regeneration of the spinal cord nerves. Transplantation of OECs into a region of incomplete SCI has been investigated for neuro-

protective behavior and axonal regeneration where a study by Woodhall et al. found that the OECs exhibit neuro-protective behavior, possibly by means of astrocyte modulation, reduction of proteoglycan expression, and release of numerous neurotropic factors.<sup>51</sup> In addition, OECs have been found to promote axonal regeneration and re-myelination.<sup>52,53</sup> BMSCs have shown inconsistent results when introduced to SCI sites, however, a study by Osada et al. showed the combination of BMSCs with granulocyte colony-stimulating factor (G-CSF) and stem cell factors (SCF) enhances motor function recovery in mice.<sup>54</sup> In another study, 6 of 20 patients receiving autologous bone marrow transplant to the location of complete spinal cord transection experienced improved sensory and motor function after 3 months.<sup>55</sup> As previously discussed, the glial scar and associated cells can inhibit axonal growth and reconnection, however, specific astrocytes of this group have been shown to be advantageous.<sup>24</sup> Reactive astrocytes that help form the glial scar can also release neurotrophic factors, reduce excitotoxic cell death, and in specific cases restrict the spread of inflammatory cells; though their efficacy is based on the specific astrocyte subtype.<sup>56,57</sup> The potential to use autologous cells to encourage regeneration and reconnection of nerve cells in the spinal cord provides a dynamic way to address the multiple factors associated with secondary damage, however graft and conduit therapies currently show the greatest potential for successful regeneration.

*Nerve Grafts, Conduits and Combination Therapies:*

Autologous nerve grafts of peripheral nerves have been consistently shown to provide a favorable environment for axon regeneration particularly when utilized with various growth factors, where a study by Tsai et al. with rats showed significant improvement of locomotor performance after complete spinal transection in the T vertebral region over a gap size of 4 mm. Another study conducted by Tadie et al. used autologous sural nerve tissue to bypass paraplegic damage at the T9 vertebral level by bridging from the spinal cord at T7/8 to the ventral roots in the L2-4 region enabling voluntary adductor and quadricep contractions within 8 months of the procedure.<sup>18,58,59</sup> Recently, autologous olfactory mucosal nerve tissue has shown potential to bridge 1 - 4 cm spinal lesions, specifically in a study by Lima et al. where 11 of 20 para/tetraplegic patients recovered sensory and varying degrees of motor function a year after surgery.<sup>60</sup> Nerve guide conduits (NGCs) also serve as a bridge for regenerating axons, bypassing the

physical impediments of the glial scar tissue. NGCs are typically composed of natural or biodegradable synthetic polymers and feature specific stiffness, swelling and permeability characteristics essential to prevent further axonal damage or degeneration.<sup>61</sup> In addition, porosity and surface engineering are also considered based on the optimum parameters for cell attachment and directional growth where studies reviewed by Madigan et al. suggest stiffness and porosity simulating that of the original tissue encouraged reconnection over a greater distance by improving cell migration through the NGC and stabilizing it within the spinal cord prior to degradation.<sup>61-63</sup> These works are supported through a study by Reynolds et al. implanting porous polymer NGCs into rats after complete spinal cord transection at the T10 level. New neural tissue growth and restoration of hindlimb locomotor function was observed through the 2 mm gap.<sup>63</sup> Surface engineering to create canals around 450  $\mu\text{m}$  in diameter and micron sized striations to guide regenerating axons through the conduit is also supported through studies by Khademhosseini et al. and Moore et al.<sup>64,65</sup> Similar to autologous grafts, delivery of neurotrophic factors and supporting cells within the NGC further improves regeneration.<sup>61,66,67</sup> The most successful NGCs to date are conduits with embedded neurotrophic factors that are time released creating a concentration gradient achieving successful regeneration over a distance of 2.5 cm.<sup>67</sup> Despite the extensive research efforts and advances, statistics show that fewer than 2% of SCI cases reach full recovery of sensory and motor function a year after the event, leading to the continued pursuit of a treatment that will enable successful regeneration and reconnection of nerves. A new direction for NGCs was suggested by Bunting et al., through the incorporation of bioactive glass fibers in a commercial NGC which performed as well as an autograft over a 5 mm gap.<sup>68</sup>

## **1.2 Silicate Bioactive Glass**

Bioactive glasses are defined by their capacity to react in physiological fluids and ultimately bond with living tissue. Silicate bioactive glasses, specifically fluoroaluminosilicates, found their first clinical uses in dental applications, however, they have since been developed for use as particulates, microspheres for drug delivery, dental/spinal cements/adhesives, coatings for orthopedic devices and sintered into bioceramic scaffolds.<sup>69-72</sup> The diversity of applications arises from the range of compositions and

specifically by modifying elements that can be accommodated in the silica network. The ability to incorporate different elements into the glass structure and their subsequent release into surrounding fluids and tissues can produce therapeutic effects in the surrounding tissues. Some of the most common elements included for their therapeutic benefits are fluoride (F), zinc (Zn), and strontium (Sr).<sup>73-75</sup> Initially used as dental materials, F was incorporated for its known benefits to the health and strength of teeth, this property was harnessed through the release of F<sup>-</sup> by the bioactive glass upon dissolution.<sup>71,76,77</sup> Zn was initially employed to replace aluminum (Al) in the glass network due to Al neurotoxicity. However, secondary advantages became clear, as in ionic form (Zn<sup>2+</sup>) it was found to aid in the combat of infections, reduce inflammatory response, and act as a fungicide.<sup>73,78-82</sup> Sr was introduced to produce an analogous effect to that of the osteoporosis drug strontium ranelate, where Sr<sup>2+</sup> is incorporated into bone in place of Ca<sup>2+</sup> and provides resistance to osteoclast activity.<sup>74,83</sup> While each of these elements has therapeutic benefits, they also alter the silicate network and thus the potential bioactivity, therefore a balance between composition and therapeutic potential must be maintained as glasses are developed for biomedical applications.

### 1.2.1. Composition

The first form of bioactive glass (45S5) was developed at the University of Florida in the 1960's by Professor Larry Hench and is known to partially degrade *in vivo*, resulting in a secure bond/tissue integration when implanted into the body.<sup>84</sup> 45S5 (composition shown in Table 1-1) is one of many bioactive glasses that can elicit this response in the body where the key compositional element is the SiO<sub>2</sub> content.<sup>68,85,86</sup> Other glasses in the soda-lime-silica system containing 45-60% SiO<sub>2</sub> were also found to be bioactive, the composition range for which is shown in the ternary diagram in Figure 1-6.

Table 1-1. 45S5 Glass Composition

45S5 Glass Composition (mol %)			
Former		Modifier	
<u>SiO<sub>2</sub></u>	<u>P<sub>2</sub>O<sub>5</sub></u>	<u>Na<sub>2</sub>O</u>	<u>CaO</u>
46.1	2.5	24.4	26.9

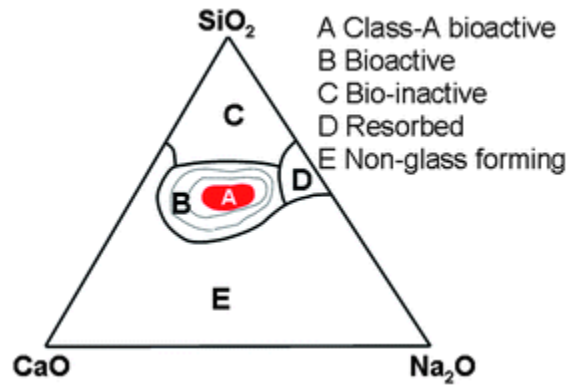


Figure 1-6. Ternary phase diagram of the soda-lime-silica system. Region A - glasses capable of bond formation with both hard and soft tissues. Region B - bioactive glasses. Region C - inert glasses where the high former content prevents reaction in physiological fluids. Region D - glasses that resorb within 30 days in the body. Region E - glasses that are not practical due to the high modifier content. From Tilocca.<sup>87</sup>

#### 1.2.1.1. Silica and Phosphate

Silica is the primary glass former in silica based bioactive glasses. Adjacent silica tetrahedra share one (bridging) O atom through Si-O-Si bonding and form a random network through variation in the angle of this bond which can range from  $120^\circ$  -  $180^\circ$ .<sup>88</sup> While any two tetrahedra may only share one O atom, each of the four O in a single tetrahedra may be linked to other tetrahedra which is referred to as a  $Q^4$  tetrahedral unit. Silica tetrahedra in bioactive glasses are typically found in  $Q^2$  and  $Q^3$  configurations where only two or three of the four O atoms in a tetrahedra are shared with other tetrahedra.<sup>89,90</sup> Other bioactive glass formers that adopt similar  $Q^2$  and  $Q^3$  configurations are  $P_2O_5$  and  $B_2O_3$ . The creation of  $Q^2$  and  $Q^3$  units occurs through the addition of network modifying elements, which provide additional O and charge compensation to the glass network.<sup>88</sup>

#### 1.2.1.2. Calcium & Sodium

Certain network modifiers such as Ca and sodium (Na) encourage silicate glasses to exhibit bioactivity. They serve as network modifiers due to their low valence and bond strengths.<sup>88</sup> When added to silicate glass they disrupt the network by increasing the ratio of O:Si where a ratio of 2 is that of  $SiO_2$  where all Os are shared between tetrahedra ( $Q^4$ )

and ratio of 4 allows each Si to bond with four individual O atoms ( $Q^0$ ) at a charge of -4. The charge is compensated by ionic association of the  $Ca^{2+}$  or  $Na^+$  ions with the non-bridging O atoms.<sup>88,91</sup> The reduction of Q species and presence of ionically associated Na and Ca ions is associated with an expansion of the network structure where the larger Ca and Na ions sit. The presence of these ionic species and expansion of the network helps create channels that are ideal for ion exchange which is an essential initial step for the bioactive cascade.<sup>91,92</sup>

### *1.2.1.3. Other Elements*

Since the discovery of 45S5 many additional elements have been introduced with the aim of manipulating the glass network to impart specific modifications in dissolution behavior, mechanical properties, and bioactivity.<sup>93,94</sup> Prediction of the role these elements may have in the glass can be made based on the valence, coordination number and associated field/bond strength where formers tend to have valences between 3 and 5 with coordination between 3 and 6, and modifiers with valences between 1 and 4 and coordination 4 or greater.<sup>88</sup> Some elements behave as intermediates adopting network forming or modifying roles based on the compositional ratios with other elements in the glass, such as Al.

### **1.2.2. Bioactivity**

Bioactive glasses are characterized by their capability to incite the formation of a bond with hard, and sometimes soft tissues when implanted into the body. For this to occur, the bioactive glass must proceed through a set of reactions, given in Figure 1-7, resulting in the formation of a hydroxyl-carbonate apatite (HCA) surface layer.<sup>95</sup> The reaction cascade initiates with exchange of hydrogen ions in the physiological fluid with modifying cations of the glass network. Thereby producing a characteristic increase in pH and alteration of the ionic content of the fluid.<sup>95</sup> This pH increase is indicative of the reactivity of the glass and can enhance the subsequent dissolution of the glass network and formation of silanols.<sup>96</sup> Once the surface silanols have polymerized creating a negatively charged surface, Ca (released from the glass or existing in the physiological fluid) will begin to deposit on the surface, and, in some cases, other cationic species released upon initial exchange with hydrogen ions. In order for the HCA layer to be

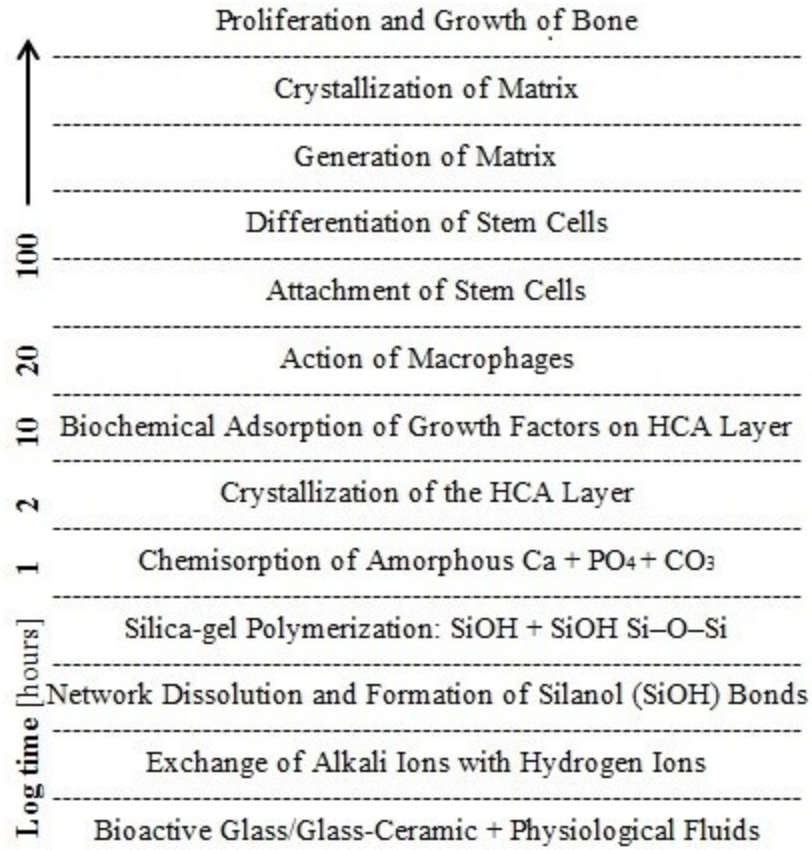


Figure 1-7. Sequence of interfacial reactions for bonding between tissue and bioactive glass-ceramics.<sup>95,97</sup>

biologically active the Ca/P ratio must mimic that of bone at 1.67.<sup>97,98</sup> Deposition of additional elements may affect the overall Ca/P ratio or the subsequent interaction with bone cells in a positive or negative way depending on the ionic species. However, if a Ca/P ratio similar to that of the inherent bone tissue is achieved, bone cells are recruited to the site and osteogenesis occurs.<sup>99</sup> This effectively bonds the bioactive glass to the regenerating tissue. Therefore striking a balance between bioactivity and ion release is sometimes vital.

### 1.2.3. pH and Ion Release

While network modifying ions enable glass reactivity, the ratio of formers to modifiers and ionic characteristics of each determine the rate of reactivity and dissolution behavior of the glasses. Dissolution of the glass network results in the release of ions which may act as therapeutic agents, which can be removed by biological processes, or,

in excess, cause cell toxicity related to specific ion levels or cumulative changes in pH.<sup>100</sup> Therefore, the balance between reactivity relating to bioactivity and ion release is vital to creating a biocompatible bioactive glass. Typical bioactive glasses consist of Si, Ca, and Na, for which the release and effects in the body have been extensively studied.<sup>101</sup> In this work Ca was exchanged for Sr, another common glass modifier, and Y and Ce are used as doping agents; while they are novel in bioactive glasses, a review of their known effects in the body follows.

#### 1.2.3.1. Silicon, Sodium and Strontium

In its elemental form Si is found as a trace element in connective tissue and skin. It is used in many products, foods, supplements, and is found in drinking water where it can be absorbed as orthosilicic acid and in turn is readily excreted through the kidneys, as such, it has not been found to accumulate in any organs or cause toxicity.<sup>102,103</sup> Orthosilicic acid in the body has been shown at concentrations of 10  $\mu\text{mol}$  to stimulate osteoblast differentiation and the production of type I collagen. In addition, multiple studies have shown the importance of Si associated with the formation of ECM proteins, such as osteopontin, metabolic processes of osteoblasts and calcification.<sup>104,105</sup> In addition, dietary supplements have been shown to improve bone mineral density in both rats and osteoporotic patients.<sup>101,106</sup> While *in vivo* studies have not reported toxicity, static *in vitro* studies have reported osteoblast toxicity at concentrations greater than 120  $\mu\text{g/ml}$ .<sup>107</sup> The toxicity of Si is likely a result of the Si concentration and pH, where above physiological pH the solubility of Si increases exponentially.<sup>108,109</sup>

Elementally Na accounts for 0.2% of the body composition and is ingested at a greater rate than any other element. Physiological levels vary but blood plasma maintains levels around 3600  $\mu\text{g/mL}$ .<sup>110</sup>  $\text{Na}^+$  is an essential ion throughout the body, necessary to maintain the ionic balance of physiological fluids, for proper nerve and muscle functioning, for effective signaling, and for multiple metabolic processes.<sup>111,112</sup> Extreme ingestion of sodium can damage the kidneys and adversely affect blood pressure, however cellular toxicity has not been observed as it is readily processed and excreted from the body.

Sr is another trace element in the body. It is present in grains, leafy vegetables and dairy products at moderate levels though can also be obtained through supplements or,

for osteoporosis patients, as strontium ranelate. Sr is incorporated into bone in place of Ca, when it is available in sufficient quantity, and impedes osteoclast activity thereby reducing the rate of bone resorption.<sup>74,83</sup> At excessive levels of Sr consumption (1000s ug/mL) bone development can be disrupted due to the excessive replacement of Ca in the tissue. In extracellular fluids Sr is typically found at  $\mu\text{M}$  concentrations though toxicity has not been reported since excess is excreted through the kidneys in the same manner as Ca.<sup>74,101,113,114</sup>

In this work the inclusion of Sr is not only for its therapeutic effect on bone but also drawing on the ionic similarities to Ca where  $\text{Sr}^{2+}$  is an ion of similar charge and ionic radius and thus serves as a network modifier within the bioactive glass in a nearly identical manner to  $\text{Ca}^{2+}$ , though a slight expansion of the network is commonly observed due to the slightly larger size.<sup>74</sup> This enables the replacement of Ca in the bioactive glass network without significant effect on typical properties associated with Ca in the glass. Through this compositional modification, a bioactive glass can be developed that addresses the  $\text{Ca}^{2+}$  attributed excitotoxicity and oxidative stresses imposed on nerve tissue after SCI.

#### *1.2.3.2. Yttrium and Cerium*

Neither Y or Ce have defined biological roles and, while there is limited information on the elemental toxicities of Y and Ce, it can be expected that as with heavy metals, accumulation in the body poses a significant risk of toxicity especially to the liver. However, in relation to this study the risk of toxicity was considered minimal based on the ion release reported by previous studies of Y and Ce bioactive glasses from which these compositions were formulated. These studies successfully incorporated Y and Ce into bioactive glasses at low concentrations, 3-6 mol% and 1-5 mol% respectively.<sup>115,116</sup> A study by Cacaina et al. evaluated Y containing bioactive glasses in simulated body fluid (SBF) up to 21 days and found that release was  $<0.03$  mg/L at each time period, for all glasses. It also showed Y to behave as a network modifier and decrease the reactivity based on the greater field strength of Y in comparison with other modifiers.<sup>115</sup> A study by Leonelli et al. substituted Ce into the 45S5 glass composition and evaluated the glass-forming potential and bioactivity of the successful glasses.<sup>116</sup> It was found that in homogeneous glasses the majority of Ce had a valence of III (attributed

to the high melting temperature which favors reduction of  $Ce^{4+}$  to  $Ce^{3+}$ ) and it behaved as a network modifier.<sup>116</sup> Similar to Y, Ce content retards glass degradation likely by the same mechanism and was not detected using ICP with a  $10^{-4}$  ppm detection limit.<sup>116</sup> Both these studies show that bioactivity decreased in glasses with increasing Y and Ce content, but the deposition of Y and Ce inclusive HCA layers did occur after 7-14 days incubation in SBF.<sup>115,116</sup> In other studies Y has been shown to encourage osteoblast adhesion and improve the electrical conductivity of the biomaterial which can aid in cell attachment and proliferation, and Ce salts can stimulate metabolic activities.<sup>117,118</sup> Therefore, considering these studies, the risk of toxicity is low, and biocompatibility as well as bioactivity is likely.

#### 1.2.4. Sintering of Bioactive Glasses

Thermal treatment of bioactive glasses may be employed to alter a number of properties, most commonly, to improve strength or reduce reactivity.<sup>119-121</sup> Upon thermal treatment glasses experience an initial phase of densification beginning just above the  $T_g$  through viscous flow which allows the formation of sintering necks between particles and proceeds to the onset of crystallization. During crystallization the viscosity increases preventing viscous flow and forestalling densification. As the temperature is increased the viscosity will again decrease and secondary densification will proceed, again, through viscous flow to  $T_m$ .<sup>122</sup> Heating rate during the sintering process has been shown to affect the characteristic temperatures where  $T_g$  and  $T_c$  increase with increasing heating rate and onset  $T_m$  decreases.<sup>122</sup> Particle size can also produce changes in the sintering behavior, where smaller particles with greater surface energy will sinter to a greater degree at lower temperatures in comparison with larger particles.<sup>123</sup> Identical heating rates and particle size distributions were used in this work to minimize variability.

Crystallization of typical bioactive glasses proceeds through surface crystallization and produces a sodium-calcium-silicate,  $Na_2Ca_2Si_3O_9$ .<sup>119,122,124</sup> While crystallization reduces reactivity and thus can in turn reduce bioactivity, multiple SBF studies have shown the  $Na_2Ca_2Si_3O_9$  phase does not eliminate bioactive potential.<sup>125-127</sup> Considering the similarities between the Ca and Sr ions previously discussed, it is reasonable to infer that primary phase generated for the  $SiO_2$ -SrO- $Na_2O$  control glass may be a similar  $Na_xSr_xSi_xO_x$  with bioactive potential. Additional phases generated in

the Y and Ce doped glasses are also of significant interest in this work. Though the effect of crystallization on bioactive glasses containing Y and Ce has not been studied, the basis of this concept stems from the study by Schubert et al. which found yttria and ceria nanoparticles to be neuroprotective.<sup>37</sup> Within this study, glutamate, a well-known stimulant for ROS production, was used with HT22 cells (rodent nerve cells) to introduce oxidative stress. It was shown that specific Y and Ce oxides provided the HT22 cells protection from ROS and that the toxicity and efficacy of the nanoparticles was size independent from 6-1000 nm; where each was non-toxic up to 200  $\mu\text{g/mL}$  with the exception of 1 $\mu\text{m}$  ceria particles which were toxic at concentrations greater than 20  $\mu\text{g/mL}$ .<sup>37</sup> In addition, the study suggested yttria nanoparticles were more effective at improving the viability of HT22 cells, in comparison with ceria, and exhibited a concentration dependent increase from 2 ng/mL-20  $\mu\text{g/mL}$ ; decreasing ROS by 50% at the highest dose.<sup>37</sup> Three mechanisms were proposed for the improved viability of the HT22 cells, and through focused experiments, ultimately attributed the effect to direct antioxidant capabilities of the oxides. The specific mechanism of this characteristic is not completely elucidated, though it is proposed that the cubic fluorite structure of the ceria, and the monoclinic B form of Y oxide (6 and 7 fold coordination) play a role.<sup>37</sup> The generation of these phases is unlikely considering the elemental composition of the glasses, however similar structures with any combination Si, Sr, or Na may show similar behavior, and address the ROS triggered necrosis of neuronal tissues after SCI.

### **1.3 Surface Properties of Biomaterials and Cell Attachment**

Cell interaction with material surfaces *in vitro* determine the potential for tissue integration; where cell attachment controls cell morphology which in turn affects cell activity relating to the rate and quality of bond formation. Characteristics of the material surface such as material selection, surface features, roughness, composition and energy all affect the cellular response, and while it is generally accepted that choosing a bioactive versus bio-inert material will produce a positive cell response, preference of surface features can differ between cell types.<sup>128,129</sup>

### **1.3.1. Surface Features**

Cell attachment is governed first by focal contacts where surface microstructures allow the initial attachment of cells. These focal contacts do not necessarily require all cell types to adopt a completely flattened morphology on the surface as some cell types require specific cytoskeletal conditions for proper function and signaling to the nucleus. Secondly, many cells types require contact guidance or grooving for orientation and migration, such as fibroblasts which prefer deeper to shallow grooves.<sup>130,131</sup> Osteoblasts on the other hand prefer pores 200-400  $\mu\text{m}$  in diameter for attachment, migration and proliferation.<sup>132</sup> The particulate size has also been shown to affect the cellular response where particles smaller than 125  $\mu\text{m}$  recruit macrophages, those 200-500  $\mu\text{m}$  are optimum for osteoblasts and larger particles recruit fibroblasts.<sup>128</sup> Surface roughness has shown similar distribution in the cellular preferences where, in general, osteoblasts prefer rougher surfaces to those of fibroblasts.<sup>133</sup>

### **1.3.2. Surface Chemistry and Charge**

Surface chemistry and charge can affect the binding and orientation of proteins the cells use to facilitate binding to the surface.<sup>129</sup> Two specific studies show the preference of osteoblasts to surfaces with higher isoelectric points and amorphous vs crystalline Ti/TiO<sub>2</sub>.<sup>128</sup> Surface energy or interfacial free energy is governed by the net charge and polarity at the surface, where these features can enhance the adsorption of proteins or affect the cell membrane potential.<sup>134</sup> The surface energy dictates the binding of ions, water and proteins and the ultimate configuration of each<sup>135</sup> where the alteration of proteins may produce changes in the protein-cell complex which again can affect cell morphology and signalling.<sup>129</sup> The adsorption of various molecules and proteins to the bioactive glass surface from cell media allows for potential cell attachment without prior incubation in SBF, given the other aspects of the material surface are suitable.<sup>136</sup>

## **1.4 Objective**

Development and delivery of bioactive glasses for nerve regeneration has been primarily focused on the peripheral nervous system, where it has been incorporated into polymer scaffolds, and used in the form of fiber wraps.<sup>68,86</sup> These studies found modest benefits to incorporation of the bioactive glass pertaining to axonal regeneration, and

limited to no toxicity. Therefore, options for delivery include particulate composites, fibers or scaffolds similar to those made by Wren et al.<sup>137</sup> which possess specific characteristics that has been shown optimal for tissue integration including: porosity >90% and a pore size of 400-500  $\mu\text{m}$ .<sup>120,137</sup>

Therefore, the objective of the proposed research is to develop a material that can provide physical stabilization of the vertebra and spinal cord, and provide therapeutic factors which encourage and/or guide neuronal cells and nerves to regenerate and reconnect in a manner that restores sensory function. The research herein focuses on the creation of a  $\text{SiO}_2\text{-SrO-Na}_2\text{O}$  glass/glass-ceramic series, where  $\text{Y}_2\text{O}_3$  and  $\text{CeO}_2$  are substituted for  $\text{Na}_2\text{O}$ . Network characteristics are evaluated through network connectivity (NC) calculations, X-ray Diffraction (XRD), X-ray photoelectron spectroscopy (XPS), thermal analysis and magic angle spinning-nuclear magnetic resonance (MAS-NMR). Bioactivity in SBF is observed with scanning electron microscopy (SEM) and energy dispersive spectroscopy (EDS), utilizing pH and ion content as supplemental techniques. Biocompatibility is assessed through the MTT assay and SEM studies with L929 Fibroblasts, MC3T3 Osteoblasts and sNF96.2 Schwann cells. Finally, antioxidant capacity is evaluated with the ABTS assay for both glass-ceramic extracts and particulates.

The following chapter sees the development and characterization of a control glass, and a series of five Y and/or Ce containing glasses, focusing on the network effects of Y and Ce and their potential to elicit a bioactive response.

## CHAPTER 2 - CHARACTERIZATION OF Y<sub>2</sub>O<sub>3</sub> AND CeO<sub>2</sub> DOPED SiO<sub>2</sub>-SrO-Na<sub>2</sub>O GLASSES.<sup>1</sup>

### 2.1 ABSTRACT

The structural effects of yttrium (Y) and cerium (Ce) are investigated when substituted for sodium (Na) in a 0.52SiO<sub>2</sub>-0.24SrO-(0.24-x)Na<sub>2</sub>O-xMO (where  $x = 0.08$ ; MO = Y<sub>2</sub>O<sub>3</sub> and CeO<sub>2</sub>) glass series. Network connectivity (NC) was calculated assuming both Y and Ce can act as a network modifier (NC = 2.2) or as a network former (NC up to 2.9). Thermal analysis showed an increase in glass transition temperature (T<sub>g</sub>) with increasing Y and Ce content, Y causing the greater increase from the control (*Con*) at 493°C to 8 mol% Y (*HY*) at 660°C. Vickers hardness (HV) was not significantly different between glasses. <sup>29</sup>Si Magic Angle Spinning-Nuclear Magnetic Resonance (MAS-NMR) did not show peak shift with addition of Y, however Ce produced peak broadening and a negative shift in ppm. The addition of 4 mol% Ce in the *YCe* and *LCe* glasses shifted the peak from *Con* at -81.3 ppm to -82.8 ppm and -82.7 ppm respectively; while the *HCe* glass produced a much broader peak and a shift to -84.8 ppm. High resolution X-ray Photoelectron Spectroscopy for the O 1s spectral line showed the ratio of bridging (BO) to non-bridging oxygens (NBO), BO:NBO, was altered, where *Con* had a ratio of 0.7, *HY* decreased to 0.4 and *HCe* to 0.5.

---

<sup>1</sup> Published: L.M. Placek, T.J. Keenan, F. Laffir, A. Coughlan, A.W. Wren, "Characterization of Y<sub>2</sub>O<sub>3</sub> and CeO<sub>2</sub> doped SiO<sub>2</sub>-SrO-Na<sub>2</sub>O bioactive glasses," *Biomed Glass*, 1 [1] (2016).

## 2.2 INTRODUCTION

Bioactive glasses are a class of material predominantly used for hard tissue repair in the body. Research into these materials began with the development of 45S5 Bioglass®, discovered in 1969 by Professor Larry Hench, which was found to partially degrade *in vivo*, allowing for the deposition of a hydroxyl-carbonate apatite (HCA) layer essential to the glass bonding and integration with host tissue when implanted into the body.<sup>84</sup> 45S5 is one of many bioactive glasses that can elicit this response where the key compositional element is 45-60 mol% SiO<sub>2</sub><sup>68,86</sup> which produces a random network of SiO<sub>2</sub> tetrahedra where some oxygen (O) atoms lack a Si-O<sub>BO</sub>-Si bonding configuration (bridging oxygen, BO). These non-bridging oxygen (NBO) atoms are instead bound to one Si atom and a modifying element (R) Si-O<sub>NBO</sub>-R, where the ratio of BO/NBO < 1 has been found necessary to allow glass degradation and bioactivity.<sup>99,138</sup> Some of the most common network modifying or intermediate elements include aluminum (Al), fluorine (F), zinc (Zn), strontium (Sr), titanium (Ti), magnesium (Mg), gallium (Ga), and cerium (Ce).<sup>73-75,93,116,139-141</sup> The ability to incorporate different elements into the glass structure can affect network connectivity and rigidity which is related to glass degradation, and in turn can alter the composition, morphology and thickness of the bioactive HCA layer subsequently deposited on the surface; in addition presence in the extracellular fluids upon release can allow these ions to act as therapeutic agents.<sup>101</sup> Some examples include F which is incorporated in dental materials and released (as F<sup>-</sup>) acting to improve the strength of the surrounding tooth.<sup>71,76,77</sup> Sr is used orally as strontium ranelate to improve bone strength in osteoporotic patients and has been added to bioactive glasses used in bone applications to provide a similar therapeutic effect when released as Sr<sup>2+</sup>.<sup>74,101,114</sup> In addition, Sr and Mg have been used to reduce the solubility of the glass network and alter the formation and morphology of the HCA layer.<sup>93,94,142</sup> The diversity of modifying elements that can be incorporated into the Si network of bioactive glasses gives rise to their many applications, such as particulates for bone void filling, glass microspheres for drug delivery, pastes/cements in dental and spinal applications, bone adhesives, scaffolds<sup>69,71,72,143</sup>, and more recently, they have been applied in composite guides for nerve regeneration.<sup>144,145</sup>

The regeneration of nerves, specifically after spinal cord injury (SCI), is of particular interest, and there are many research activities currently aimed at aiding the regeneration and reconnection of these nerves. However, there are a multitude of impediments to this process and over distances greater than 5 mm the reconnection does not often occur properly and functionality is not recovered.<sup>146</sup> Nerve guide conduits with surface modifications and neuro-promoting growth factors have shown some improvement observed in the regeneration and reconnection process, however, the limited ability of nerves to regenerate and multiple post-injury environmental impediments continue to compromise the regenerating nerve tissue before reconnection.<sup>34-37</sup>

This study aims to develop and investigate a series of bioactive glasses that can be used to alleviate two detrimental environmental conditions, specifically, influx of calcium ions ( $\text{Ca}^{2+}$ ) and oxidative damage, for the re-growth of a damaged spinal cord nerve tissue.<sup>68,86</sup> Through compositional modifications, a bioactive glass can be developed that addresses the  $\text{Ca}^{2+}$  accumulation and oxidative stresses that are imposed on nerve tissue after damage; the first is the replacement of  $\text{Ca}^{2+}$  in the glass network with  $\text{Sr}^{2+}$ .  $\text{Sr}^{2+}$  is an ion of similar charge and size to  $\text{Ca}^{2+}$ , has been shown to serve the same network role in bioactive glasses (as a network modifier), encourages bone growth, and is metabolized through the same channels in the body as  $\text{Ca}^{2+}$ .<sup>74,147</sup> By exchanging the  $\text{Ca}^{2+}$  for  $\text{Sr}^{2+}$ , additional  $\text{Ca}^{2+}$  will not be released at the site upon degradation of the glass, while maintaining the glass network degradability and potential bioactivity.<sup>114</sup> The second modification involves the addition of yttrium (Y) and Ce to the glass. Studies using yttria and ceria nanoparticles found that both exhibit neuro-protective properties through direct scavenging of reactive oxygen species (ROS) from the site with limited toxicity.<sup>37,148</sup> In addition, Y and Ce have both been successfully incorporated into bioactive glasses up to 5 mol%.<sup>115,116,149</sup> These simulated body fluid (SBF) studies show that the deposition of a HCA occurs, but is delayed (forms between 7 and 14 days incubation) and thickness is decreased with increasing Y and Ce content as a result of the increased network rigidity. In an effort to avoid the delayed bioactivity observed with previous Y and Ce containing glasses, Na content was increased. The development and characterization of Y and Ce

containing glasses, where  $\text{Ca}^{2+}$  is replaced with  $\text{Sr}^{2+}$ , is the subject of this study, with the aim of evaluating the glass network in terms of potential to elicit a bioactive response.

Techniques used for bioactive glass characterization are focused on evaluating the glass structure and extrapolating their potential to elicit a bioactive response. Calculation of the theoretical network connectivity (NC) can be the first indication of what is occurring when trends are observed in Simultaneous Thermal Gravimetric Analyzer-Differential Scanning Calorimetry (TGA-DSC), Vickers hardness (HV),  $^{29}\text{Si}$  Magic Angle Spinning-Nuclear Magnetic Resonance (MAS-NMR) and X-ray Photoelectron Spectroscopy (XPS). Ideal NC for deposition of a HCA layer is 2.0-2.4, and corresponds to a glass composed of mainly  $\text{Q}^2$ - $\text{Q}^3$  silicate tetrahedral units.<sup>91,92</sup> Trends in the glass transition temperature ( $T_g$ ) and HV observed in simple silicate systems associate increasing  $T_g$ /HV with a greater quantity of BOs, therefore indicating greater connectivity and relative increases in Q-speciation.<sup>150,151</sup> This can also be observed through  $^{29}\text{Si}$  MAS-NMR where a fully connected silicate network of  $\text{Q}^4$  tetrahedra shows a peak center below -100 ppm increasing to nearly -65 ppm for  $\text{Q}^0$  species.<sup>152,153</sup> XPS complements this technique with a main focus on the O 1s spectral line which can commonly be de-convoluted into its BO and NBO components, where the ratio between the two has been related to the potential for dissolution; the initiation step in the process for deposition of a HCA layer on the surface of the glass.<sup>138,154</sup> These techniques are used herein to evaluate the bioactive potential of these Y and Ce containing  $0.52\text{SiO}_2$ - $0.24\text{SrO}$ - $0.24$ - $x\text{Na}_2\text{O}$  glasses based on structure.

## 2.3 EXPERIMENTAL

### 2.3.1. Glass Synthesis

Six glasses of varying composition were formulated for this study, two yttrium (Y) containing glasses (*LY*, *HY*), two cerium (Ce) containing glasses (*LCe*, *HCe*), one glass containing both yttrium and cerium (*YCe*), and one  $\text{SrO}$ - $\text{Na}_2\text{O}$ - $\text{SiO}_2$  control glass (*Con*). The  $\text{Y}_2\text{O}_3$  and  $\text{CeO}_2$  are incorporated into each glass, with the exception of the control, at the expense of  $\text{Na}_2\text{O}$ . Glass compositions (mol%) can be found in Table 2-1.

Table 2-1. Glass Compositions (XPS Comp.) in mol%, Particle Size & Hardness (HV)

	<u>Con</u>	<u>LY</u>	<u>HY</u>	<u>YCe</u>	<u>LCe</u>	<u>HCe</u>
<b>SiO<sub>2</sub></b>	52 (50)	52 (47)	52 (47)	52 (49)	52 (51)	52 (47)
<b>SrO</b>	24 (24)	24 (22)	24 (24)	24 (25)	24 (25)	24 (25)
<b>Na<sub>2</sub>O</b>	24 (26)	20 (28)	16 (22)	16 (17)	20 (22)	16 (20)
<b>Y<sub>2</sub>O<sub>3</sub></b>	-	4 (3)	8 (7)	4 (4)	-	-
<b>CeO<sub>2</sub></b>	-	-	-	4 (5)	4 (2)	8 (8)
<b>Particle Size (<math>\mu\text{m}</math>)</b>	4.2	3.9	4.5	4.3	4.4	4.6
<b>HV (GPa)</b>	5.5	6.0	5.9	5.9	5.5	6.5

### 2.3.1.1. Glass Powder Production

Glass powders were prepared by weighing out appropriate amounts of analytical grade reagents (Fisher Scientific, PA, USA) and ball milling (1 h). The mix was then oven dried (100°C, 1 h), fired (1500°C, 1 h) in a platinum crucible and shock quenched in water. The resulting frit was dried, ground and sieved to retrieve glass particles <20  $\mu\text{m}$ .

### 2.3.1.2. Glass Rod/Plate Production

The powdered mixes of analytical grade reagents (Fisher Scientific, PA, USA) were oven dried (100°C, 1 h) and fired (1500°C, 1 h) in a platinum crucibles. Glass rods/plates were produced by pouring the melts into graphite molds. The graphite molds were left for 1 hr before the glass was removed and subsequently annealed at the glass transition ( $T_g$ ) temperature for 3 hrs. The resulting glass casts were shaped into approximate dimensions of 15 x 3 $\emptyset$  mm rods and 50 x 30 x 5 mm plates using an Ecomet III polish/grinding machine (Buehler, IL, USA) with incremental grit silicon carbide grinding paper (MetLab, NY, USA).

## 2.3.2. Glass Characterization

### 2.3.2.1. Particle Size Analysis (PSA)

Particle size was analyzed using a Multisizer 4 Particle Size Analyzer (Beckman Coulter, CA, USA). Glass powder samples ( $n = 3$ ) were loaded into 20°C Isoton II Diluent at a concentration <10%. Samples were evaluated using a 280  $\mu\text{m}$  standard to a final count of 30000.

#### 2.3.2.2. X-Ray Diffraction (XRD)

Diffraction patterns were collected using a Phaser D2 X-ray Diffraction Unit (Bruker AXS Inc., WI, USA). Glass powder samples ( $n = 1$ ) were packed into zero background sample holders. A generator voltage of 40 kV and a tube current of 30 mA was employed. Scattering patterns were collected in the range  $10^\circ < 2\theta < 70^\circ$ , at a scan step size  $0.02^\circ$  and a step time of 10 s.

#### 2.3.2.3. Network Connectivity (NC)

The NC of the glass series was calculated using equation 1 and basing the calculations on the molar compositions of each glass. Multiple NC calculations were performed based on Y and Ce acting as (1) network formers, where charge compensation is provided in the order  $\text{Na}^+ > \text{Sr}^{2+}$  and as (2) network modifiers. Calculations were made assuming a net of 2 NBO were produced for each Y and Ce atom when assuming they are performing as network modifiers.

$$NC = \frac{\text{Bridging Oxygens} - \text{NonBridging Oxygens}}{[\text{Bridging Species}]} \quad (2-1)$$

#### 2.3.2.4. Thermal Analysis

A SDT Q600 Simultaneous Thermal Gravimetric Analyser-Differential Scanning Calorimetry (TGA-DSC) (TA Instruments, DW, USA) was used to obtain a thermal profile of each glass ( $n = 2$ ), specifically the glass transition temperature ( $T_g$ ) and crystallization temperatures. A heating rate of  $20^\circ\text{C}/\text{min}$  was employed in an air atmosphere using alumina as a reference in a matched platinum crucible. Sample measurements were carried out every 0.5 s between  $30^\circ\text{C}$  and  $1300^\circ\text{C}$ . TA Universal Analysis software (TA Instruments, DW, USA) was used to plot and obtain the temperatures of interest.

#### 2.3.2.5. Vickers Hardness (HV)

HV testing was completed on glass plates mounted in epoxy resin and polished using 1200 grit silicon carbide polishing paper. A HMV-2000 Hardness testing machine (Shimadzu, MD, USA) was used with a 500 g load cell at a load of 200 g and a dwelling

time of 15 s ( $n = 16$ ). Using the attached light microscope and computer, the diagonals created by the Vickers diamond indenter were measured and the hardness was calculated using Eq. (2) where the conversion factor from VHN to GPa is included.

$$HV (GPa) = 0.01819 \frac{F}{d^2} \quad (2-2)$$

where:

$F =$  applied load (kgf)

$d =$  diagonal length (mm)

#### 2.3.2.6. Magic Angle Spinning-Nuclear Magnetic Resonance (MAS-NMR)

$^{29}\text{Si}$  MAS-NMR studies were carried out on a Bruker 600 MHz Wide-Bore Solid State NMR spectrometer with a 9.4 T magnet (600.35 MHz proton Larmor frequency, 119.27 MHz  $^{29}\text{Si}$  Larmor frequency) using a probe head for 7 mm rotor diameters. The specimens ( $n = 1$ ,  $<20 \mu\text{m}$ ) were spun at 5.00 kHz. 200 scans were accumulated with single pulse excitation using a pulse length of  $80^\circ$  at 28 kHz rf field strength. The recycle delays were chosen to be three times the spin lattice relaxation times as determined by inversion recovery sequences. Spin lattice relaxation times ranged between 15 and 26 s. The chemical shift scale was referenced externally against Kaolin as secondary chemical shift standard at -91.34 ppm (center between doublet).

#### 2.3.2.7. X-ray Photoelectron Spectroscopy (XPS)

XPS was performed using a Kratos AXIS-165 X-ray Photoelectron Spectrometer to analyze the surface chemistry, as well as the chemical state of the top few nanometers of the samples. Notched glass bars ( $n = 1$ ) were broken under vacuum. Survey scans were used to monitor the presence of any contaminants. TMono Al X-rays were used with a 100  $\mu\text{m}$  spot size, 25 W, 15 kV, 240 eV pass energy, 0.5 eV step size, 3 sweeps, and a binding energy range of 0–1,100 eV. High resolution scans were then acquired of the binding energy regions associated with each element present in the glass. Spot size, power, and voltage were held consistent, however the pass energy and step size was

reduced to 55 and 0.05 eV respectively, and the number of sweeps was raised to 5. All data was normalized based on the C 1s peak position of 284.8 eV.

#### 2.3.2.8. Preliminary Cell Compatibility

Glass plates ( $n = 1$ ) were buffered for 24 hrs in DMEM Low Media supplemented with 10% FBS in a cell culture incubator at 37°C/5%CO<sub>2</sub>/95%air atmosphere (Fisher Scientific, PA, USA). sNF96.2 Schwann cells (ATCC CRL-2884) were seeded onto the glass plates in 6-well plates at a density of 10<sup>4</sup> cells/well and incubated for an additional 24 hrs. Cells were then fixed using the procedure from Wang et al.<sup>155</sup> and imaged using a Quanta 200F Environmental Scanning Electron Microscope under a vacuum at a pressure of 0.60 torr. The electron beam was used at an accelerating voltage of 20 kV and a spot size of 3.0.

## 2.4 RESULTS

### 2.4.1. Particle Size Analysis

Average particle size ranged from 4.2 μm for *Con* to 4.6 μm for *HCe*, with *LY* falling slightly outside the range at 3.9 μm. Particle sizes for each glass powder are presented in Table 1. *LY* is found to be statistically lower than the glasses containing high modifier content (*HY* and *HCe*) though the average particle size range is <1 μm for all glasses.

### 2.4.2. X-Ray Diffraction (XRD)

Scattering patterns for all glasses can be seen in Figure 2-1. No crystalline peaks were detected in any of the six glasses confirming their completely amorphous nature.

### 2.4.3. Network Connectivity (NC)

The calculated NC for each glass is displayed in Figure 2-2. The NC of the control glass, *Con*, Y, and Ce glasses assuming Y and Ce serve as network modifiers remains constant at 2.2 considering Y and Ce are directly replacing Na. When Y is assumed to act as a network former, the NC increases to 2.6 and 2.9 for *LY* and *HY* respectively. This trend is also seen with the Ce containing glasses where NC increases to 2.4 and 2.7 for *LCe* and *HCe*. The combination of Y and Ce in the *YCe* glass increases

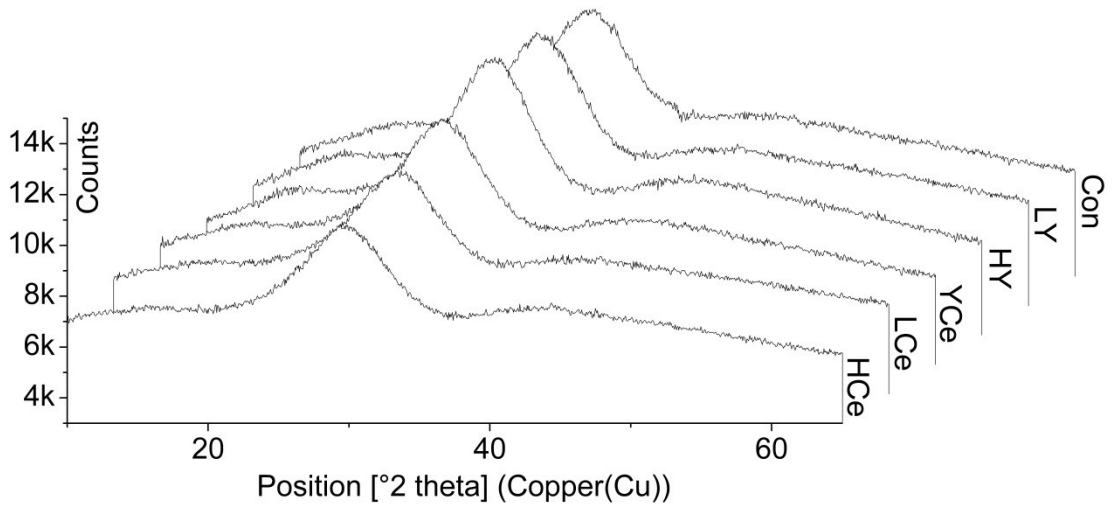


Figure 2-1. X-ray scattering of each glass powder.

the NC to 2.8 when both elements are acting as network formers. Table 2-1 includes this data in addition to the NC as calculated using the compositions obtained through XPS analysis for comparison, and will be discussed in section 2.4.7.

#### 2.4.4. Thermal Analysis

$T_g$  obtained from TGA-DSC are shown in Figure 2-2 and full curves are shown in Figure 2-3. *Con* has the lowest  $T_g$  of 497°C.  $T_g$  increases for all glasses containing Y and/or Ce. Glasses containing 4 mol% Y or Ce content, *LY* and *LCe*, have  $T_g$  values of 592°C, 518°C, respectively.  $T_g$  further increases to 661°C, 625°C, and 566°C with an increase in Y and Ce content for *HY*, *YCe* and *HCe*, respectively. Y content causes the

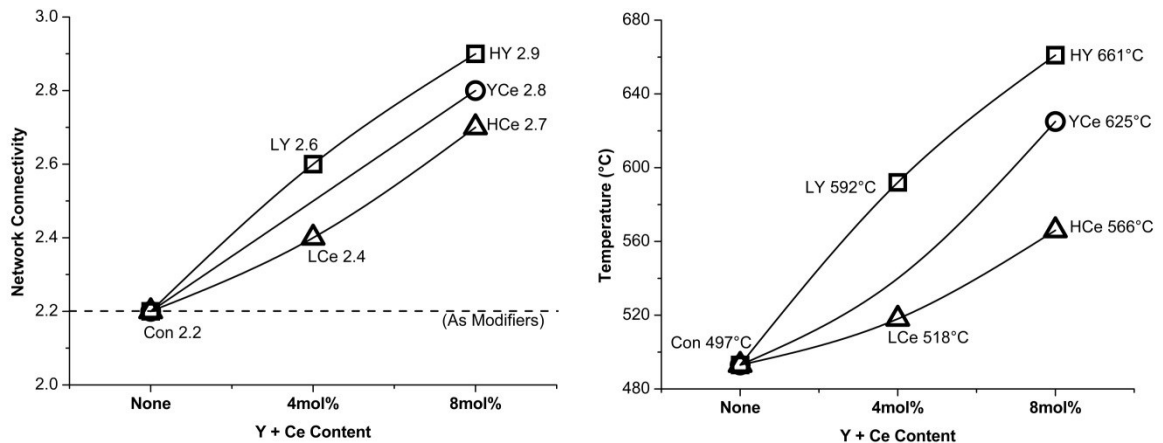


Figure 2-2. (Left) Network connectivity from the molar concentrations given in Table 2-1. (Right) Glass transition temperature ( $T_g$ ) for each glass.

greatest increase in  $T_g$  with a comparable increase when both Y and Ce are added to the same glass.

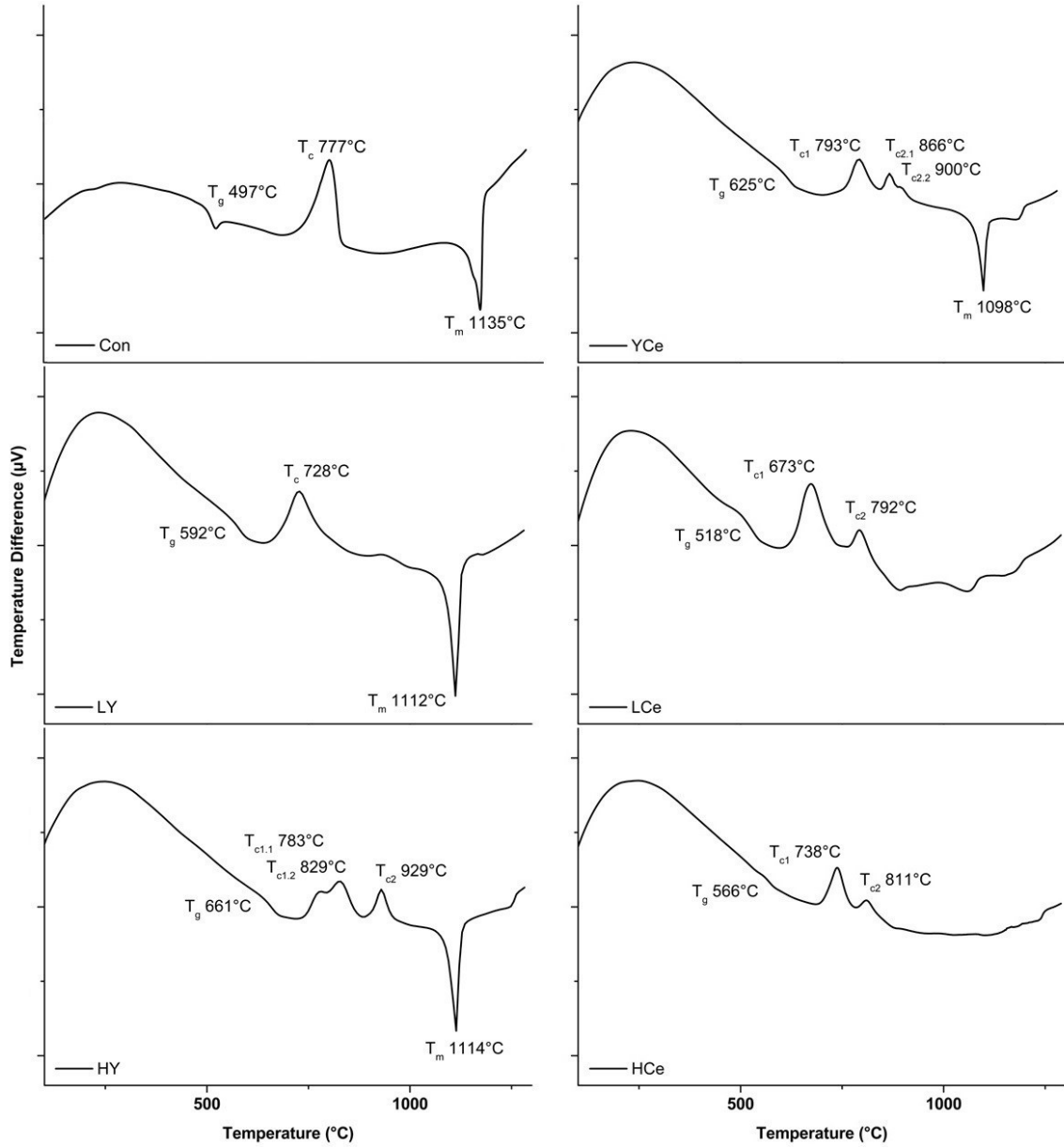


Figure 2-3. SDT curves for each glass with relevant temperatures labeled. Glass transition temperature ( $T_g$ ), Crystallization temperature ( $T_c$ ), Melting temperature ( $T_m$ ).

#### 2.4.5. Vickers Hardness (HV)

HV values are presented in Table 2-1 for all glasses. The control glass, *Con*, and *LCe* containing 4 mol% Ce, have a HV of 5.5 GPa. HV increases to 6.0 GPa and 5.9 GPa with the addition of 4 mol% and 8 mol% Y in the *LY* and *HY* glasses respectively. The glass containing 4 mol% of both Y and Ce also has a HV of 5.9 GPa, while *HCe* containing 8 mol% Ce shows the greatest increase to 6.5 GPa, though the HV difference between the glasses was not found to be significant.

#### 2.4.6. Magic Angle Spinning-Nuclear Magnetic Resonance (MAS-NMR)

MAS-NMR can be used to elucidate the Si environment and associated Q-structure. Figure 2-4 shows the  $^{29}\text{Si}$  MAS-NMR studies for each glass composition. *Con* has a peak location at -81.3 ppm. Y containing glasses did not significantly shift the  $^{29}\text{Si}$  peak location centering at -81.5 ppm and -81.2 ppm for *LY* and *HY* respectively. Peak broadening is observed in the Ce containing glasses along with a slight shifting of the peak center. *YCe* and *LCe* containing 4 mol% Ce shifted the center to -82.7 ppm, while *HCe* with 8 mol% Ce saw the greatest peak broadening and a shift to -84.8 ppm. All peaks de-convoluted using a Gaussian distribution showed a peak curve fit to the primary peak with secondary peaks on the shoulder(s).

#### 2.4.7. X-ray Photoelectron Spectroscopy (XPS)

XPS survey scans, shown in Figure 2-5, were used to confirm the glass composition. Glass compositions as calculated from XPS are included in Table 2-2. All glasses showed a slight decrease in Si content (from 1-5 mol%) and an increase in Na content (2-8 mol%). Sr, Y and Ce content remained consistent with the “as batched” values ( $\pm 1-2$  mol%). Using the XPS compositions, NC was recalculated and is included in Table 2 with the original values for comparison. NC decreases for all glasses due to the decrease in Si content and associated increase in Na content. The NC for *Con* decreases from 2.2 to 2.0. When Y and Ce are assumed to act as network formers the greatest NC decrease is seen for *LY* going from 2.6 to 2.1, followed by *HY* and *HCe* both decreasing by a factor of 0.3. The NC drops below 2.0 when Y and Ce are assumed to act as network modifiers, with the exception of *LCe* (2.1) and *Con* which remains constant (2.0).

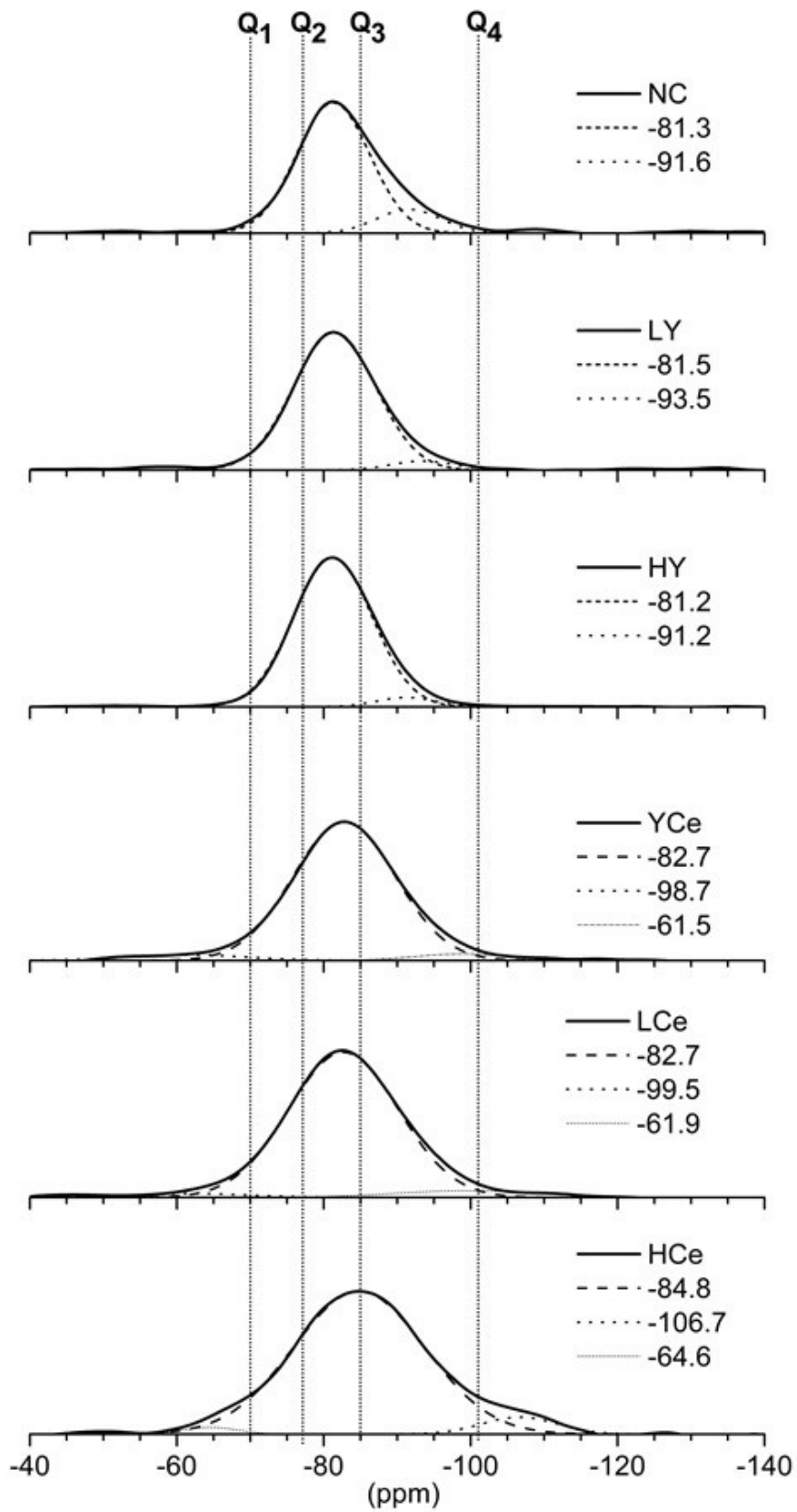


Figure 2-4.  $^{29}\text{Si}$  MAS-NMR of each glass.

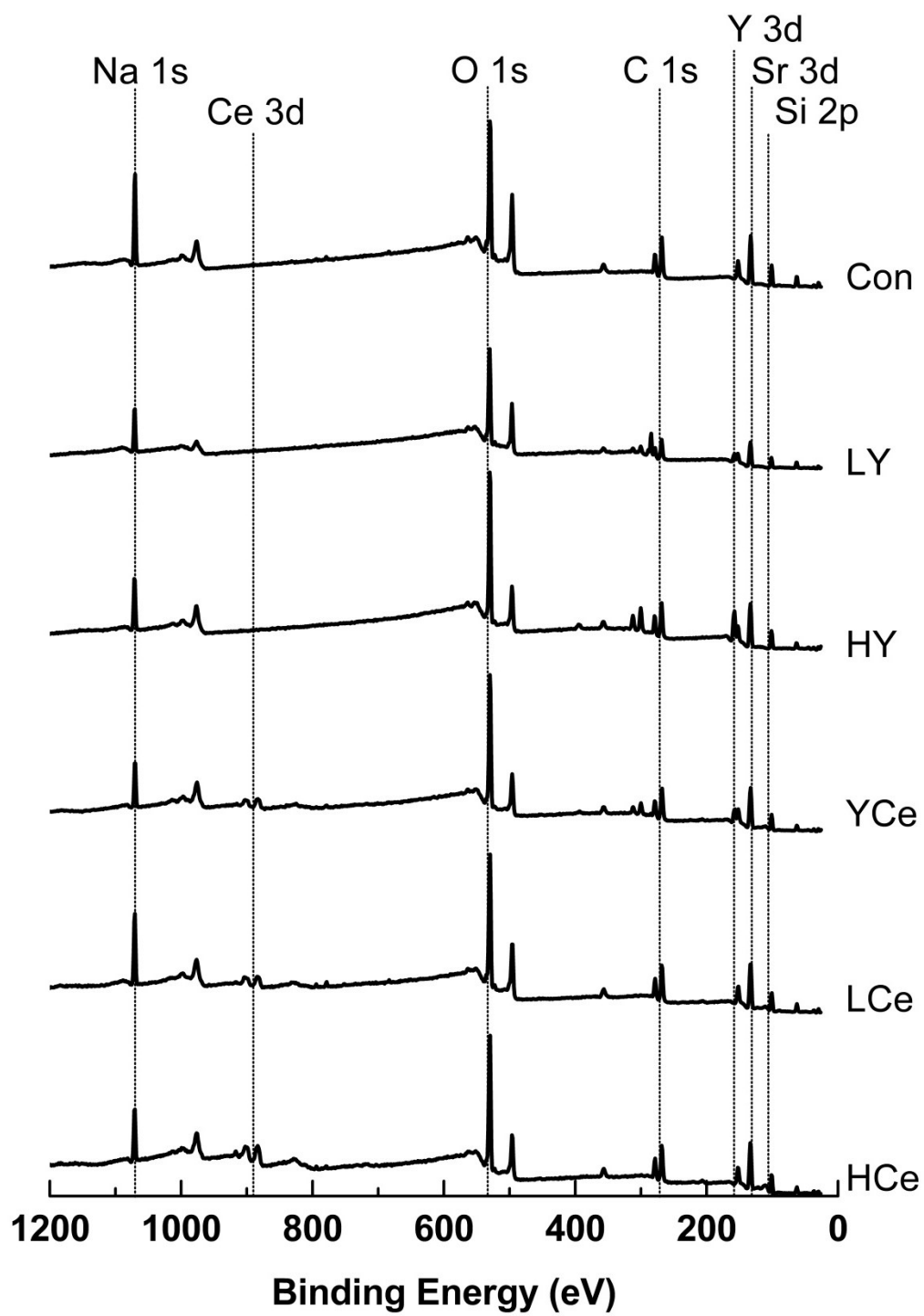


Figure 2-5. XPS survey scans of each glass.

Table 2-2. Network Connectivity (using XPS comp.)

	<u>Con</u>	<u>LY</u>	<u>HY</u>	<u>YCe</u>	<u>LCe</u>	<u>HCe</u>
<b>Modifiers</b>	2.2 (2.0)	2.2 (1.7)	2.2 (1.7)	2.2 (1.9)	2.2 (2.1)	2.2 (1.7)
<b>Formers</b>	2.2 (2.0)	2.6 (2.1)	2.9 (2.6)	2.8 (2.7)	2.4 (2.2)	2.7 (2.4)

High resolution scans for Si 2p, Sr 3d, Na 1s, Y 3d, Ce 3d and O 1s were completed and the binding energy (BE) for each peak maximum can be found in Table 2-3. The range in BE for the 6 glasses and each spectral line is  $\leq 0.7$  eV indicating no significant shift in BE. High resolution scans for Y and Ce are shown in Figures 2-6 and 2-7. The Y 3d<sub>5/2</sub> and Y 3d<sub>3/2</sub> peaks are seen in each Y containing glass (*LY*, *HY* and *YCe*) without significant shift in peak location or area. An indistinct maximum is seen in the Ce 3d<sub>5/2</sub> and Ce 3d<sub>3/2</sub> peaks of the Ce containing glasses (*LCe*, *HCe*, *YCe*). After curve fitting it can be seen that each glass containing 4 mol% Ce displays two peaks contributing to each spin of the Ce 3d spectral line (*a*, *b* and *c*, *d*) and a shoulder, *e*, around 916 eV. The shoulder becomes more prominent when Ce content is increased to 8 mol% in the *HCe* glass, and is associated with the appearance of an additional peak in each spin state (*a*<sub>2</sub> and *c*<sub>2</sub>).

Table 2-3. High Resolution XPS Peak Locations

<u>Spectral Line</u>	<u>Con</u>	<u>LY</u>	<u>HY</u>	<u>YCe</u>	<u>LCe</u>	<u>HCe</u>
Si 2p	101.2	101.5	101.4	101.1	101.2	101.1
Sr 3d <sub>5/2</sub>	132.6	133.0	133.1	132.9	132.8	132.7
Sr 3d <sub>3/2</sub>	134.3	134.6	134.7	134.4	134.6	134.5
Na 1s	1070.4	1070.8	1071.0	1070.7	1071.1	1071.1
Y 3d <sub>5/2</sub>		157.7	157.2	157.4		
Y 3d <sub>3/2</sub>		159.8	159.2	159.4		
Ce 3d <sub>5/2</sub> a				880.8	881.1	880.7
Ce 3d <sub>5/2</sub> a <sub>2</sub>						882.6
Ce 3d <sub>5/2</sub> b				884.6	884.8	884.9
Ce 3d <sub>3/2</sub> c				898.7	899.1	898.7
Ce 3d <sub>3/2</sub> c <sub>2</sub>						901.3
Ce 3d <sub>3/2</sub> d				902.3	903.0	902.9
Ce 3d <sub>3/2</sub> e				916.3	916.3	916.6
O 1s NBO	529.4	529.9	529.9	529.5	529.5	529.7
O 1s BO	531.1	531.1	531.4	531.1	531.3	531.4

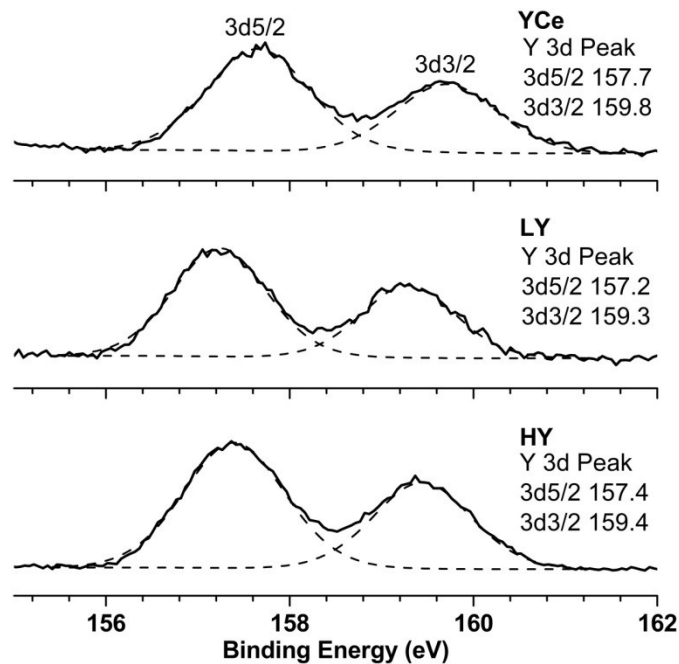


Figure 2-6. High resolution scans of the Y 3d peak for yttrium containing glasses, *LY*, *HY*, and *YCe*.

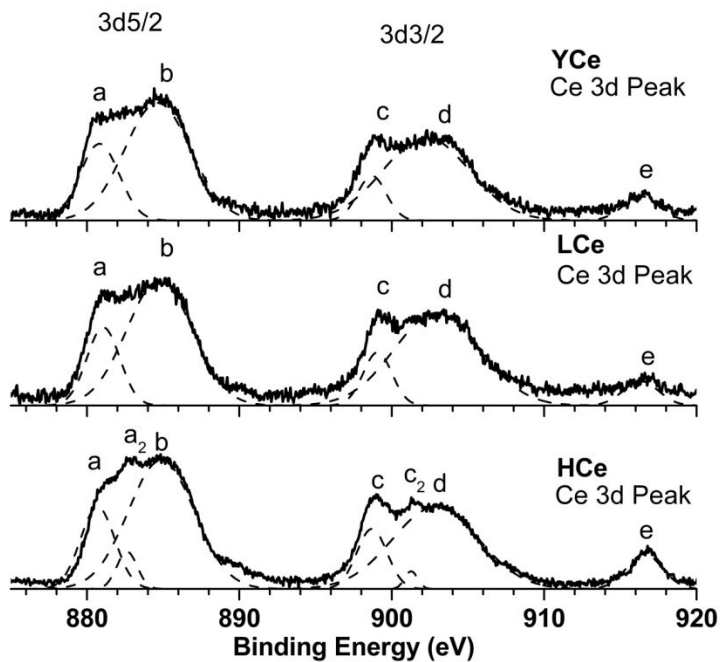


Figure 2-7. High resolution scans of the Ce 3d peak for cerium containing glasses, *LCe*, *HCe*, and *YCe*.

Fitting of the O 1s spectral lines for the *Con* and glasses containing high total modifier content (*HY*, *YCe*, *HCe*) was undertaken and is presented in Figure 2-8. In the control glass, *Con*, a high energy peak, centered at 531.1 eV, is indicative of BOs, and a low energy peak, centered at 529.4 eV, represents NBOs. These BO and NBO peaks are present in each glass and it can be seen that slight shifting occurs of the peaks to higher BE with addition of Y, and to a lesser degree with Ce. Peak fitting revealed there is a decrease in the ratio of BO:NBO (shown in Figure 2-9) where *Con* has a ratio of 0.7, decreasing to 0.6, 0.5 and 0.4 for *YCe*, *HCe* and *HY* respectively.

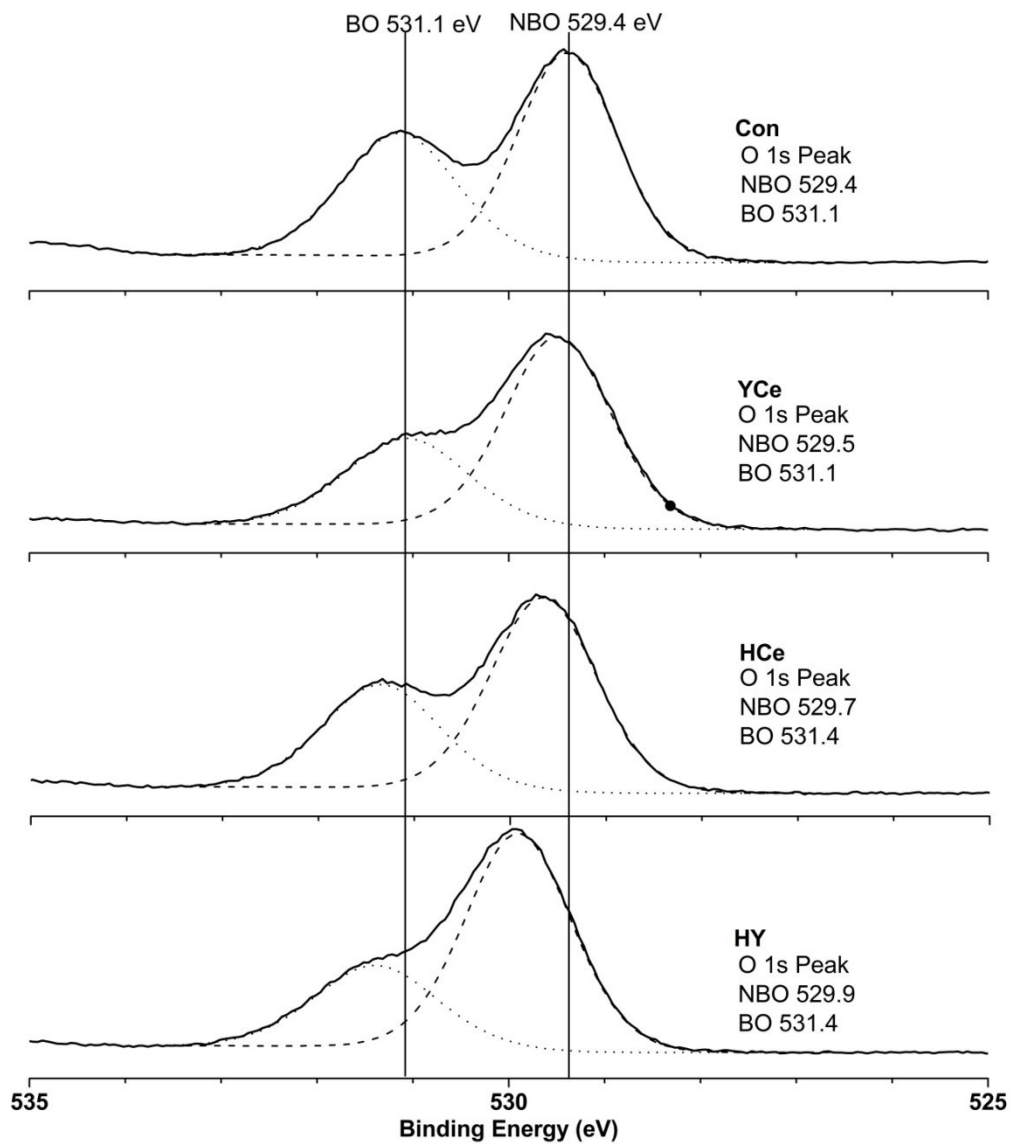


Figure 2-8. High resolution scans of the O1s peak for *Con*, *YCe*, *HCe* and *HY*.

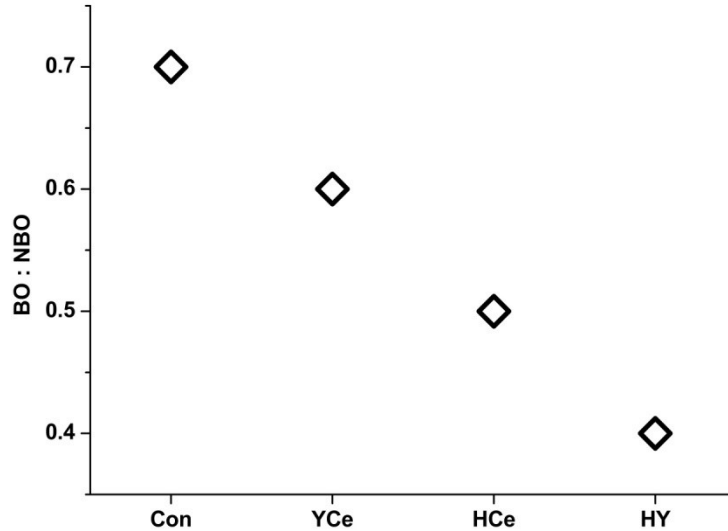


Figure 2-9. Bridging to non-bridging oxygen ratio as determined using O1s high res-XPS for *Con*, *YCe*, *HCe* and *HY* glasses.

#### 2.4.8. Preliminary Cell Compatibility

Images showing Schwann cell interaction with the polished bulk glass surfaces can be seen in Figure 2-10. All glasses prove to be acceptable surfaces for growth and attachment of Schwann cells, though differences in cell density and morphology are apparent, where the *Con* and *LCe* glasses show Schwann cells extensively covering the glass surface and spread forming a connected network. *LY* and *HCe*, appear to support a slightly lower cell population where most cells form a connected network over the surface. *HY* and *YCe* glasses show a significantly decreased cell population where cells are localized to groups and do not form a connected network, however individual cells show a greater degree of spreading on the glass surface.

## 2.5 DISCUSSION

With the aim of incorporating Y and Ce to reduce the oxidative damage associated with nerve injury while retaining bioactivity, 6 glasses containing various quantities of Y and/or Ce were synthesized and NC calculated assuming both a forming and modifying role for Y and Ce. The common cation charge of Y is  $Y^{3+}$ , and Ce is also

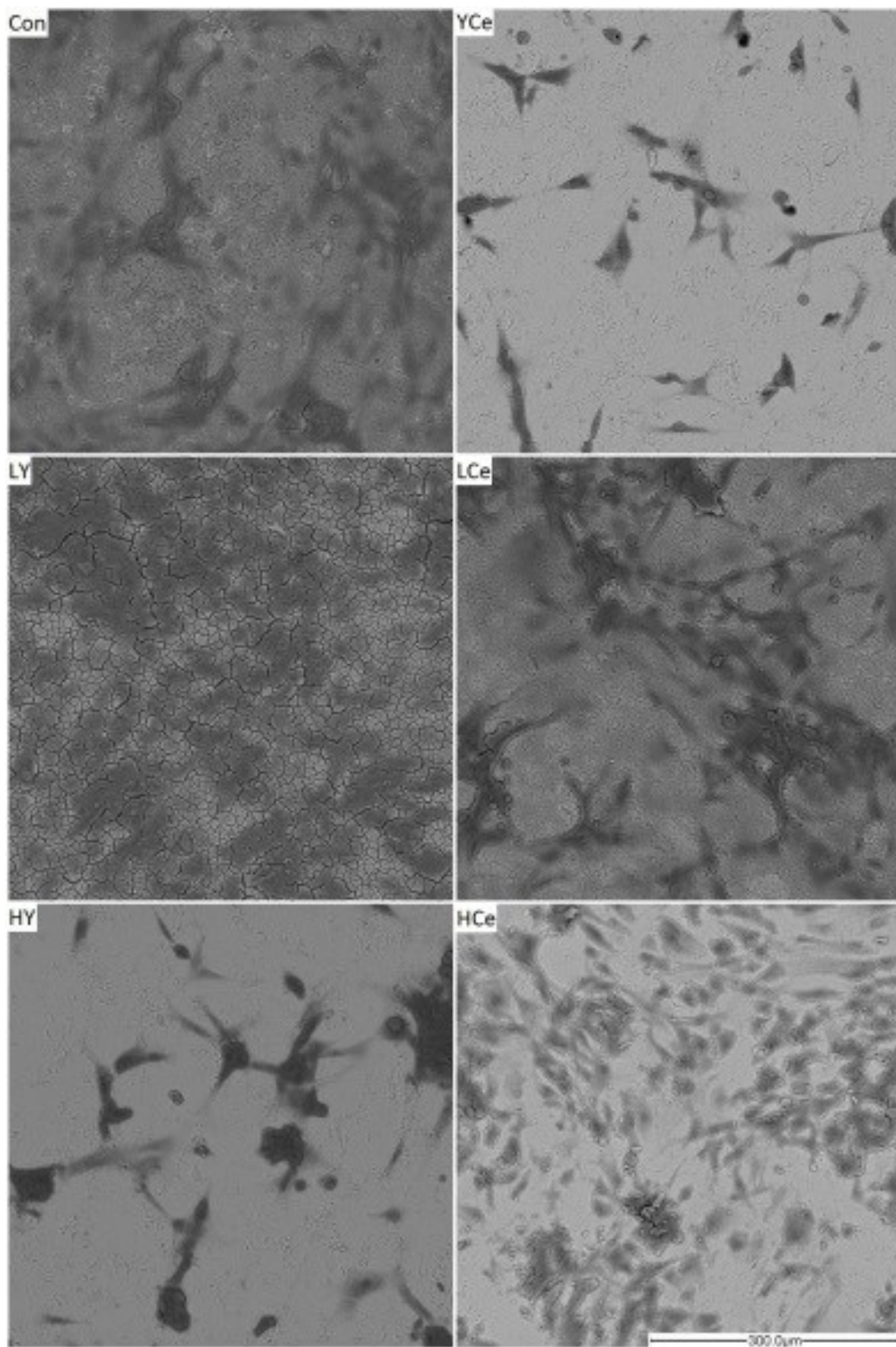


Figure 2-10. SEM images of Schwann cells fixed on each polished glass surface at 200X.

found as  $Ce^{3+}$ , analogous to that of both  $Al^{3+}$  and  $Ga^{3+}$  which have been found to act as network intermediates depending on the ratio to Si and charge compensating cations.<sup>156,157</sup> Ce is also found as  $Ce^{4+}$ , and while similar in charge to Si, it is nearly double the ionic size in addition to having a typical coordination environment greater than 4 as is seen for Si,<sup>158</sup> therefore is not expected to serve in typical Si tetrahedral positions, though may produce an analogous forming effect. NC calculations, assuming that the Y and Ce are incorporated into the glass network in a forming role, suggests Y will produce a greater NC increase as a result of the required charge compensation, and Ce will produce an increase in NC similar to that of Si. However, considering Ce commonly exists in multiple oxidation states ( $Ce^{3+}$  and  $Ce^{4+}$ ) in glass structures, and has not been processed to produce glass of either state exclusively, multiple techniques within this study will be necessary to determine the cumulative role of Ce species within these glasses. As network modifiers,  $Y^{3+}$  and  $Ce^{3+}$  are assumed to create 2 NBOs/mol and therefore directly replace Na, suggesting that the NC will remain constant. The calculated NC for these glasses falls into the optimum range for bioactivity at 2.2 assuming Y and Ce act as network modifiers, and approach/exceed the upper limit when calculated as formers, however previous studies have found both to act primarily as network modifiers.<sup>115,116,159,160</sup>

Glass formation and processing is verified through XRD that a completely amorphous structure was achieved for each glass, thereby avoiding potential mismatched onset times for the formation of a HCA layer seen with partially to fully crystallized materials,<sup>124,126</sup> and average particle size for the glass powders falls within a 1  $\mu m$  range further ensuring consistency between samples. Thermal analysis of the glasses was used to evaluate any change in the  $T_g$  where an increase in  $T_g$  represents greater stability of the glass network, which can be an effect of ionic differences or often as a result of increased quantities of BOs and higher NC.<sup>150,151</sup> The significant increase in  $T_g$  with both Y and Ce content is seen for all glasses, increasing with increasing content. This indicates increased network stability as a result of the replacement of Na with both Y and Ce, where Y and Ce have complementary effects in the *YCe* glass and Y is producing a greater effect. This  $T_g$  increase is likely due to the ionic differences relating to Na, Y, and Ce considering the charge, size, field strength, and coordination environment typically adopted by each. Na

is found as  $\text{Na}^{1+}$  in glass networks and has low field strength in comparison to Y or Ce. In the glass each Na ion is associated with NBO and experiences an ionic association that is relatively weak; these characteristics allow Na to easily move through the glass network as evidenced by the immediate exchange with hydronium ions in incubation fluids.<sup>161,162</sup> Y and Ce are similar in ionic size to Na, however, as trivalent and tetravalent ions their associated field strength is higher which may impart a covalent characteristic to the O atoms they associate with within the glass network. In addition, the coordination environment of both Y and Ce in glasses has been found to be between 6 and 8 where they preferentially associate with NBOs.<sup>158,163,164</sup> These characteristics are likely producing the increase seen in  $T_g$  where stronger Y-NBO and Ce-NBO association with multiple NBOs increase the stability, and likely has implications for their non-movement through the glass structure *in vivo* which has been observed through lack of release in SBF studies.<sup>115,116,165</sup> When considering the possibility of increased network connectivity or rigidity, hardness can prove complementary and offer further indication of structural changes with composition.<sup>166,167</sup> Current models use constraint theory to predict changes in the hardness where increased constraints on the network through increased connectivity reflect greater hardness values, though complex systems experience local maximum/minimum and are not completely understood.<sup>168</sup> The lack of significant difference in hardness between the control glass and Y and Ce containing glasses suggests there is not a significant change in network connectivity. Therefore, considering the hardness in correlation with the  $T_g$ , Y and Ce are likely acting as modifiers, while producing an increase in network rigidity as an effect of their ionic characteristics compared to Na.<sup>115,116,160</sup>

To gain a better understanding of the role of Y and Ce in the glasses, the Si tetrahedral environment was evaluated using  $^{29}\text{Si}$  MAS-NMR and characteristic Q-species indicators. Q species for  $\text{SiO}_4$  tetrahedra represent the NBO per Si where  $Q^0$  represents 4-NBO/Si and  $Q^4$  0-NBO/Si. The  $Q^1$  species is centered between -70-72 ppm,  $Q^2$  at -77-80 ppm,  $Q^3$  at -85-89 ppm and  $Q^4 \geq -101$  ppm.<sup>89,152,153,169</sup> Bioactive glasses typically exhibit a  $Q^2$  to mainly  $Q^3$  species distribution which corresponds to a NC within the 2.0-2.4 range.<sup>89</sup> The control glass, *Con* illustrates an appropriate initial composition with a calculated NC of 2.2 and an NMR peak location at -81 ppm falling between the  $Q^2$

and  $Q^3$  species characteristic shifts. This indicates the *Con* will likely exhibit degradability to allow for a bioactive response *in vivo*. Similarly, *LY* and *HY* produce a minimal shift in comparison to *Con* supporting the  $Q^2$ , partially  $Q^3$   $Q$ -structure. This substantiates the  $T_g$ , HV, and literature that Y is performing as a network modifier. With the addition of Ce, a negative shift is observed for *YCe*, *LCe*, and *HCe*; the magnitude of which is similar for *YCe* and *LCe* and greater for *HCe*, indicating the effect is solely due to Ce content in the *YCe* glass. Generally this shift toward a higher  $Q$ -structure, indicates increased network connectivity, however shifts for  $Q$ -species have characteristic ranges up to 10 ppm depending on the conditions and composition of silicate glasses; therefore the 1.4 – 3.5 ppm shift observed may not be significant based on the average  $Q^x$  shift values chosen for graphical representation. A distinct feature of significance present in the MAS-NMR spectra is peak broadening occurring with the addition of Ce to the glass and presence of shoulders in the  $Q^0$  and  $Q^4$  characteristic regions. The broadening suggests the  $Q$ -species distribution in the glass is becoming diversified where in an ideal glass there will be a ratio of two adjacent  $Q$ -species. In practice, glasses will typically exhibit two prominent  $Q$ -species with small contributions from the remaining, which is the case with the *Con* and Y containing glasses with a prominently  $Q^2$ - $Q^3$  distribution. The addition of Ce however suggests the presence of increasing quantities of each  $Q$  type with increasing Ce content. It can also be seen that the Ce effect on Si-O environment is not affected by the presence of Y in the glass as the peak shifts and shoulders are similar in both *YCe* and *LCe* containing 4 mol% Ce each. This  $Q$ -species distribution is possibly due to the multivalent states and range in coordination environments adopted by Ce ions in glasses.<sup>116,158</sup> The presence of  $Ce^{4+}$ , with higher field strength than  $Ce^{3+}$ , may begin acting as an intermediate, where Si-O- $Ce^{4+}$  bridges approach the BO to NBO distinction simulating  $Q^4$  forming regions. In comparison, the  $Ce^{3+}$  ions may produce regions where the coordination environment and potential charge balancing implications create species ranging from  $Q^0$  to  $Q^3$ . While the overall peak shift may suggest a higher quantity of  $Q^3$  species, peak broadening indicates there are a range of local effects on the Si-O-X environment associated with Ce which may be clarified through high-resolution XPS.

The compositional comparison as determined by XPS maintains a consistent reduction of Si and an increase in Na. Minimal shifting in the Si 2p, Sr 3d, Na 1s, and Y

3d peaks do not indicate a significant difference in the elemental bonding environment between glasses. The lack in shift of the Si 2p peak is of interest specifically for the Ce containing glasses considering the peak shift and broadening observed in MAS-NMR. The overall shift in the MAS-NMR spectra relating to the bridging or non-bridging nature of the Si coordinating O atoms, does not appear to effect the immediate Si-O bonding reflected in the XPS survey scan. The Ce 3d spectral line does not exhibit a maximum, but does have the characteristic Ce 3d<sub>5/2</sub> and Ce 3d<sub>3/2</sub> multiplet with contributions from Ce in both the Ce<sup>3+</sup> and Ce<sup>4+</sup> oxidation states as demonstrated in a study by Gavarini et al.<sup>170</sup> Relating the BEs found in that particular study to the data for the Ce containing glasses in this work, components *a*, *b*, *c* and *d* of the multiplet are attributed primarily to Ce<sup>3+</sup> with a small content of Ce<sup>4+</sup> reflected in each and component *e*. In *HCe*, *e* becomes increasingly prominent with the appearance of tertiary components *a*<sub>2</sub> and *c*<sub>2</sub> also suspected to be attributed to Ce<sup>4+</sup>. The multiple states of Ce and the modest increase in Ce<sup>4+</sup> as Ce content increases, supports the peak broadening seen in MAS-NMR as increasing the diversity of Ce ions will produce an increasingly complex coordination and charge compensation dynamic within the network. The mechanisms of Ce in the glasses are not well distinguished through the MAS-NMR data suggesting looking instead at the O environment. The XPS O1s peak data shows the addition of Y and Ce shifts both BO and NBO peaks to slightly (0.3-0.5 eV) higher BEs compared to the control glass, *Con*. This is likely due to the ionic effect associated with substituting Y and Ce at the expense of Na; where National Institute of Standards and Technology (NIST) BE for the Na-O peak is prominent at 529.7 eV and Y<sub>2</sub>O<sub>3</sub>, CeO<sub>2</sub> and Ce<sub>2</sub>O<sub>3</sub> peaks are found up to 532.0 eV,<sup>171</sup> and is supported by T<sub>g</sub>/HV. The significant differences between glasses from XPS become apparent when analyzing the ratio of BO:NBO. BO:NBO decreases with the addition of both Y and Ce indicating that while they increase the network rigidity, in replacing Na, *HY* is creating a 17% increase and *HCe* is creating an 11% increase in NBOs at 8 mol%. This increase in NBO is not suggested in the NMR spectra and may be attributed to variations in the physical state of the samples where MAS-NMR was run on <20 μm powders and XPS with glass surfaces broken under vacuum. Atmospheric interaction the high energy surface of the glass particulate likely altered the network at the surface of the particles, which can in turn affect the overall MAS-NMR spectra, while

XPS will show the bulk characteristics. The creation of a greater quantity of NBOs with the addition of Y in comparison to Ce may be due to any number of differences between the two such as distribution throughout the network, coordination environment, required charge balancing, and presence of Ce in a tetravalent state. Further the *YCe* glass creates only a 6% increase in NBO where it might be expected to fall between *HY* and *HCe* as seen with the  $T_g$  values. While the effect of Y and Ce is complementary in producing the increase in network rigidity seen through  $T_g$  they appear to behave independently in the network considering the MAS-NMR shifts are nearly identical to that of *LCe* and the XPS peak locations do not significantly shift indicating lack of interaction between the two within the network. Therefore, the effect when considering network connectivity is likely not additive and would be representative of the 4 mol% additions which would produce an average increase in NBOs around 7%, which is still slightly higher than that observed in the actual *YCe* glass but may be accounted for by additional charge balancing required with multiple tri/tetravalent ion types existing within the same network. A BO:NBO ratio greater than 1 indicates a glass will have low bioactivity, *Con*, *HY*, *YCe*, and *HCe* all maintain BO/NBO ratios less than 1 further supporting their potential to degrade and incite the formation of a HCA layer *in vivo*.<sup>172</sup>

The glass series shows network characteristics suggesting their bioactive potential (evaluation of which will be the subject of future work) but does not give any indication of their biocompatibility. Therefore, work was undertaken to evaluate initial biocompatibility with Schwann cells on the polished glass surface where each was shown to support cell attachment with differences in population. This may be affected by any number of factors including but not limited to composition, surface charge and energy, or slight roughness variation. Based on population size present on the glass surfaces the *Con* and *LCe* glasses appear to perform slightly better than *LY* and *HCe*, followed by *HY* and *YCe* and is likely due to surface effects created by the increasing Y and Ce content.

## 2.6 CONCLUSION

Y glasses show a significant increase in thermal stability, while not altering the glass hardness or indicating a prominent shift in the Q-species as observed by <sup>29</sup>Si MAS-NMR. XPS shows a decrease in the BO:NBO ratio with 8 mol% Y supporting the literature that it serves as a network modifier in the glass structure while increasing the

rigidity due to its ionic properties. Ce glasses show moderate increase in  $T_g$ , no change in hardness, and present a negative shift and peak broadening in the  $^{29}\text{Si}$  MAS-NMR, suggesting the diversification of Q-species. XPS shows an indistinct maximum with multiple Ce states for the Ce 3d spectral line indicating an increase in  $\text{Ce}^{4+}$  ions with increasing Ce content and a decrease in BO:NBO ratio similar to that of Y. Therefore, while the multitude of bonding environments associated with the presence of tri/tetravalent Ce may indicate some intermediate activity, collectively it serves as a network modifier in the Ce-containing glasses.

The ability of bioactive glasses to interact with physiological fluids and induce the deposition of a HCA layer is dependent on the glass composition and the connectivity of its network, which can be interpreted through various characterization techniques. The characterization techniques used in this work to evaluate the network structure, in agreement with previous studies, support that Y and Ce are both performing primarily as network modifiers in the glasses, and increase network rigidity due to their ionic characteristics. This suggests NC falls within the optimum range for bioactivity, while Schwann cell attachment to each glass surface supports preliminary biocompatibility and maintains that these glasses are candidates for solubility and cytocompatibility studies.

Therefore, the following chapter focuses on evaluating the glass series solubility through pH and ion release relating to cytocompatibility of dissolution products. Time and dose dependent cytocompatibility is evaluated with L929 Fibroblasts, MC3T3 Osteoblasts, *E.coli* and *S. Aureus* cell and bacterial lines. In addition, antioxidant capacity of the extracts is evaluated to determine the potential these glasses may have to provide neuroprotection under oxidative stress.

## CHAPTER 3 - SOLUBILITY, CYTOTOXICITY AND ANTIOXIDANT CAPACITY OF Y<sub>2</sub>O<sub>3</sub> AND CeO<sub>2</sub> DOPED SiO<sub>2</sub>-SrO-Na<sub>2</sub>O GLASSES.<sup>2</sup>

### 3.1 ABSTRACT

The solubility and cytocompatibility of Yttrium (Y) and Cerium (Ce) are investigated when substituted for Sodium (Na) in a 0.52SiO<sub>2</sub>-0.24SrO-(0.24-x)Na<sub>2</sub>O-xMO glass series (where MO = Y<sub>2</sub>O<sub>3</sub> or CeO<sub>2</sub>). Solubility is evaluated through pH and Inductive Coupled Plasma-Optical Emission Spectrometry (ICP-OES) analysis where pH of deionized (DI) water increased between 11.2 and 12.5 after incubation of glass powders over 1, 7 and 30 days. Ion release of Silicon (Si), Na and Strontium (Sr) from the *Con* glass (not containing Y or Ce) was at minimum 2x greater than that of glasses containing Y or Ce, where *Con* Si release reached a solubility limit after 1 day and then precipitated in the following 7 and 30 days. Release from Y and Ce containing glasses reached a maximum of 1800 µg/mL, 1800 µg/mL, and 10 µg/mL for Si, Na, and Sr, respectively. Release of Y and Ce was below the ICP-OES detection limit <0.1 µg/mL. Cell viability of both L929 fibroblasts and MC3T3 osteoblasts decreased for *Con*, *LY*, and *LCe* extracts; *HY* extracts did not significantly decrease cell viability while *YCe* and *HCe* saw viability decrease at higher extract concentrations (20%, 33%). Bacterial studies saw similar trends to those observed with fibroblasts and osteoblasts, where *Con* and *LY* eliminated 100% of bacteria at a 9% extract concentration. In addition, antioxidant capacity (a possible mechanism for neuroprotection) was evaluated using the ABTS assay where all glasses had some inherent radical oxygen species (ROS) scavenging capability with *Con* reaching 9.5 mMTE.

---

<sup>2</sup> Under review; Co-authors: Timothy J. Keenan, Aisling Coughlan, Anthony W. Wren.

### 3.2 INTRODUCTION

Bioactive glasses have a variety of applications due to their characteristic dissolution when in contact with fluids, including water and various simulated or physiological fluids that can result in the deposition of a hydroxycarbonate-apatite (HCA) layer and subsequent formation of a bond with host hard tissues.<sup>84,90</sup> The dissolution of the glassy network is initiated by exchange of hydrogen ions ( $H^+$  or  $H_3O^+$ ) with  $R^+$  and  $R^{2+}$  (commonly  $Na^+$  and  $Ca^{2+}$ ) modifying ions in the glass network. This is followed by attack of the Si-O bonds to form silanol groups and allows for  $Si(OH)_4$  dissolution into the aqueous environment.<sup>127</sup> Biocompatibility is dependent on the quantities of these dissolution products and the response they induce in the adjacent cells. Dissolution products from silicate based bioactive glasses are known to exhibit osteogenic, angiogenic, and antibacterial properties.<sup>101</sup> Specifically, the glass former, Si, is known to support collagen I and extra cellular matrix formation, is essential for metabolic processes relating to formation and calcification of the bone matrix, and, in oral supplements, improve bone mineral density.<sup>101,173</sup> Na is an essential component in blood and extracellular fluids maintained at concentrations up to 3600  $\mu\text{g/mL}$  and is involved in multiple cellular functions and signaling.<sup>111,112</sup> Calcium (Ca) and Sr have been shown to serve the same role in the glass network as well as some similar functions within the body. Sr was first administered to osteoporosis patients as strontium ranelate<sup>[13]</sup> and is known to localize to bone tissue where it can substitute for Ca. It is present in extracellular fluids at  $\mu\text{M}$  concentrations whereas Ca is present at mM concentrations<sup>101,113,114</sup> but toxicity has not been reported since excess is excreted through the kidneys in the same manner as Ca.<sup>74,113</sup> Additional elements of interest are Y and Ce which have been successfully incorporated into bioactive glasses, however, the studies concerning the dissolution of these glasses give limited information reflecting any effect they may have on biocompatibility as any release was minimal. In addition, these studies show that bioactivity decreased in glasses with increasing Y and Ce content, but the deposition of a HCA layer did occur after incubation in simulated body fluid (SBF).<sup>115,116</sup> Other studies evaluating yttria and ceria nanoparticles found they were non-toxic up to 200  $\mu\text{g/mL}$  and offered neuroprotection via direct ROS scavenging.<sup>37,148</sup> This antioxidant

capacity is what is hoped to be imparted on the SiO<sub>2</sub>-SrO-Na<sub>2</sub>O glass used in this work through doping with Y<sub>2</sub>O<sub>3</sub> and CeO<sub>2</sub>.

Antioxidant potential is of significant interest for applications involving nerve regeneration and reconnection since one of the many factors impeding this process are ROS. Primary physical damage to nerve tissue is accompanied by ischemia, inflammation, migration of activated glial cells and loss of ionic homeostasis in the extracellular fluid due to the influx of calcium and production of cytokines and ROS.<sup>33,174</sup> Nerve tissue is particularly sensitive to changes in the ionic content of extracellular fluids and after injury the consequential fluctuations cause Ca excitotoxicity and necrosis in adjacent (uninjured) nerve tissues.<sup>34</sup> This secondary damage occurring at and around the injury site significantly impedes the regeneration and reconnection of nerves, and over distances greater than 5 mm the reconnection does not often occur properly and functionality is not fully recovered.<sup>21,34-37,68,86,146</sup> Standard treatment of nerve injury involves the administration of Methylprednisolone Sodium Succinate (MPSS) to reduce the inflammatory response, which addresses only one of the many impediments encountered by regenerating axons after injury.<sup>86,144,149,175</sup> Recent studies have shown bioactive glasses have the potential to encourage nerve regeneration after injury through mechanical guidance and delivery of growth factors. Therefore, this work proposes the inclusion of Y<sub>2</sub>O<sub>3</sub> and CeO<sub>2</sub> into bioactive glass which may produce ROS scavenging capability similar to that observed in yttria and ceria nanoparticles, where Sr is replaced with Ca to avoid contributions to Ca excitotoxicity.

Previous work by the authors investigating these Y<sub>2</sub>O<sub>3</sub> and CeO<sub>2</sub> doped SiO<sub>2</sub>-SrO-Na<sub>2</sub>O glasses found Y and Ce serve as modifying ions in the glass network while increasing the rigidity due to ionic differences with Na for which they are being substituted, but maintain a network connectivity and structure that should support dissolution, biocompatibility and potentially bioactivity. In this work the dissolution products will be evaluated along with their effect on L929 fibroblasts, MC3T3 osteoblasts, *Escherichia Coli*, and *Staphylococcus Aureus* to assess the cytocompatibility. Antioxidant capacity will be assessed via the ABTS assay to determine the potential of these glasses to provide protection from ROS produced after nerve tissue damage with the goal of improving nerve regeneration and reconnection.

### 3.3 EXPERIMENTAL

#### 3.3.1. Glass Synthesis

Six glasses of varying composition were formulated for this study, two yttrium (Y) containing glasses (*LY*, *HY*), two cerium (Ce) containing glasses (*LCe*, *HCe*), one glass containing both yttrium and cerium (*YCe*), and one SrO-Na<sub>2</sub>O-SiO<sub>2</sub> control glass (*Con*). The Y<sub>2</sub>O<sub>3</sub> and CeO<sub>2</sub> is incorporated into each glass, with the exception of the control, at the expense of Na<sub>2</sub>O. Glass compositions (mol%) can be found in Table 3-1.

Table 3-1. Glass Compositions in mol% and Surface Area (SA)

	<u>Con</u>	<u>LY</u>	<u>HY</u>	<u>YCe</u>	<u>LCe</u>	<u>HCe</u>
SiO <sub>2</sub>	52	52	52	52	52	52
SrO	24	24	24	24	24	24
Na <sub>2</sub> O	24	20	16	16	20	16
Y <sub>2</sub> O <sub>3</sub>	-	4	8	4	-	-
CeO <sub>2</sub>	-	-	-	4	4	8
SA (g/m <sup>2</sup> )	0.84	0.92	0.93	0.84	0.75	0.68

##### 3.3.1.1. Glass Powder Production

Glass powders were prepared by weighing out appropriate amounts of analytical grade reagents (Fisher Scientific, PA, USA) and ball milling (1 h). The mix was then oven dried (100°C, 1 h), fired (1500°C, 1 h) in a platinum crucible and shock quenched in water. The resulting frit was dried, ground and sieved to retrieve glass particles <20µm.

Glass particles were imaged using a Quanta 200F Environmental Scanning Electron Microscope (FEI, OR, USA) under a vacuum at a pressure of 0.60 torr. The electron beam was used at an accelerating voltage of 20 kV and a spot size of 3.0. Energy dispersive x-ray spectroscopy was carried out using an FEI EDAX system equipped with a silicon-drift detector at an 11 mm working distance, collected full frame for 100 s at a minimum 1000 CPS.

#### 3.3.2. Glass Solubility

##### 3.3.2.1. Surface Area Analysis

Surface area of the glasses was determined using an Advanced Surface Area and Porosimetry, ASAP 2010 System Analyzer (Micrometrics Instrument Corporation, GA,

USA). After oven-drying (100°C) overnight approximately 60 mg of each glass powder (n = 3) was weighed into standard ¾” tubes and loaded into the instrument. Liquid nitrogen, nitrogen and helium gasses were used to purge and obtain isothermal gas absorption on an 11 point scale which was then used to calculate the specific surface area using the Brunauer-Emmett-Teller (BET) method.

#### 3.3.2.2. *Sample Preparation*

Sterile liquid extracts were prepared by weighing out 1 m<sup>2</sup> of each glass powder (n = 3/time period) into glass vials. Vials were covered with aluminum foil and autoclaved. The sterile glass powders were then transferred to sterile 15 mL centrifuge tubes and 10 mL sterile ultra-pure de-ionized (SUPDI) water was added to each tube, including glass-free control tubes. The tubes were sealed and incubated on a rotating tray for 1, 7 and 30 days. Upon removal, each sample was filtered (Amicon Ultra-4 Centrifugal Filters, Fisher Scientific, PA, USA) to separate the liquid extract from the glass powders. A 1.5mL aliquot from each sample extract was removed into a sterile vial to be used for cytocompatibility studies.

#### 3.3.2.3. *pH Analysis*

The pH of each sample extract was measured using an Accumet® Excel XL 15 pH meter (Fisher Scientific, PA, USA). Prior to testing, the pH meter was calibrated using pH buffer standards 4.00±0.02, 7.00±0.02 and 10.00±0.02. The probe was rinsed with DI water and allowed to stabilize in the pH 7 buffer between readings which were taken after the pH value stabilized for 10 s.

#### 3.3.2.4. *Ion Release*

The ion release profile of each glass was measured using Inductively Coupled Plasma–Optical Emission Spectroscopy (ICP – OES) on a Perkin-Elmer Optima 8000 (Perkin Elmer, MA, USA). ICP – OES calibration standards for Si, Sr, Na, Y and Ce were prepared from stock solutions.

### 3.3.3. Glass Cytocompatibility

#### 3.3.3.1. Fibroblast and Osteoblast Viability

L-929 Fibroblasts (ATCC CCL-1) and MC-3T3-E1 Osteoblasts (ATCC CRL-2593) were maintained on a regular feeding regime with Medium 199 Media (w/Earl's balanced salts and L-glutamine) or Minimum Essential Medium (MEM) Alpha Media (w/L-glutamine, ribonucleosides, and deoxyribonucleosides), respectively, both supplemented with 10% fetal bovine serum (FBS) in a cell culture incubator at 37°C/5%CO<sub>2</sub>/95%air atmosphere (Fisher Scientific, PA, USA). Cells were seeded into 96-well plates at a density of 10<sup>4</sup> cells/well and incubated for 24 hrs. Glass extracts and SUPDI water controls, were added to the 100 µL wells in quantities of 10 µL, 25 µL and 50 µL, producing final concentrations by volume of 9%, 20% and 33%. After addition of the extracts the plates were incubated for an additional 24 hrs.

Cytocompatibility was tested using the methyl thiazolyl tetrazolium (MTT) assay. 10 µL of MTT reagent was added to each well and incubated for 4 hrs (37°C/5%CO<sub>2</sub>). After incubation each well was aspirated and 100 µL of MTT solubilization solution (10% Triton X-100 in acidic [0.1 M HCl] Isopropanol) was added, and mixed by gently pipetting at half the well volume (50 µL). Once the crystals were fully dissolved, the absorbance was measured at 570 nm using a µQuant Microplate Spectrophotometer (Biotek Instruments Inc., VT, USA). Media wells with the SUPDI water control samples were used to determine the background effect and a control cell population was assumed to represent 100% viability to normalize the readings.

#### 3.3.3.2. Bacterial Inhibition

Bacterial inhibition of the glass extracts were tested against *E. coli* (ATCC CRM-8739) and *S. aureus* (ATCC 49230) using the broth transmission method. Bacterial stocks were made by plating bacteria from frozen stores onto Lysogeny (LB) agar and Trypticase Soy (TS) agar, respectively, then incubating at 37°C for 24 hrs. Sterile loops were used to extract one colony from each plate, into 5 mL of LB or TS broth and allowed another 24 hrs incubation at 37°C. Agar and broth was made according to ATCC recipes and autoclaved before use.

SUPDI water controls and glass extracts (100  $\mu$ L) were added to 1 mL of sterile bacterial broth in 24-well plates giving a concentration of 9% glass extract. Each well (with the exception of the sterile broth control wells) was then inoculated with 10  $\mu$ L of a 1/50 dilution of the respective bacterial containing broth yielding a bacterial concentration of 1%. After incubation for 24 hrs at 37°C the plates were removed and 100  $\mu$ L (n = 4) from each sample well was pipetted into a 96-well plate. Plates were read at 590 nm using a  $\mu$ Quant Microplate Spectrophotometer for the absorbance. Wells containing sterile broth and SUPDI water controls served as a background measurement and those containing bacteria broth-SUPDI water controls served as the uninhibited bacterial populations. Sample wells were compared against the respective uninhibited populations representing 0% growth inhibition.

#### 3.3.3.3. *Statistical Analysis*

One-way analysis of variance (ANOVA) was employed to compare the difference in cell viability and bacterial inhibition relative to the control populations. Comparison of relevant means was performed using the post hoc Bonferroni test. Differences between groups was deemed significant when  $P < 0.05$ .

#### 3.3.4. **Antioxidant Capacity**

Evaluation of the antioxidant capacity of the glass extracts was conducted using an 2,2'-azino-bis(3-ethylbenzothiazoline-6-sulphonic acid (ABTS) assay and Trolox<sup>®</sup> as a standard for comparison. A 7 mM ABTS, 2.45 mM potassium persulfate solution was prepared in DI water and incubated in the dark at room temperatures for 12 hrs. The solution was then diluted to obtain an absorbance of  $2.55 \pm 0.07$ . A 50 mM Trolox<sup>®</sup> solution was prepared by dissolving 25 mg Trolox<sup>®</sup> in 150  $\mu$ L methanol, and adding 1.747 mL DI water and 103  $\mu$ L 1M NaOH to a final pH of 7.3. Dilutions were made in the range 0.5 mM–10 mM to obtain a Trolox<sup>®</sup> standard curve. Standards and glass extracts (n = 3) were added (25  $\mu$ L) to 0.5 mL ABTS solution in a 1.5 mL centrifuge tube, sealed and vortexed then 100  $\mu$ L (n = 4) of each sample was pipetted into a 96-well plate. Plates were read at 734 nm using a  $\mu$ Quant Microplate Spectrophotometer to obtain the absorbance. A one-way analysis of variance (ANOVA) was employed to compare the difference in antioxidant capacity between time periods for each glass and

between glass extracts. Comparison of relevant means was performed using the post hoc Bonferroni test. Differences between groups was deemed significant when  $P < 0.05$ .

### **3.3.5. Preliminary Cell Adhesion**

Glass (+10 wt% <75  $\mu\text{m}$  PVA) powders (0.15 g/disk) were pressed in a 6 mm  $\varnothing$  stainless steel die at a pressure of 4 tons and subsequently heated to 50°C above the glass transition temperature ( $T_{g+50}$ , previously determined by the authors) for 6 hrs. Disks were buffered for 24 hrs in 199 Media and fibroblasts were seeded onto the disks in 6-well plates at a density of  $10^4$  cells/well and incubated for 24 hrs. Cells were then fixed using the procedure from Wang et al.<sup>155</sup> and imaged using a Quanta 200F Environmental Scanning Electron Microscope under a vacuum at a pressure of 0.60 torr. The electron beam was used at an accelerating voltage of 20 kV and a spot size of 4.0.

## **3.4 RESULTS**

### **3.4.1. Scanning Electron Microscopy (SEM)/Energy Dispersive X-ray (EDX)**

SEM images and EDX generated spectral oxide contributions for each glass powder are presented in Figure 3-1. Images show each glass powder consists of particles <20  $\mu\text{m}$  and some agglomeration is occurring. EDX reveals the presence of each element of interest in the glasses and relative correlation with the as calculated composition.

### **3.4.2. Surface Area Analysis**

Average surface area ranged from 0.68  $\text{m}^2/\text{g}$  for *HCE* to 0.93  $\text{m}^2/\text{g}$  for *HY*. Surface area of each glass powder is presented in Table 3-1 where no significant difference is found between glasses.

### **3.4.3. pH Analysis**

pH of the glass extracts, presented in Figure 3-2, was found to range from 11.2 for *HY* to 11.9 for *Con* after 1 day and increases slightly, though not significantly, over the 7 and 30 day time periods to 11.4 and 12.7, respectively.

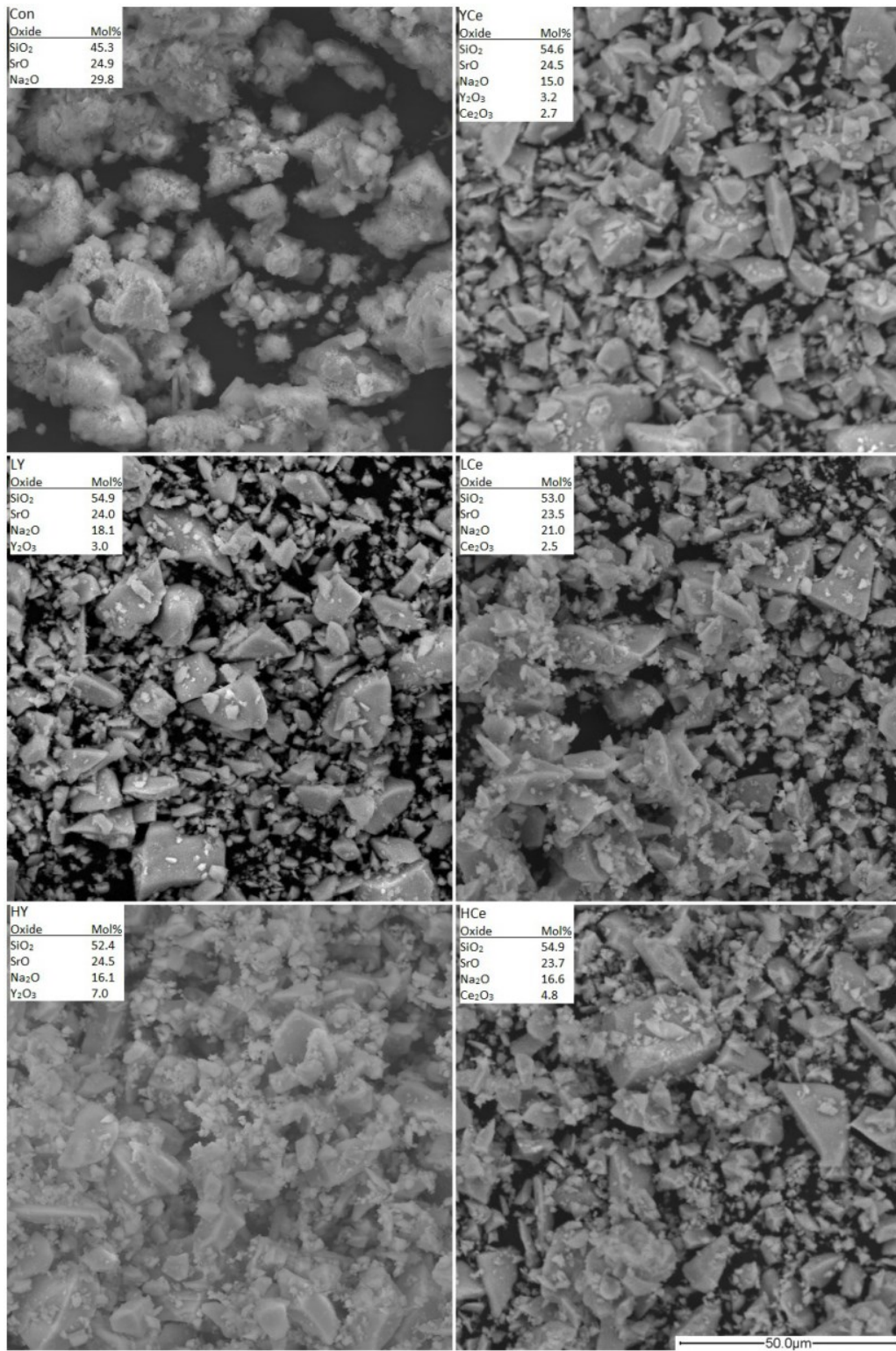


Figure 3-1. SEM images of glass particles at 1000X and EDX generated oxides list.

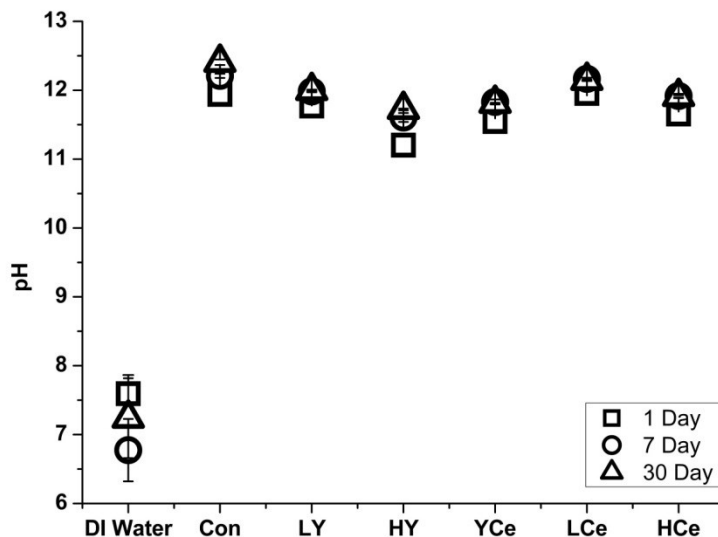


Figure 3-2. pH of liquid extracts from Y/Ce glass series over 1, 7 and 30 days incubation.

#### 3.4.4. Ion Release

Ion release is for all glasses and time periods is shown in Figure 3-3, where Y and Ce are not included as any release was below the detection limit ( $<1 \mu\text{g/mL}$ ). Si release reaches a maximum for *Con* near 16k  $\mu\text{g/mL}$  after 1 d and decreases to 4.5k by day 30. The second highest release of Si is from *LCe* between 1.4k and 1.8k  $\mu\text{g/mL}$  over the 30 days. The remaining glasses release between 400 and 1k  $\mu\text{g/mL}$  over the 30 days without a significant increase or decrease in release between time periods. Similar trends are seen with Na release, where *Con* releases significantly more compared to the Y or Ce containing glasses, from 6.3k after 1 and 7 d decreasing to 3.75k after 30 d. The Y and Ce containing glasses each show a trend of increasing Na release over the 30 d time period, with *LCe*, again, releasing the second greatest quantity of 1.8k  $\mu\text{g/mL}$  after 30 days, followed by *LY*, *HCe*, with *HY* and *YCe* releasing around 500  $\mu\text{g/mL}$  after 30 days. Release of Sr follows the decreasing trend of release over the 30 days for *Con* where a maximum release of 89  $\mu\text{g/mL}$  is released after 1 d, 69  $\mu\text{g/mL}$  after 7 d, and 40  $\mu\text{g/mL}$  after 30 d. The Y and Ce containing glasses each release  $<10 \mu\text{g/mL}$  with the peak occurring after 7 days and subsequent decrease at 30 d below that of the 1 d release.

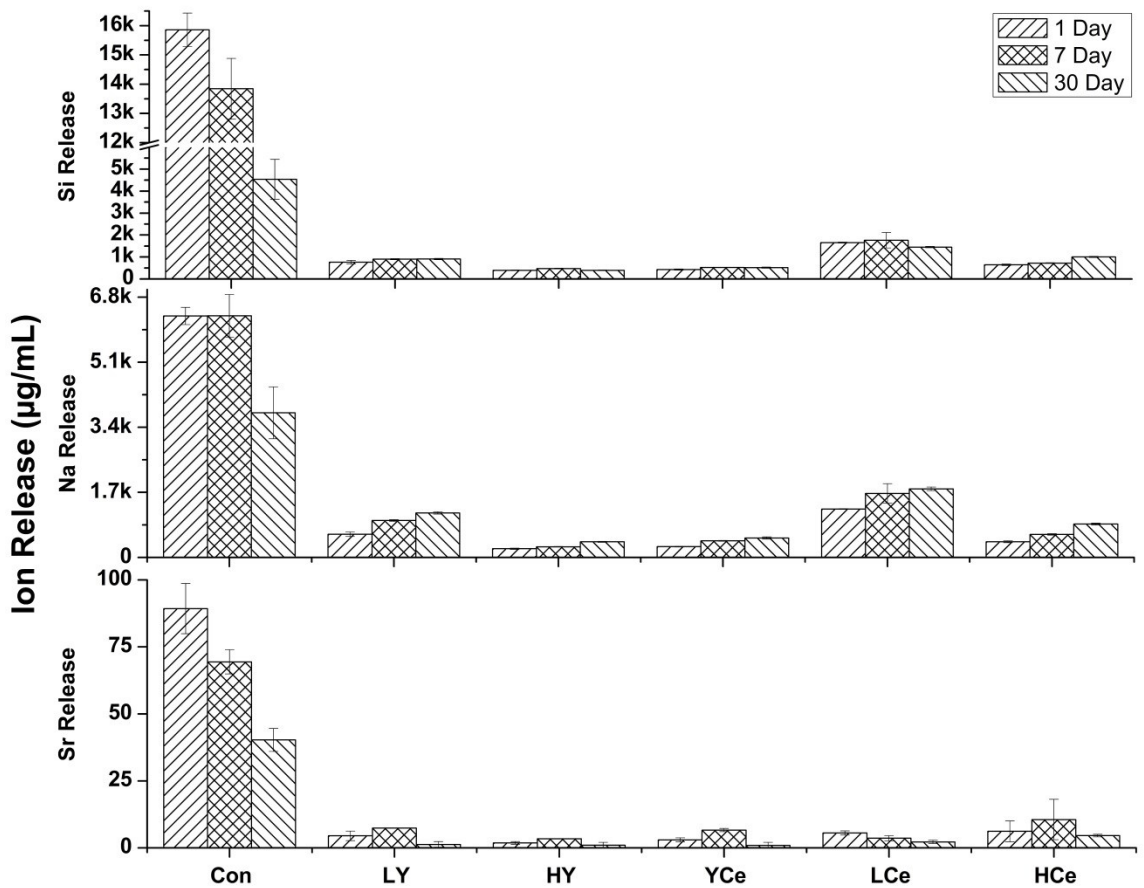


Figure 3-3. Ion release from each glass extract over 1, 7 and 30 days.

### 3.4.5. Fibroblast and Osteoblast Viability

Viability of fibroblast cells after incubation with various concentrations of glass extracts ( $t = 1, 7, 30$  d) is shown in Figure 3-4. At a concentration of 9% the fibroblast viability is reduced to 25% by *Con*, *LY*, and *LCe* with a trend in decreasing viability over the 30 d time period. *YCe* and *HCe* appear to decrease the fibroblast viability at a concentration of 9% but is not found to be significantly different from the control population. At an extract concentration of 20% the viability remains below 25% for *Con*, *LY*, *LCe*, and additionally *HCe*, with the viability dropping to 0% for *Con* at 30 d. This trend continues at the 33% concentration where both 7 and 30 day *Con* extracts produce a viability of 0%. *YCe* does not indicate a significant difference from the control population at the 9% or 20% extract concentrations but indicates a significant drop in viability to

25% with the 1 d extracts at 33% concentration, recovering with the 7 and 30 day extracts. *HY* does not significantly affect cell viability at any concentration or time period.

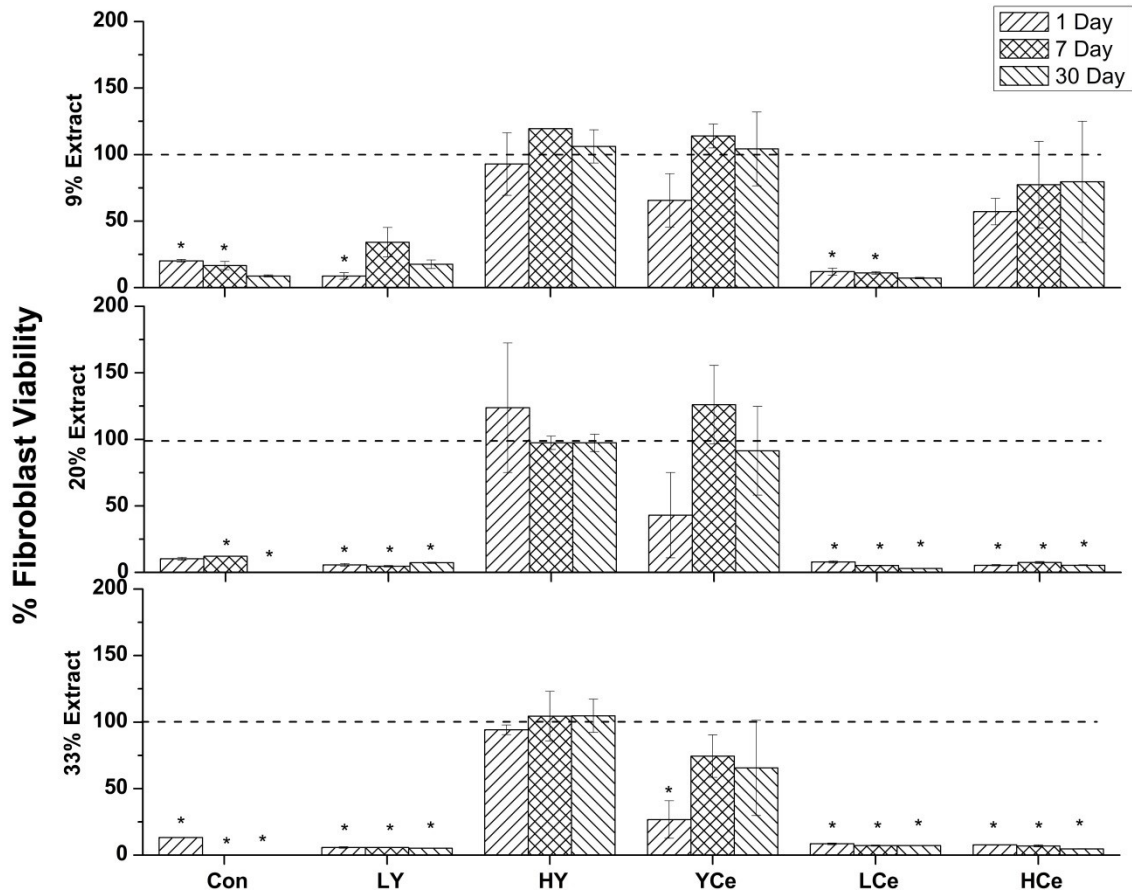


Figure 3-4. Fibroblast viability after incubation with glass extracts at 9%, 20% and 33% concentrations by volume over 1, 7 and 30 days. \* indicates a significant difference ( $P < 0.05$ ) between the control Fibroblast population and the extract incubated populations.

Viability of osteoblast cells after incubation with various concentrations of glass extract ( $t = 1, 7, 30$  d) is shown in Figure 3-5. At a concentration of 9% the osteoblast viability is reduced to 50% by *Con* and *LCe* with a trend in decreasing viability over the 30 d time period. *LY*, *YCe* and *HCe* do not significantly affect osteoblast viability at a concentration of 9%. At an extract concentration of 20% the viability drops to 75%, 0% and 0% for *Con* at 1, 7 and 30 d respectively, and below 25% for *LY*, *LCe* and *HCe* at each time period. *YCe* causes a significant decrease in fibroblast viability below 25%

after 1 day and then increases cell viability after 7 d before dropping back into range with the control population after 30 d. At the 33% concentration *Con* extracts produce a viability of 0% and *LY*, *LCe*, and *HCe* extracts maintain viability below 25%; while *YCe* does not indicate a significant difference from the control population. *HY* does not significantly affect cell viability at any concentration or time period.

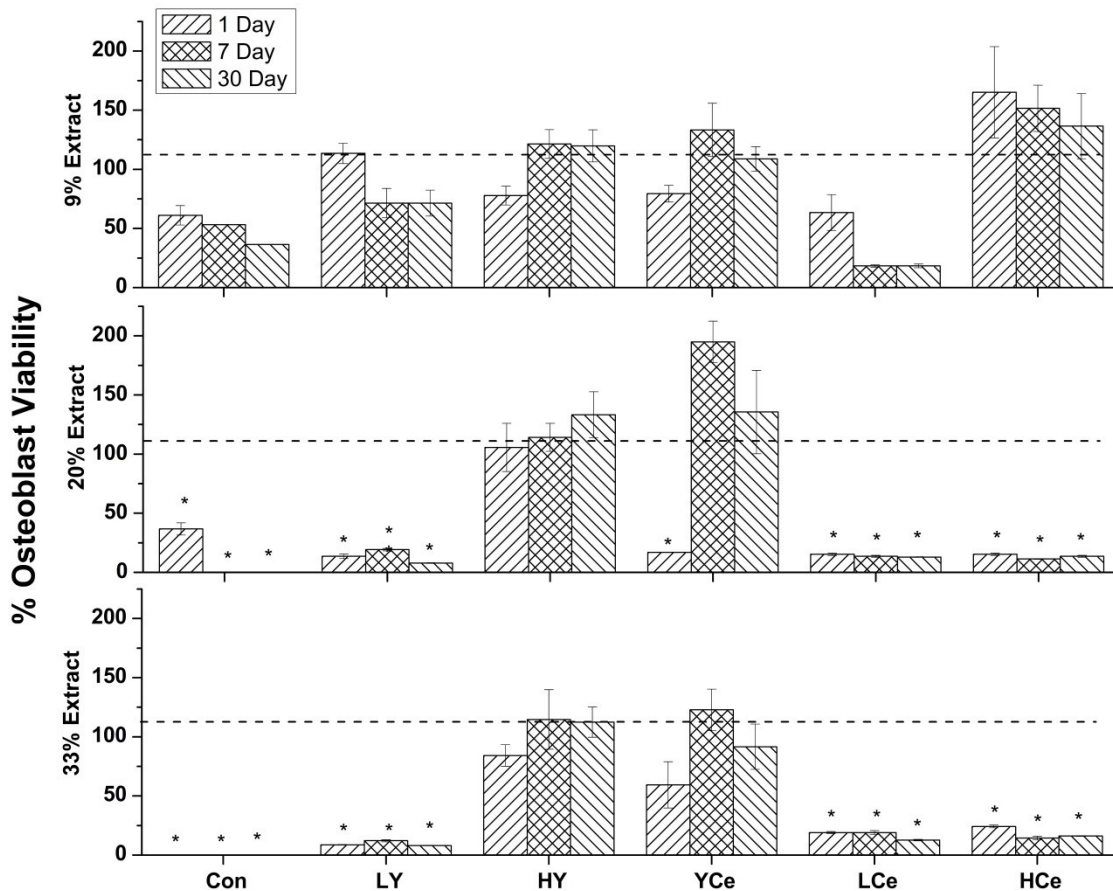


Figure 3-5. Osteoblast viability after incubation with glass extracts at 9%, 20% and 33% concentrations by volume over 1, 7 and 30 days. \* indicates a significant difference ( $P < 0.05$ ) between the control Osteoblast population and the extract incubated populations.

### 3.4.6. Bacterial Inhibition

Bacterial inhibition for each glass extract at a 9% concentration and each bacterial type is shown in Figure 3-6. For both *E. coli* and *S. aureus*, *Con* and *LCe* yield 100% bacterial inhibition. *LY* and the 7 and 30 d *HCe* extracts inhibit *E. coli* growth by 65% while *HY*, *YCe* and 1 d *HCe* extracts inhibit *E. coli* growth by 25% or less. *S. aureus*

inhibition by *LY* was limited to 30% after 1 d, increasing to 75% after 7 d and holding after 30 d. *HY*, 1 and 7 d *YCe* and 1 d *HCe* extracts produced less than 10% *S. aureus* growth inhibition, increasing to 40%, 62% and 45% for 30 d *YCe*, 7 d *HCe* and 30 d *HCe* extracts.

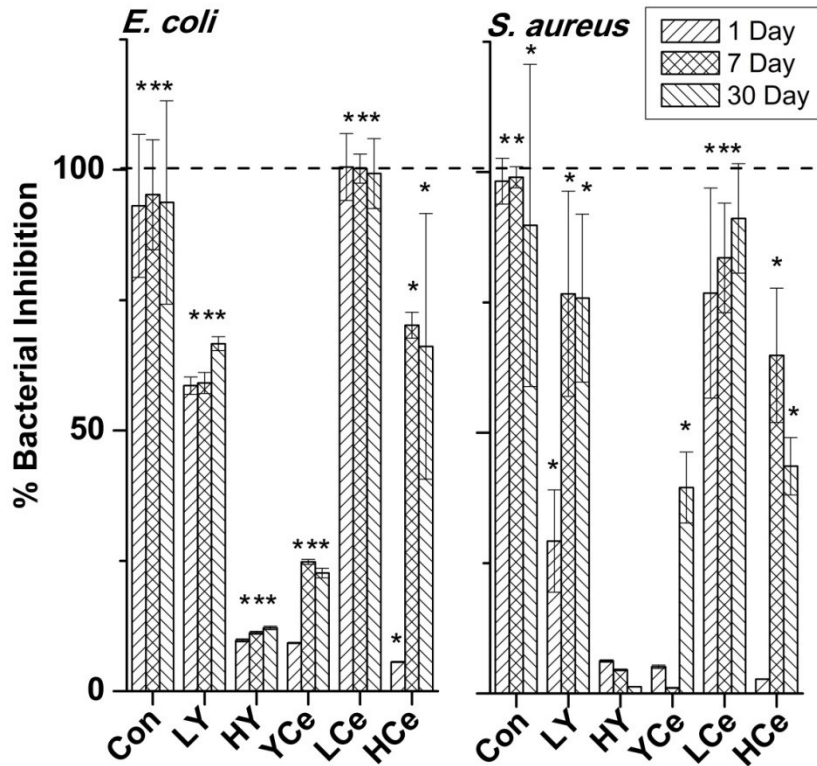


Figure 3-6. *E. coli* and *S. aureus* inhibition after incubation with glass extracts at 9% concentration by volume. \* indicates a significant difference ( $P < 0.05$ ) between the control *E. coli* or *S. aureus* population and the extract incubated populations.

### 3.4.7. Antioxidant Capacity

Antioxidant capacity in mM Trolox<sup>®</sup> equivalency (mMTE) is presented in Figure 3-7. *Con* had the greatest capacity at 8.2-9.5 mMTE followed by *LCe* and *LY* at 5.9-8.5 mMTE and 7.3-7.9 mMTE, respectively. *HCe* capacity falls just below this range from 4.3-5.9 mMTE. *HY* and *YCe* glasses have antioxidant capacity significantly lower at 0.9-1.2 mMTE and 1.9-2.1 mMTE, respectively.

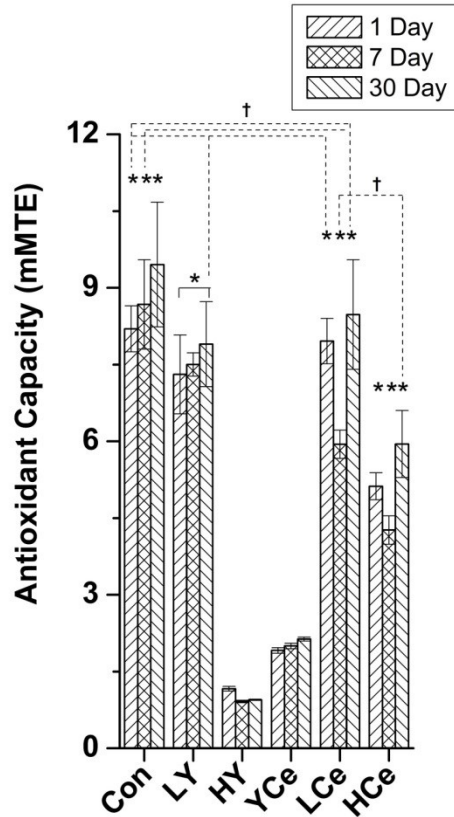


Figure 3-7. Antioxidant capacity of glass extracts relative to Trolox<sup>®</sup>. \* indicates a significant difference ( $P < 0.05$ ) between time periods for each glass; † indicates non-significance between glasses.

### 3.4.8. Fibroblast Adhesion

Considering the cytocompatibility, and antioxidant behavior *Con*, *HY*, and as an intermediate *HCe* glasses were selected for a preliminary evaluation of cell interaction by seeding fibroblasts onto pressed powder disks. SEM images of fibroblast cells after 24 hr incubation are presented in Figure 3-8. While each disk shows the presence of fibroblast cells on the disk surface cell morphology differs between the glasses. Fibroblast cells present on the surface of the *Con* disk are rounded and clustered together, without showing significant attachment to the disk surface or spreading. On both the *HY* and *HCe* disks fibroblast cells are present and appear to form a connected network over the disk surface.

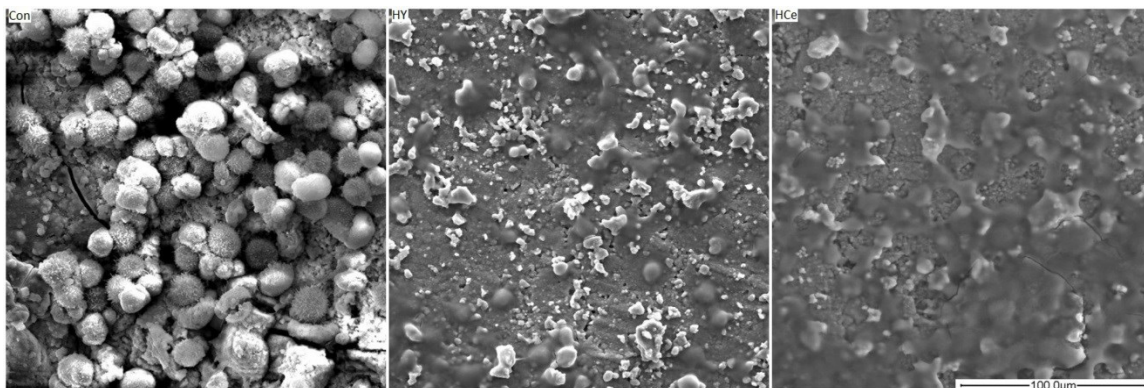


Figure 3-8. SEM images of Fibroblast cells after 24 hr incubation on *Con*, *HY* and *HCe* disks at 500X.

### 3.5 DISCUSSION

With the aim of incorporating Y and Ce to reduce ROS damage associated with nerve injury while retaining biocompatibility, six glasses containing various quantities of Y and/or Ce were synthesized, imaged and incubated in SUPDI water for 1, 7, and 30 days. EDX confirms the relative oxide contribution to each composition and correlates to the calculated compositions. The increase in pH seen is similar to that observed in typical bioactive glasses,<sup>96</sup> where the *Con* glass saw the greatest spike from 11.9 after 1 day to 12.4 after 30 days. There is a direct relationship between the increase in pH and the dissolution of the glass network, relating to the initial exchange of hydrogen ions ( $H^+$ ) with  $Na^+$ . This attack is most pronounced in the *Con* glass with the highest Na content and lack of trivalent cations (Y and Ce) which are not released from the glass network and likely require charge compensation thereby reducing the mobility of the Na and Sr ions which serve this role. In addition, the pH has a direct correlation with the dissolution of silica species into solution based on the surface charge and the extent to which the reaction will be catalyzed;<sup>176</sup> as a result, at higher pH, Si dissolution rates increase. In *Con*, Si release is exceptionally high, though is in accordance with the solubility curves, where up to a pH of 9 the solubility limit is around 120  $\mu\text{g/mL}$  and increases to around 30,000  $\mu\text{g/mL}$  at a pH of 11.5.<sup>108,109</sup> *Con* Si release of 16,000  $\mu\text{g/mL}$  after 1 day is within the solubility limit at a pH of 11.9. The Si concentration in solution decreases after both 7 and 30 days suggesting the Si release approaches the solubility limit between 1 and 7 days and proceeds to precipitate over the 30 day time period.<sup>177</sup> The silica

polymerization/precipitation is associated with the gelation of the liquid sample over time and when buffered with culture media and broth which causes the pH to drop and supersaturation to occur.<sup>178-180</sup> Na and Sr are also released in significant levels in *Con*, where Na release exceeds levels typically found in physiological fluids (2,500-3,500 µg/mL).<sup>110,181</sup> Sr, in the role of replacing Ca, is released in quantities greater than 10 µg/mL which have been found to impede osteoblast mineralization activity *in vitro*.<sup>113,182</sup> Both Na and Sr concentration decreases after 30 days indicating that precipitation of Na/Sr salts or complexes is occurring. Ion release levels for *Con* are excessive for biomaterials applications and therefore require modification to reduce the solubility into an acceptable range.<sup>183</sup>

The pH increase seen in the Y and Ce containing glasses are similar to those seen with the *Con* glass, however exhibit a trend where greater Y or Ce content relates to modestly lower pH values and significantly reduced ion release. This is supported through prior work by the authors which found that Y and Ce increase network rigidity. Si in these glasses is released at a maximum of 1,800 µg/mL in the *LCe* glass after 7 days, followed by *LY*, *HCe*, and at 400 – 500 µg/mL from *YCe* and *HY* where significant changes are not observed over the 1, 7 and 30 day time period. Na concentration increases over the 30 day time period for each glass and reaches a maximum of 1,788 µg/mL for *LCe*, which is within physiological levels. Sr concentrations range from 10.6 to 0.9 µg/mL, levels found to support healthy bone mineralization.<sup>182</sup> In these glass extracts Sr release peaks after 7 days and 30 day values are lower than those seen after 1 day, suggesting the Sr is precipitating out of solution. The precipitation of Sr may be analogous to that observed with Ca in bioactivity testing, where the negatively charged silanol bioactive glass surface is suspected to attract the positively charged Ca or P ions (in solution containing Ca and P) resulting in the deposition of an amorphous CaP layer. Therefore suggesting, when in physiological fluids containing Ca and P a HCA layer doped with Sr may form.<sup>184</sup> Y and Ce release was undetectable in agreement with the literature.<sup>115,116</sup> The immobility of the Y and Ce in the glass network suggests that while they serve as network modifiers, their field strength results in covalent-type bonding that prevents the successful breaking of bonds and reduces mobility through the glassy network. Ion clustering may also contribute, where presence of smaller clusters of

modifying ions has been shown to reduce the rate of dissolution.<sup>87</sup> In studies by Christie et al.<sup>160,164</sup> and Du et al.<sup>158</sup> it was found that Y and Ce tend to form clusters of 2-4 and 1-2 atoms, respectively. These studies also showed that with increasing content, cluster size of both the Y or Ce and of other modifying ions, such as Ca, increases.<sup>158,164</sup> These factors likely reduce solubility of Y and Ce glasses as seen by the significant reduction in ion release compared to that of *Con*. In addition, subtle differences in release can be seen between glasses with different concentrations of Y or Ce, where the lowest release is observed in the glasses with the highest Y and/or Ce content, and secondarily in glasses containing Y over Ce. Therefore general pH and ion release yields the trend: NC > LCe > LY > HCe > YCe > HY which is reflected in cytocompatibility studies.

The high pH and ion release associated with *Con*, causes both fibroblast and osteoblast toxicity; where fibroblasts see a 75% decrease in viability with an extract dose of 9%, and osteoblasts decrease by nearly 50%. Fibroblast and osteoblast toxicity may be attributed to both the excessive ion release and the pH, both which significantly exceed levels found in typical physiological fluids such as simulated body fluid (SBF). This holds for glasses containing only 4 mol% Y or Ce which drop fibroblast viability under 25% at a 20% dose, joined by *HCe* at the 33% dose. These trends directly relate to the release and pH trend seen between the glasses where *Con* is in excess of physiological levels, even accounting for dose and the buffering capacity of the cell media, the environment proves these levels to be inhospitable for fibroblasts. Osteoblasts show viability is maintained above 50% at a 9% dose for most extracts and similar toxicities to those of fibroblasts are seen at the 20% and 33% doses. This may be attributed to a greater inherent buffering capacity in the osteoblast media or resiliency in the osteoblast cells themselves.<sup>185</sup> In either case, minimal toxicity is observed for the *YCe* and *HY* glasses which show the lowest pH increase of all the glasses and similar ion release values; making these glasses the best candidates for use without modification in terms of cytotoxicity.

Bacterial inhibition can be primarily attributed to the pH of the extract. *E. Coli* grows optimally at pH between 6.0 and 8.0, can survive at a pH of 9.2, however once the pH reaches 9.4 *E.coli* is eliminated.<sup>186,187</sup> Similarly, *S. aureus* optimal pH is also between 6 and 8 but have been shown to survive *in vitro* up to a pH of 10.<sup>188-190</sup> All extracts

exceed the pH necessary to eliminate both bacterial types, however it can be seen that not all samples eliminate bacteria, and for *YCe* and *HCe* inhibition can be affected by dose. This occurs due to the buffering capability of the LB and Tryptic Soy broths used where 9%, 20%, and 33% doses produce variable increases of broth pH in addition to ion content. It is known that both bacteria types are sensitive to Na, however concentrations released by the glasses do not approach those necessary to reduce the water activity ( $a_w$ ) to levels shown to affect bacterial survival and growth.<sup>191,192</sup> However, another consideration with the presence of Na in the extracts, is it has been shown to reduce the ability of *E. coli* to adapt to alkaline environments by disrupting their proton exchange mechanisms.<sup>193</sup> Therefore, it is suggested that pH is to be attributed to the bactericidal characteristics where the extracts are producing an increase in pH where at some concentrations, exceeds the buffering capacity of the broth affecting bacterial survival. The glasses showing the greatest antibacterial potential are those also producing the greatest fibroblast and osteoblast cytotoxicity, and therefore require modification for use as a biomaterial.

Antioxidant capacity of these glass extracts is observed through ABTS assay, where *Con* shows the greatest potential, with the other glasses following the same trend seen throughout this study. The ABTS assay shows stability up to pH values of 13 (95% confidence) and therefore antioxidant capacity is attributed to the glass dissolution. Considering Na and Sr will exist as cations in solution any role in the in the antioxidant behavior of the extracts is unlikely. However, the dissolved Si may indicate a source of the observed reduction; as the Si-O network is broken there is a quantity of dissolved silica in solution most commonly ortho-silicic acid at a pH between 4 and 9.<sup>173</sup> At higher pH (greater than 8) it has been shown polymerization of the ortho-silicic acid occurs producing a variety of silicic acid species carrying a charge from -1 to -4 at a pH of 12.<sup>194-196</sup> The existence of these negatively charged species may account for the neutralization of the ABTS radical cation by electron donation or through hydrogen bonding.<sup>197</sup> This is supported in a study by Preari et al. which found a supersaturated solution of silicic acid molecules with hydrogen bond donating (HBD) ability was stabilized by polyethylene glycols (PEG) through hydrogen bonding with the hydrogen-accepting PEG O atoms.<sup>197</sup> Therefore, potential for ROS scavenging can be related to the

quantity of dissolved silica in the extracts where *Con* shows the highest release of Si as well as the greatest ROS scavenging ability and *HY* the opposite. In addition, it can be seen that over the 30 day time period the antioxidant potential slightly increases for the *Con*, *LY*, *LCe* and *HCe* glass extracts while no effect is observed for the *HY* and *YCe* glass extracts though the Si release is stable for Y and Ce containing glasses and decreases for *Con*. This is likely due to a maximum concentration of the negatively charged silicic acid polymers that can be generated with a given Si concentration, at a given pH.<sup>180,196</sup> For the *LY*, *LCe* and *HCe* glasses, at a stable Si concentration, a slight increase in pH observed over time may produce more charged species and an associated increase in antioxidant capacity. In the *Con* extracts, though overall Si concentration decreases, saturation of charged silicic acid species remains consistent and responds to the slight increase in pH corresponding to the slight increase in antioxidant capacity. Therefore, increase ROS scavenging over time for *Con* is similarly attributed to the slight increase in pH. Further research is required to clarify the mechanism of antioxidant behavior in these extracts, and potential for enhancement through processing.

Overall, *Con* showed the greatest cytotoxicity, bacterial inhibition and antioxidant potential while *HY* presented the inverse. *HCe* was selected as an intermediate between the two extremes to test the interaction of fibroblasts with the glass surfaces based on cell morphology. While all three glasses supported cells on the surface, cell attachment and round morphology suggests the cells are not compatible with the *Con* surface, and may be advancing into a cell death cycle. The *HY* and *HCe* glasses show the cells attached and spread across the glass surfaces suggesting in accordance with the cytocompatibility studies that these glasses do not pose a toxicity risk and are a suitable surface for cell growth.

### **3.6 CONCLUSION**

The ability of bioactive glasses to interact with physiological fluids and induce the deposition of a HCA layer is dependent on the dissolution characteristics, but more important is the effect the dissolution products have on the extracellular fluids and adjacent cells. This work has shown *Con* to release Si, Na, and Sr at levels that are in excess of those seen in typical physiological fluids. As a result, and in association with high pH, cytotoxicity is seen with fibroblasts, osteoblasts and both bacterial types.

Glasses containing Y or Ce show reduced solubility where release is higher for *LCe* and *LY* in comparison with *YCe* and *HY*, but are retained within levels seen in physiological fluids, however, they are still associated with relatively high pH, which produces significant cytotoxicity. *HCe* falls in the middle of the range and exhibits concentration dependent cytotoxicity, while *YCe* and *HY* do not cause pronounced fibroblast, osteoblast or bacterial toxicity. Antioxidant capacity is greatest in *Con* where the presence of silicic acid is suspected to neutralize the ABTS radical. However, all glasses have antioxidant capacity in the mMTE range and therefore may provide neural protection from ROS species produced after nerve injury. Preliminary work testing the fibroblast response to the glass surfaces support cytocompatibility studies where *HY* and *HCe* caused limited toxicity and shows fibroblast adhesion and spreading on the glass surfaces. The inverse relationship observed between cytocompatibility and antioxidant capacity is less than ideal and therefore modification of these glasses using thermal treatments to produce crystallinity in the glasses and potentially improve their cytocompatibility by reducing solubility and enhancing antioxidant capacity will be the subject of future studies.

Therefore, the following chapter focuses on thermally inducing the formation of crystalline phases in the glasses. Two thermal treatments are employed, one at 50°C above the  $T_g$ , ( $T_{g+50}$ ) and the other at  $T_{c1}$ , noted by “A” and “S” respectively. In the interest of sample size the control, *Con* and three best performing Y and Ce doped glasses, in terms of biocompatibility (*HY*, *YCe*, *HCe*), have been selected for the work herein. Identification of the phases generated, observation of surface features, and analysis of ion release will provide an indication of the potential effects on bioactivity and biocompatibility. In addition, antioxidant capacity is again evaluated, where greater insight on the mechanism and potentially correlations between phases and ROS scavenging ability may be made.

# CHAPTER 4 - EFFECT OF CRYSTALLIZATION ON THE SOLUBILITY AND ANTIOXIDANT POTENTIAL OF $Y_2O_3$ AND $CeO_2$ DOPED $SiO_2$ - $SrO$ - $Na_2O$ GLASS-CERAMICS.<sup>3</sup>

## 4.1 ABSTRACT

Crystalline phase generation of a  $0.52SiO_2$ - $0.24SrO$ -( $0.24-x$ ) $Na_2O$ - $xMO$  glass-ceramic series (where  $x = 0.08$  and  $MO = Y_2O_3$  or  $CeO_2$  and processing temperatures were  $50^\circ C$  above the glass transition for annealed (A)-lower temp, or the 1<sup>st</sup> crystallization temperature for sintered (S)-higher temp) is investigated through X-Ray Diffraction (XRD) and Scanning Electron Microscopy (SEM). The prominent phase for *Con* (not containing Y or Ce) is a sodium-strontium-silicate while yttrium (Y) and cerium (Ce) containing glass-ceramics show sodium-Y/Ce-silicate and oxide phases. SEM imaging of the disk surface shows the presence of Na rich regions in the Y and Ce containing glasses and multiple distinct phases including Ce crystallites in the *HCe-S* glass-ceramic. Disk shrinkage during thermal processing ranges from 1-7% for *Con-A/S*, *HY-A/S*, *YCe-A/S* and *HCe-A* in both diameter and thickness; while *HCe-S* disks shrink 17% in diameter and expand 60% in thickness. Ion release of Si and Na into simulated body fluid (SBF) are greatest from the *Con-A* disks at  $1550 \mu g/mL$  and  $4475 \mu g/mL$ , respectively, though comparable with levels released from *Con-S*. Release from the Y and Ce containing disks reached  $320 \mu g/mL$  for Si and  $630 \mu g/mL$  for Na. Antioxidant capacity was evaluated using the ABTS assay where ground disks and extracts from disk incubation in SBF were tested. Ground, un-incubated disks outperformed incubated disks, which in turn exceeded antioxidant levels reached with all extracts. The range of antioxidant capacity for all samples was  $3.9 - 0.31$  mMTE. The preservation of dissolution potential and antioxidant capacity with thermal treatment maintains the candidacy of these glasses for evaluation in terms of bioactivity.

---

<sup>3</sup> Under review; Co-authors: Timothy J. Keenan, Aisling Coughlan, Anthony W. Wren.

## 4.2 INTRODUCTION

Biological response to nerve injury includes: influx of monocytes, lymphocytes, and inflammatory mediators, activation of microglia and astrocytes, formation of the glial scar and is accompanied by differences in the new extracellular matrix (ECM) and changes in the extracellular fluid composition where calcium ( $\text{Ca}^{2+}$ ), glutamate, aspartate and iron are commonly released stimulating the production of reactive oxygen species (ROS) at the site.<sup>18,28-30,33</sup> While these are natural repair mechanisms they often result in degeneration of the axon at the site of severance.<sup>33-37</sup> This work aims to mediate the effect of biologically generated ROS through composition and processing modification of a bioactive glass series.

Ion release and surface dissolution of bioactive glasses is a highly desirable therapeutic characteristic resulting in biodegradable properties when immersed in a hydrated medium. This characteristic is essential for initiation of the bioactive cascade resulting in the deposition of a hydroxycarbonate apatite (HCA) surface layer and subsequent integration with host tissues. The released ions have been shown, in appropriate quantities to be therapeutic, where the most commonly investigated ions Si, Ca and P encourage osteogenesis.<sup>101</sup> If however, the ion release rate is excessive or associated spikes in pH are not accommodated by the dynamic physiological environment, toxicity can be observed. Previous work by the authors on these compositions has shown both osteoblast and fibroblast toxicity through cell viability assays as a result of rapid glass dissolution.<sup>198,199</sup> In an effort to alter the dissolution behavior of bioactive glasses two techniques are considered: compositional adjustments and partial crystallization.<sup>119</sup> Common compositional adjustments focus on the inclusion of ions such as Sr, Ti, Mg, and Al which have been shown to increase network rigidity and decrease glass dissolution.<sup>93,94,137,200</sup> In many cases the composition is selected with the aim of providing specific therapeutic effects and alteration is not desirable. In this work the composition was formulated with two goals; the first with the aim of producing a glass that will not contribute to excess calcium (Ca) accumulation occurring at the site of nerve injury.<sup>34,35</sup> Therefore, Sr was utilized in place of Ca as they have previously been shown to play similar roles in both the structure of bioactive glasses and also within the body.<sup>147,184,201</sup> As such, further alteration of the Sr content was not considered desirable.

In addition, Y and Ce are also included in these glass formulations as they have been shown to increase the stability of the glass network and decrease dissolution.<sup>198,202</sup> Additional network forming ions may only produce a marginal decrease in glass dissolution and convolute the determination of the effect Y and Ce have on the properties of these glasses. The effects of Y and Ce are of significant interest as excess Ca not only results in calcination and excitotoxicity, but also triggers the production of ROS at the injury site. This causes problems in adjacent tissues, where under oxidative stress, a reduction in the ability of the nerve tissue to regenerate and also supporting tissues to aid in recovery is evident.<sup>203</sup> Y and Ce have been incorporated with the aim of harnessing the ROS scavenging abilities described by Schubert et al.<sup>37</sup> In this study, yttria and ceria nanoparticles were found to directly scavenge ROS and provide neuroprotection to cells under oxidative stress, and has been supported in subsequent work.<sup>37,204</sup> The antioxidant capacity is attributed to their structure as oxides. In light of these studies, thermal treatment of the glasses may result in the development of Y and Ce oxide phases capable of ROS scavenging. Therefore, in an effort to reduce the dissolution and produce ROS scavenging Y and Ce oxide phases, glasses will be thermally treated at high and low temperatures to produce glass-ceramics. These glass-ceramics will be evaluated using XRD, SEM, and shrinkage to determine the phases produced and resulting differences in physical properties. Dissolution will be evaluated based on inductively coupled plasma-optical emission spectroscopy (ICP-OES) ion release and antioxidant capacity will be evaluated for both ground disks and extracts using the ABTS assay. The work herein aims to characterize the properties and antioxidant potential of Y/Ce glass-ceramics for reducing oxidative stress after nerve injury.

## **4.3 EXPERIMENTAL**

### **4.3.1. Glass Synthesis**

Four glasses of varying composition were formulated for this study, one containing yttrium (*HY*), one with cerium (*HCe*), a glass containing both Y and Ce, (*YCe*), and one SrO-Na<sub>2</sub>O-SiO<sub>2</sub> control glass, (*Con*). The Y<sub>2</sub>O<sub>3</sub> and CeO<sub>2</sub> is incorporated into each glass at the expense of Na<sub>2</sub>O. Glass compositions (mol%) can be found in Table 4-1.

Table 4-1. Glass Compositions in mol%

	<u>Con</u>	<u>HY</u>	<u>YCe</u>	<u>HCe</u>
SiO <sub>2</sub>	52	52	52	52
SrO	24	24	24	24
Na <sub>2</sub> O	24	16	16	16
Y <sub>2</sub> O <sub>3</sub>	-	8	4	-
CeO <sub>2</sub>	-	-	4	8

Glass powders were prepared by weighing out appropriate amounts of analytical grade reagents (Fisher Scientific, PA, USA) and ball milling (1 h). The mix was then oven dried (100°C, 1 h), fired (1500°C, 1 h) in a platinum crucible and shock quenched in water. The resulting frit was dried, ground and sieved to retrieve glass particles <20 µm. Glass powders were ball milled for 24 hrs with <75 µm polyvinyl alcohol (PVA) added at 10 wt% to act as a binder.

#### 4.3.2. Thermal Analysis

Hot stage microscopy (HSM) (Mistura 3.32) was used to obtain the sintering temperature ( $T_s$ ) at 5% height reduction, for each glass ( $n = 1$ ). Samples were formed using glass particulate mixed with Isopropyl Alcohol pressed into a stainless steel die. The samples were then ejected onto an alumina plate and centered in the HSM furnace for optimal imaging. The samples were heated at a rate of 10°C/min from 30°C to 400°C, 5°C/min up to 975°C, and 2°C/min to the final temperature of 1300°C, images were collected every 12 s.

A SDT Q600 Simultaneous Thermal Gravimetric Analyzer-Differential Scanning Calorimetry (TGA-DSC) (TA Instruments, DW, USA) was used to obtain a thermal profile of each glass-PVA particulate ( $n = 1$ ), specifically monitoring the PVA burnout, as the  $T_g$  and crystallization temperatures have been previously determined.<sup>202</sup> A heating rate of 10°C/min was employed in an air atmosphere using alumina as a reference in a matched platinum crucible. Sample measurements were carried out every six seconds between 30°C and 500°C. TA Universal Analysis software (TA Instruments, DW, USA) was used to process the data.

#### 4.3.3. Disk Production

A 12 mm Ø stainless steel die was used to press 0.5 g of powder at a pressure of 8 tons. The disks were heat treated at two processing temperatures ( $T_{p1}$  and  $T_{p2}$ ), where the

heating profile and processing temperatures are given in Figure 4-1. Processing temperatures were selected at the glass transition ( $T_g$ ), 50°C above  $T_g$  ( $T_{g+50}$ ), sintering ( $T_s$ ), and 1<sup>st</sup> crystallization ( $T_{c1}$ ) temperatures for each glass individually. Thermally treated disks are denoted by annealed disks (A), heated to  $T_g/T_{g+50}$ , and sintered disks (S), heated to  $T_s/T_{c1}$ .

Disk thickness and diameter were measured with digital calipers before and after thermal treatment ( $n = 15$ ). Averaged values for each glass-thermal treatment combination were used to calculate the average diameter and thickness of each disk type. The shrinkage was calculated according to the following equation:

$$\text{shrinkage (\%)} = \frac{x_i - x_t}{x_i} 100 \quad (4.1)$$

where  $X_i$  = the initial average thickness or diameter, and  $X_t$  = the average thickness or diameter after thermal treatment.

#### **4.3.4. X-Ray Diffraction (XRD) of A/S Disks**

Diffraction patterns were collected using a Phaser D2 X-ray Diffraction Unit (Bruker AXS Inc., WI, USA). Glass-ceramic disks were ground (<20  $\mu\text{m}$ ) and ( $n = 1$ ) packed into zero background sample holders. A generator voltage of 40 kV and a tube current of 30 mA was employed. Scattering patterns were collected in the range  $10^\circ < 2\theta < 70^\circ$ , at a scan step size  $0.02^\circ$  and a step time of 10 s.

#### **4.3.5. Scanning Electron Microscopy (SEM)**

SEM images of the disk surfaces ( $n = 1$ ) were collected using a Quanta 200F Environmental Scanning Electron Microscope under a vacuum at a pressure of 0.60 torr. The electron beam was used at an accelerating voltage of 20 kV and a spot size of 3.0.

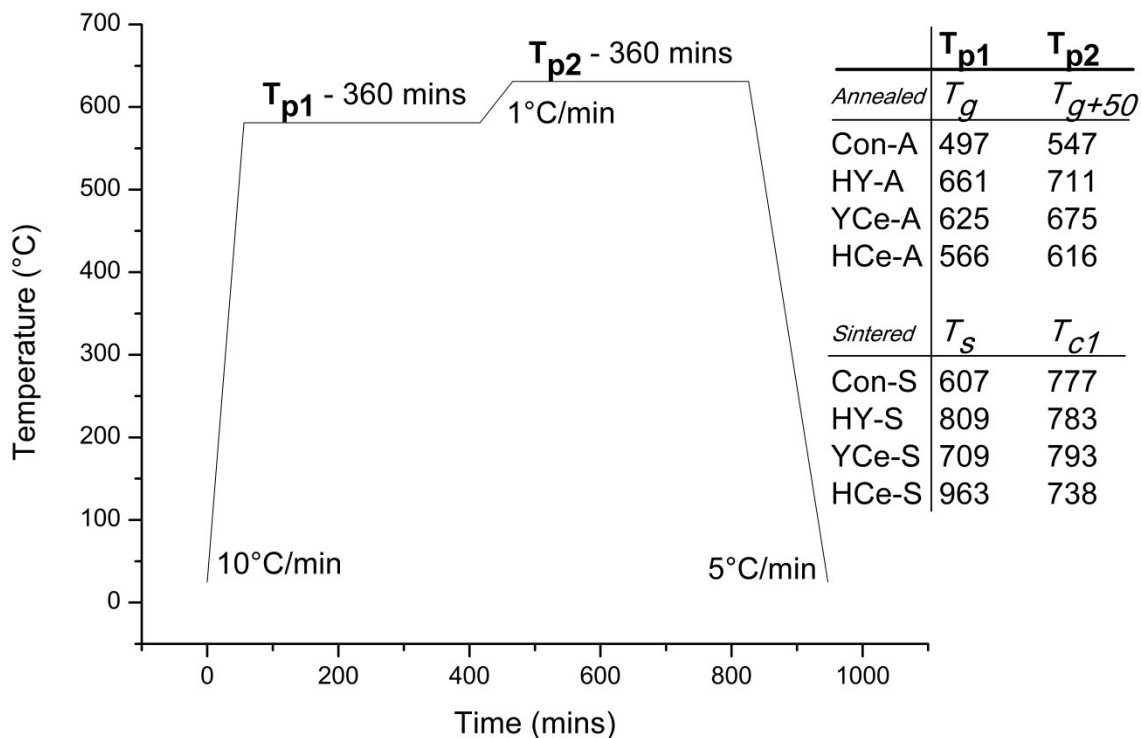


Figure 4-1. Thermal treatment profile and processing temperatures for annealed and sintered disks.

#### 4.3.6. ICP-OES Ion Release

Sterile liquid extracts were prepared by incubating glass-ceramic disks ( $n = 3/\text{time period/composition}$ ) in sterile 15 mL centrifuge tubes with 5 mL simulated body fluid (SBF) due to the ion content mimicking that of human blood plasma, prepared by the method described by Kokubo et al.<sup>110</sup> Dry disks in tubes without SBF ( $t = 0/\text{“unincubated”}$ ) and tubes containing only SBF were used as controls. SBF containing tubes were sealed and incubated for 1, 7 and 14 days. Upon removal, each sample was filtered (Amicon Ultra-4 Centrifugal Filters, Fisher Scientific, PA, USA) to ensure particle free extracts. The ion release profile of each glass was measured using Inductively Coupled Plasma–Optical Emission Spectroscopy (ICP – OES) on a Perkin-Elmer Optima 8000 (Perkin Elmer, MA, USA) with a detection limit  $<0.1 \mu\text{g/mL}$ . ICP – OES calibration standards for Si, Sr, Na, Y, and Ce, were prepared from stock solutions (Perkin-Elmer,

MA and Fisher Scientific, PA, USA). Na ion content in SBF solution is presented as the difference in Na ion content of incubated samples relative to SBF-only samples.

#### 4.3.7. Antioxidant Capacity

Evaluation of the antioxidant capacity of the glass-ceramic disks was conducted using an 2,2'-azino-bis(3-ethylbenzothiazoline-6-sulphonic acid (ABTS) assay and Trolox<sup>®</sup> as a standard for comparison. A 7 mM ABTS, 2.45 mM potassium persulfate solution was prepared in DI water and incubated in the dark at room temperatures for 12 hrs. The solution was then diluted to obtain an absorbance of  $2.55 \pm 0.07$ . A 50 mM Trolox<sup>®</sup> solution was prepared by dissolving 25 mg Trolox<sup>®</sup> in 150  $\mu$ L methanol, and adding 1.747 mL DI water and 103  $\mu$ L 1M NaOH to a final pH of 7.3. Dilutions were made in the range 0.5 mM–10 mM to obtain a Trolox<sup>®</sup> standard curve. Standards, glass-ceramic powders, and extracts ( $n = 3$ ) were added (10 mg or 25 $\mu$ L) to 0.5 mL ABTS solution in a 1.5 mL centrifuge tube, sealed and vortexed (ground disk samples were centrifuged using an 5415 D centrifuge, Eppendorf, Westbury, NY, USA at 3000 rpm for 2 min) then 100  $\mu$ L ( $n = 4$ ) of each sample was pipetted into a 96-well plate. Plates were read at 734 nm using a  $\mu$ Quant Microplate Spectrophotometer to obtain the absorbance. A one-way analysis of variance (ANOVA) was employed to compare the difference in antioxidant capacity between time periods for each glass and between glass-ceramic powders/extracts. Comparison of relevant means was performed using the post hoc Bonferroni test. Differences between groups was deemed significant when  $P < 0.05$ .

## 4.4 RESULTS

### 4.4.1. Thermal Analysis

Glass-PVA powders were monitored for burnout of the polymer phase used to stabilize the powder pellets during pressing (shown in Figure 4-2). PVA weight loss between 200°C and 500°C was 81%, followed by *Con-PVA* at 11%, and the Y and Ce containing glasses-PVA from 7-8%.

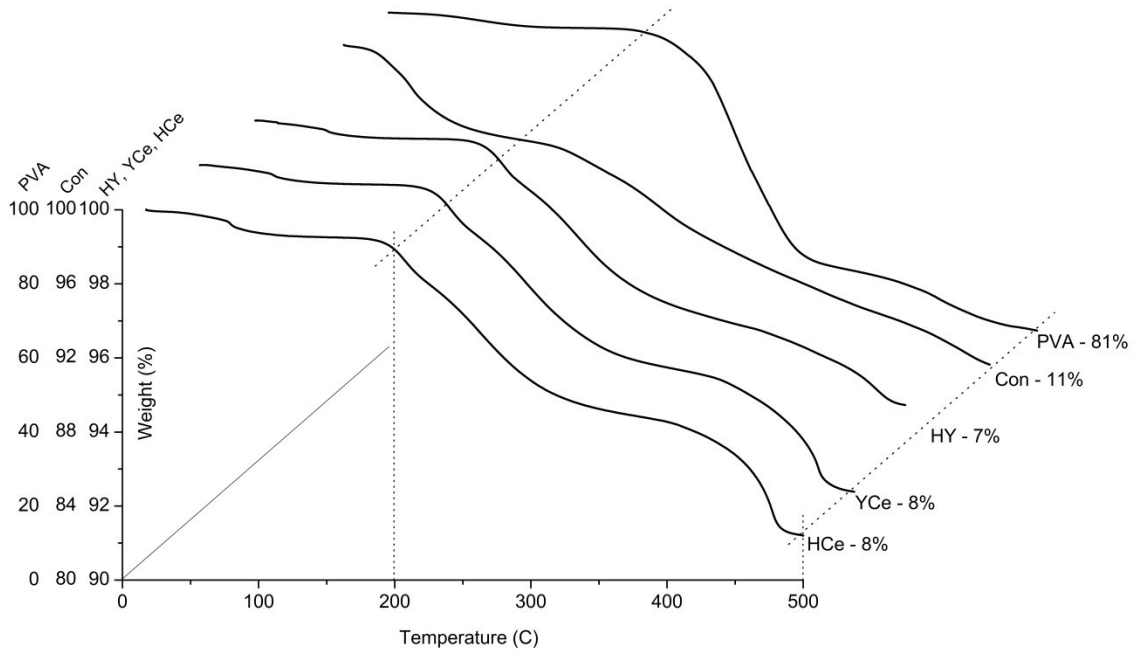


Figure 4-2. Weight change of PVA and glass-PVA powders up to 500°C.

#### 4.4.2. Shrinkage

Shrinkage of the disks is represented in Figure 4-3. Thickness shrinkage of the disks was similar between *A* and *S* samples for *Con*, *HY* and *YCe* ranging from 2-4%. Diameter shrinkage ranged from 1% (*HY-A*) to 7% (*Con-S* and *YCe-S*), with the remaining disks at 4-5%. *HCe-A* shrinkage was within the previously mentioned ranges at 3% for thickness and 4% in diameter, however *HCe-S* thickness expanded by 60% with a diameter shrinkage of 17%.

#### 4.4.3. X-Ray Diffraction(XRD) and Scanning Electron Microscopy(SEM)

XRD and SEM comparison of *A* and *S* disks are shown in Figures 4-4 through 4-7. Evolution of crystallinity can be seen for each set of disks where *A*-disks exhibit partial crystallinity and *S*-disks show fully crystalized structures. A sodium-strontium-silicate is the primary phase associated with the *Con* disks and is also present in the Y containing disks though the primary phase becomes a sodium-strontium-yttrium-silicate for each. Ce is present as a sodium-cerium-silicate in *YCe-A*, as sodium-cerium-oxide in *YCe-S* and as a sodium-cerium-oxide and ceria in the *HCe-S* disks. There is also a recurring strontium-

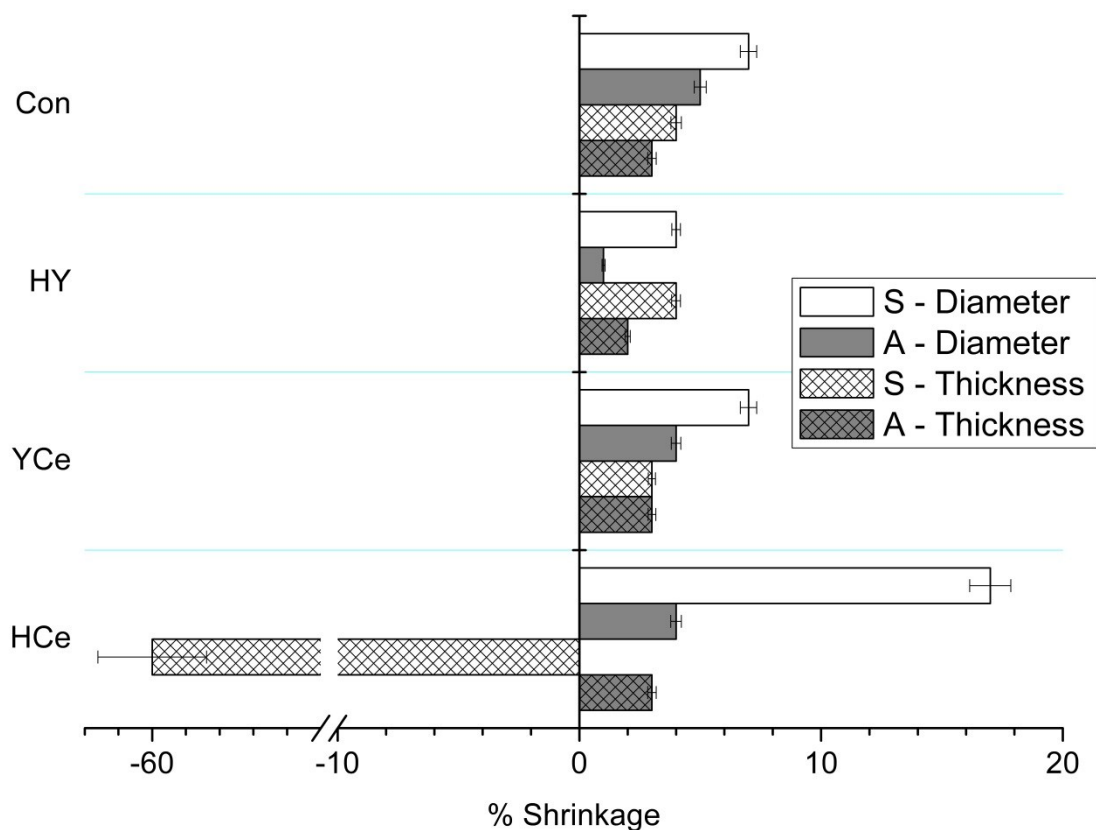


Figure 4-3. % shrinkage of disks after thermal treatment.

silicate phase in each *S* XRD pattern, the molecular formula (MF) for which can be found in Table 4-2, along with the MF and PDF information for each identified phase. Through the associated SEM images it can be seen that *Con* disks show minimal porosity and appear to have a reacted surface layer. *HY*, *YCe* and *HCe-A* disks have visible porosity at a magnification of 30X and distinct packed and sintered particle morphology as well as regions of dark crystallite growth. *HCe-S* disks show both porosity and crystallite growth and at high magnification the presence of multiple phases.



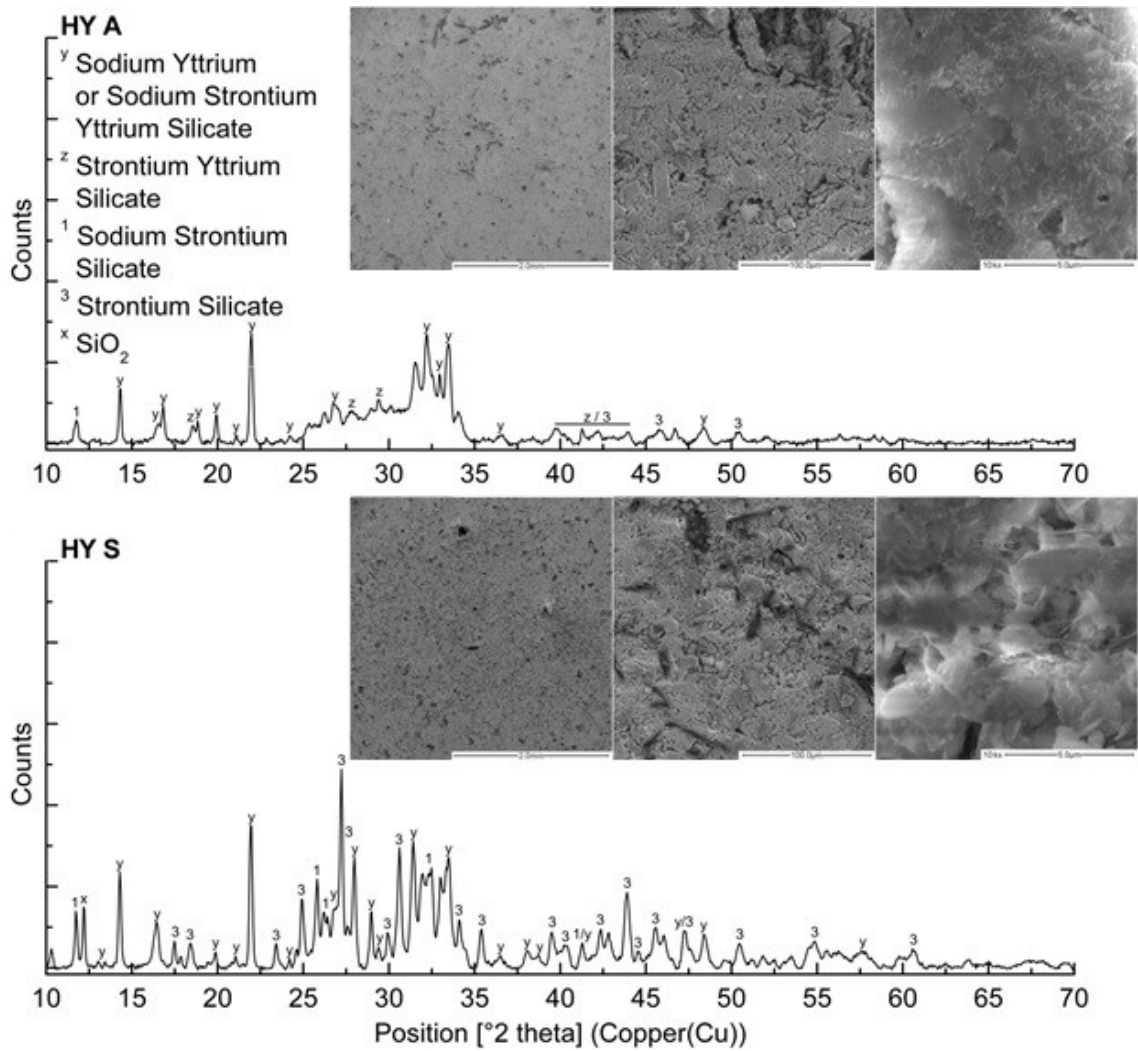


Figure 4-5. XRD patterns and SEM images at 30X, 500X and high magnification of thermally treated *HY* disks.

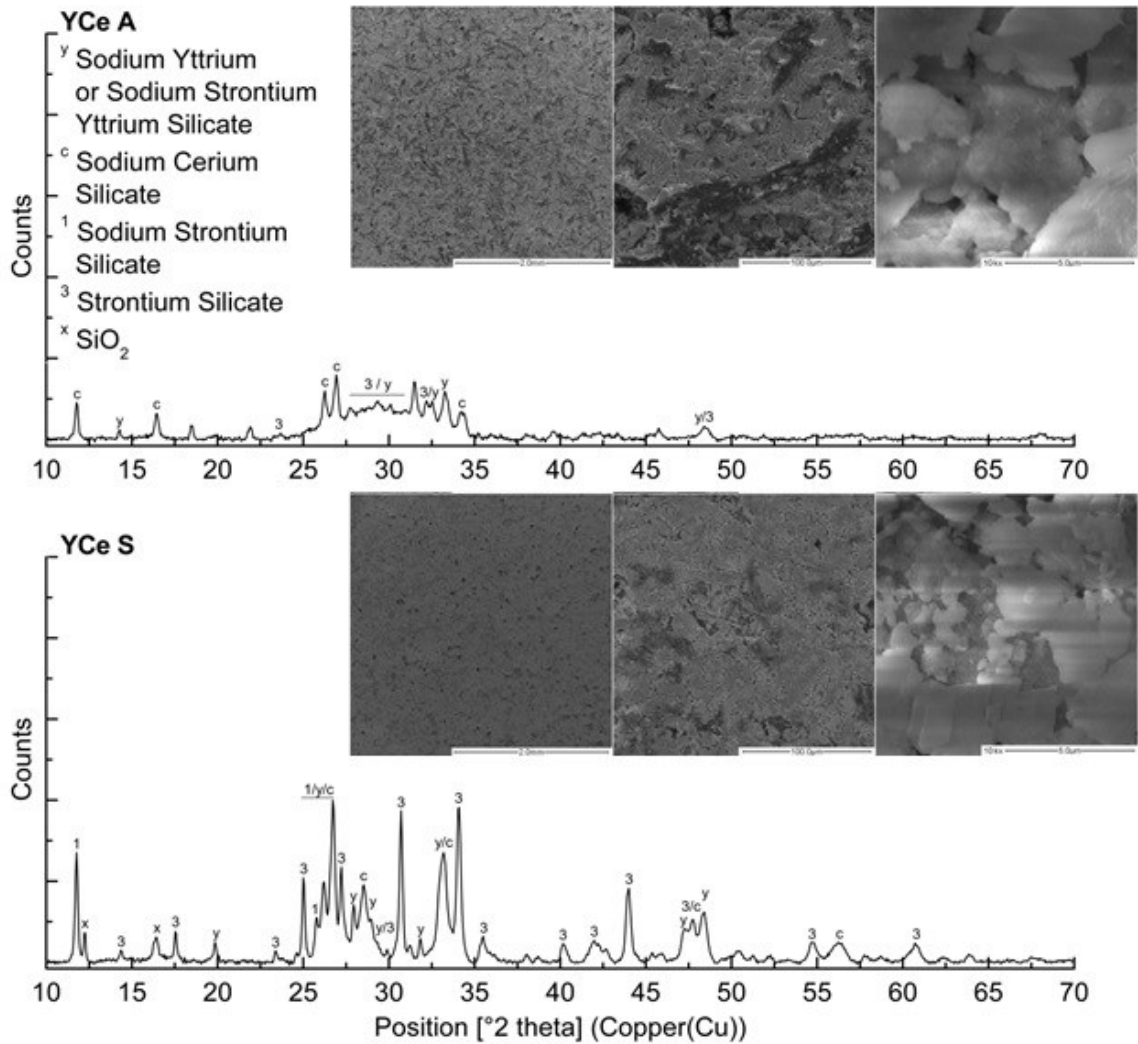


Figure 4-6. XRD patterns and SEM images at 30X, 500X and high magnification of thermally treated YCe disks.

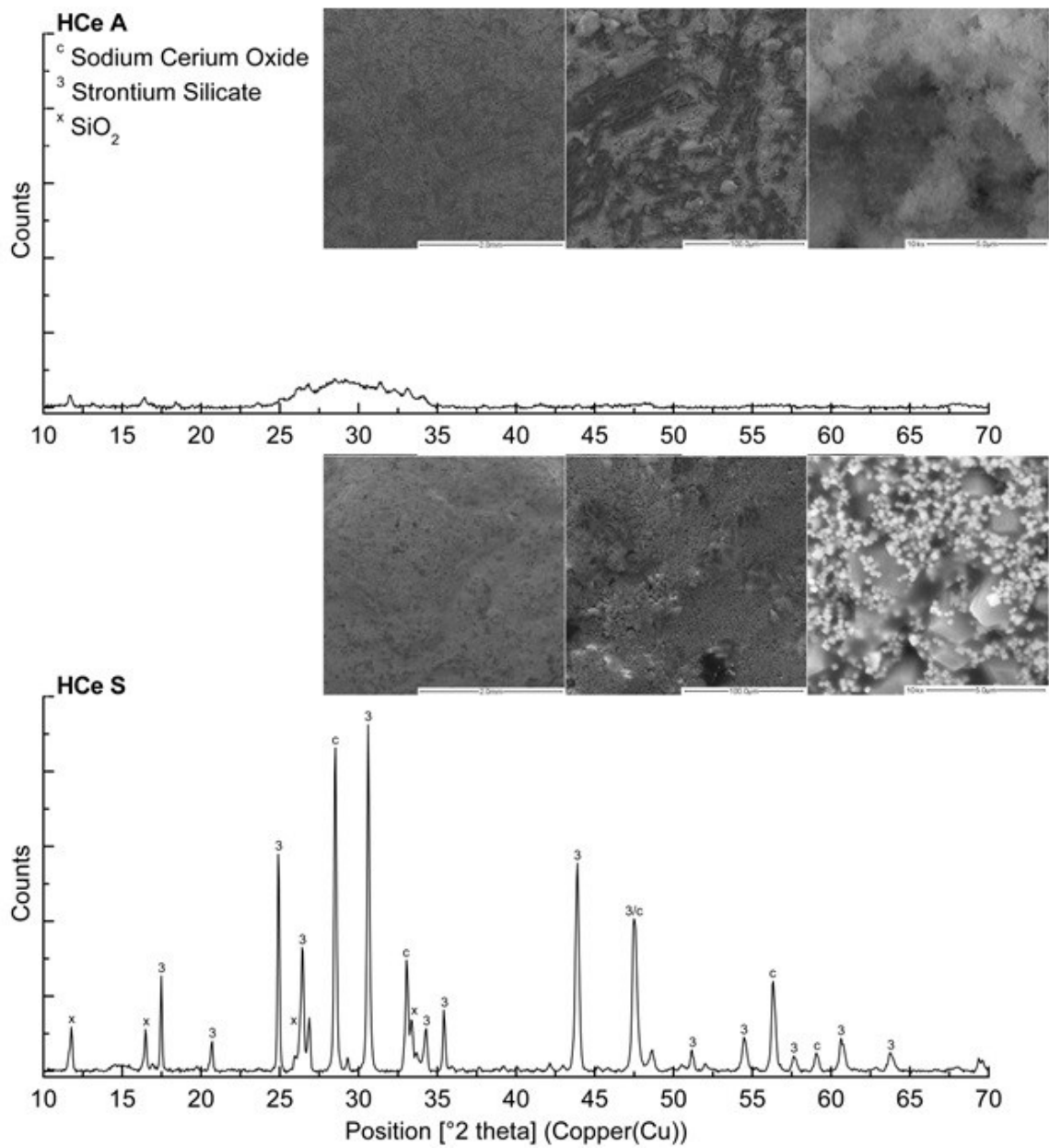


Figure 4-7. XRD patterns and SEM images at 30X, 500X and high magnification of thermally treated *HCe* disks.

Table 4-2. PDF and Molecular Formulas (MF) for XRD Identified Phases

<b>ID</b>	<b>Phase</b>	<b>PDF</b>	<b>MF</b>
<b>1</b>	<b>Sodium Strontium Silicate</b>	04-014-2585	Na <sub>6</sub> Sr <sub>3</sub> Si <sub>6</sub> O <sub>18</sub>
<b>2</b>	<b>Sodium Silicate</b>	00-023-0529	Na <sub>2</sub> Si <sub>2</sub> O <sub>5</sub>
<b>3</b>	<b>Strontium Silicate</b>	00-034-0099/00-030-1302	SrSiO <sub>3</sub>
		00-032-1257/04-016-6880	
		00-058-0576/04-012-0759	SrSi <sub>2</sub> O <sub>5</sub>
<b>C</b>	<b>Cerium Oxide</b>	04-008-6551	CeO <sub>1.66</sub>
	<b>Sodium Cerium Oxide</b>	04-015-0264	Na <sub>0.09</sub> Ce <sub>0.91</sub> O <sub>1.87</sub>
	<b>Sodium Cerium Silicate</b>	04-018-2280	Na <sub>8</sub> CeSi <sub>6</sub> O <sub>18</sub>
<b>X</b>	<b>Silicon Oxide</b>	01-075-3159/01-073-3418/01-075-3902	SiO <sub>2</sub>
<b>Y</b>	<b>Sodium Yttrium Silicate</b>	04-012-5275	Na <sub>3</sub> YSi <sub>3</sub> O <sub>9</sub>
		00-028-1190	NaYSiO <sub>4</sub>
		00-035-0014	Na <sub>3</sub> YSi <sub>2</sub> O <sub>7</sub>
		00-035-0406	Na <sub>9</sub> YSi <sub>6</sub> O <sub>18</sub>
	<b>Sodium Strontium Yttrium Silicate</b>	00-059-0766	Na <sub>4</sub> Sr <sub>2</sub> Y <sub>2</sub> Si <sub>4</sub> O <sub>15</sub>
<b>Z</b>	<b>Strontium Yttrium Silicate</b>	04-017-9226	SrY <sub>2</sub> Si <sub>3</sub> O <sub>10</sub>

#### 4.4.4. Ion-Release

Ion release of Si (presented in Figure 4-8) reaches a maximum of 1550 µg/mL for *Con-A* after 7 days incubation, decreasing to 580 µg/mL at 14 days. *Con-S* shows a similar trend where Si release reaches a maximum 950 µg/mL decreasing to 720 µg/mL. Regarding the Y and Ce containing disks, Si release ranged from 190 µg/mL to 320 µg/mL over the 14 day period without any significant difference in ion release that can be attributed to thermal treatment. Sr release shows trends opposite those of Si where a maximum release of 13 µg/mL and 24 µg/mL was reached for *Con-A/S* respectively. Y and Ce containing disks show a significant trend in increasing Sr release (shown in Figure 4-9) where *S*-disk release profiles show significantly higher release at each time period. Sr release for these samples ranges from 50 µg/mL from *HCe-A* after 1 day to a maximum of 1085 µg/mL from *HY-S* after 14 days. Na release is presented in Figure 4-10 as the difference in Na content in comparison with that of SBF-only samples incubated over the same time period. Similar to Si, Na release from *Con* disks is significantly greater than the other samples however, it does not experience a drop off after 14 days as experienced with Si. Na release for both *Con* sample types are comparable reaching a maximum of 4475 µg/mL after 14 days incubation. Both *HY-A/S* and *YCe-A/S* disks show an increase in Na release from 1 to 7 days reaching 630 µg/mL for *A*-disks and 409 µg/mL for *S*-disks. This is followed by a reduction below levels seen in SBF after 14 days. *HCe-A/S* disks also appear to reach a maximum release after 7 days

followed by a reduction, however the significance is unclear. Significant release of Y or Ce was not detected.

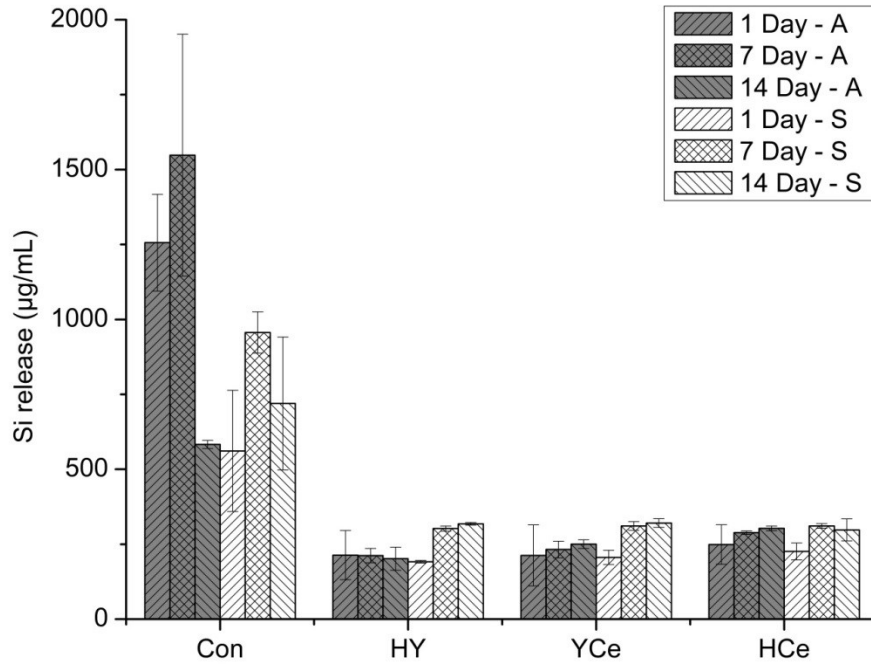


Figure 4-8. Si on release from each disk extracts over 1, 7, and 14 days.

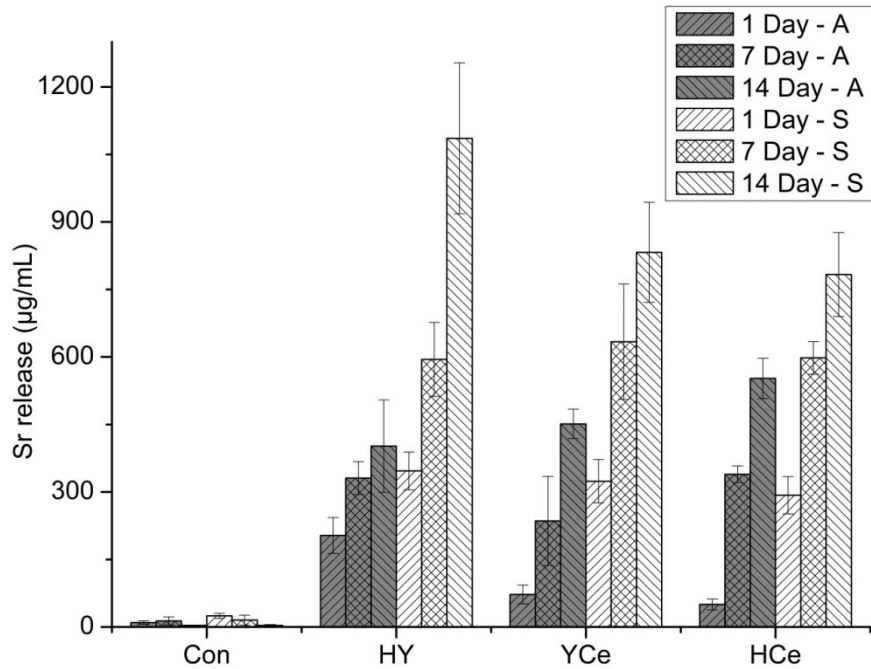


Figure 4-9. Sr ion release from each disk extracts over 1, 7, and 14 days.

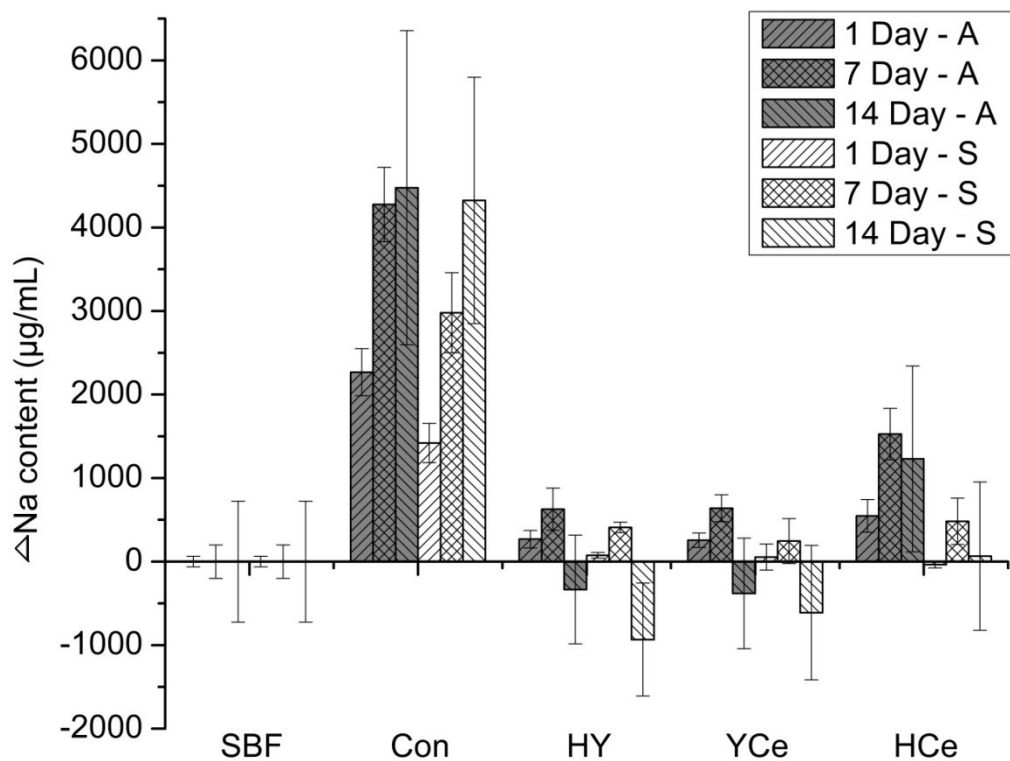


Figure 4-10. Change in Na<sup>+</sup> content relative to SBF-only samples after 1, 7, and 14 day disk incubation.

#### 4.4.5. Antioxidant Capacity

Antioxidant capacity is determined by comparing the quantity of the ABTS radical reduced by a known concentration of the antioxidant Trolox to that reduced by the sample, and is given in terms of mM Trolox Equivalency (mMTE). The antioxidant capacity of the ground disks is presented in Figure 4-11 where the *Con* disks, at 2.9-3.9 mMTE, and un-incubated samples performed better than 7 day incubated samples. *HCe-A* un-incubated reached 1.7 mMTE and the remaining samples fell within the range of 0.8-1.2 mMTE. Significant difference between  $t = 0$  and 7 day incubated samples was found for *Con-A*, *HY-S*, and both *HCe* disk types, where the  $t = 0$  samples showed higher antioxidant capacity. Another trend is observed through the significant differences between sample type at the same time period. *Con* 7 day, both *HY* time periods, and *HCe*  $t = 0$  samples show the *S*-samples perform significantly better than their *A* counterparts; the exception is *YCe*  $t = 0$  where the opposite is observed. The antioxidant capacity of the extracts collected after disk incubation in SBF is presented in Figure 4-12 and shows that

*Con* disk extracts have the greatest antioxidant capacity. *Con-A* extracts show an increase in antioxidant capacity up to 1.14 mMTE after 7 days and a decrease to 0.96 mMTE after 14 days. *Con-S* extracts increase over the 14 day period to 0.91 mMTE. The remaining samples fall in the 0.31 – 0.51 mMTE range without distinct trends between time periods. Significant differences in antioxidant capacity based on time for each extract are observed for each disk type with the exception of *YCe-A* and *HCe-S*. For *Con-A*, each time period is significantly different from the other two, while for *Con-S* the 1 day value is significantly different from the 7 and 14 day values, but the two are not significantly different from each other. The remaining glasses only show significance between the values at one adjacent time period, though the time periods and trend varies.

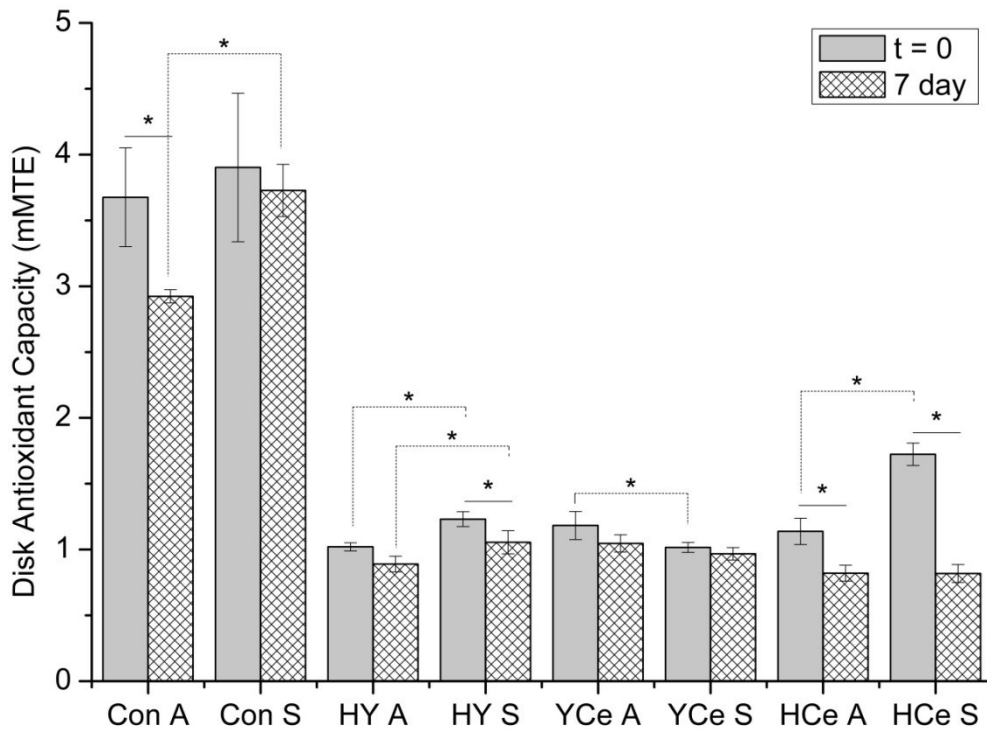


Figure 4-11. Antioxidant capacity of disk particulate after thermal treatment and 7 day incubation in SBF. \* indicates a significant difference ( $P < 0.05$ ) between time periods and sample type for each glass.

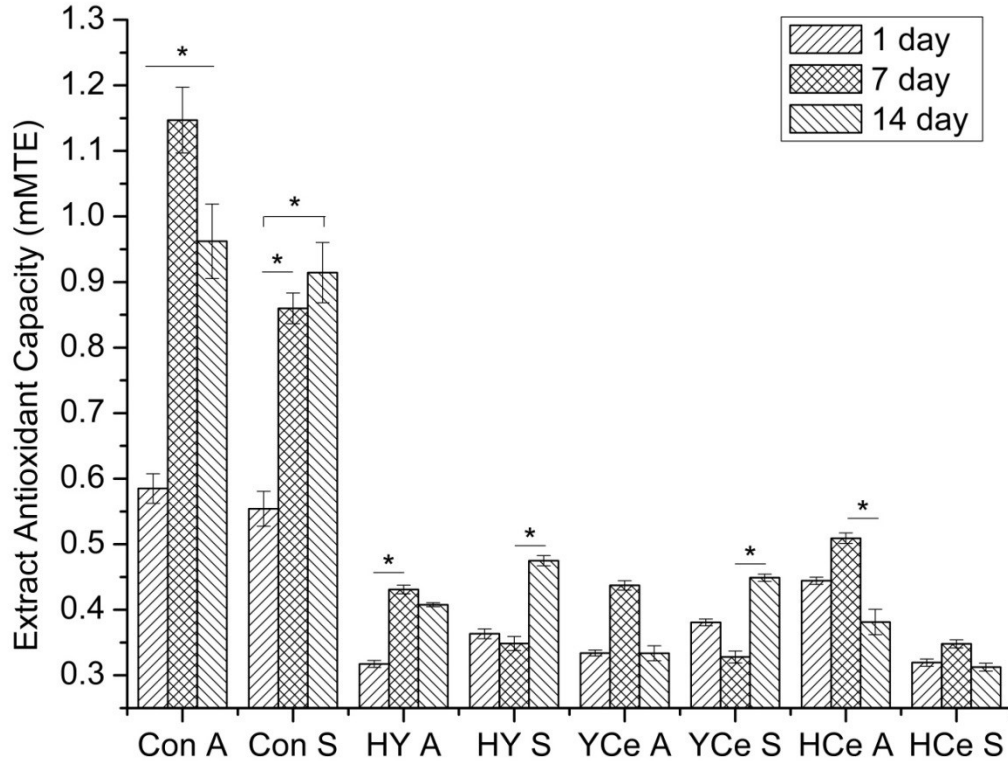


Figure 4-12. Antioxidant capacity of disk extracts relative to Trolox<sup>®</sup>. \* indicates a significant difference ( $P < 0.05$ ) between time periods for each sample.

#### 4.5 DISCUSSION

In an effort to reduce the dissolution of the original glass series thermal processing was utilized to crystallize pressed disks. Initial burnout of the polymer phase prior to reaching the lowest processing temperature is confirmed through thermal analysis where of the 10% addition all Y and Ce glasses reached 7-8% weight loss corresponding to the 81% observed in the PVA sample by 500°C. *Con* reached 11% weight loss which can be attributed to its small particle size and highly reactive nature,<sup>198</sup> where the additional 3% is due to loss of free water and -OH groups from the surface.<sup>119</sup> Following the burnout of the PVA and approaching the processing temperature, glasses are expected to follow similar sintering behavior to that which is seen in 45S5 Bioglass, beginning with the initial phase of densification just after the  $T_g$  is reached through viscous flow, onset of crystallization where viscosity increases preventing viscous flow, and secondary densification where increasing temperatures cause viscosity decrease and viscous flow to resume.<sup>122</sup> Using HSM,  $T_s$  corresponded to a 5% volume reduction. Shrinkage

calculations suggest each sample reached 1-7% of both thickness and diameter with minimal differences between disks processed at high (*S*) versus low (*A*) temperatures with the exception of *HCe-S*. The similarity in shrinkage may be a result of the heating rate. A study by Bretcanu et al. found the heating rate to correlate with the magnitude of shrinkage, where at a heating rate of 10°C/min 45S5 powder forms reached a maximum shrinkage of 6% at 900°C.<sup>122</sup> This suggests that the heating rate of 10°C/min selected for this work limited the shrinkage around 6%, and coupled with the holding temperatures selected, *A*-disks were likely held in the temperature range favoring viscous flow for the duration of their thermal treatment, while *S*-disks were heated through the region allowing viscous flow into the plateau where viscosity is too high as a result of crystallization and neither entered the second densification. The *HCe-S* samples are the exception to this where thickness expansion and diameter shrinkage relates to an overall expansion of the disk. One consideration for this is that the  $T_s$  is greater than the  $T_c$ , and may also approach the temperature required for second densification. Therefore, upon thermal treatment these samples pass through the viscous flow and crystallization regions to reach the sintering temperature and returned to the  $T_c$ . *HCe* HSM trace reveals a 10% volume increase initiating around 1100°C and peaking at nearly 1150°C. While the maximum processing temperature for these samples was 963°C, HSM was running at a rate of 2°C/min and the samples were treated at a rate 10°C/min. Bretcanu's study also shows the effect of heating rate on different characteristic temperatures where  $T_g$  and  $T_c$  increase with increasing heating rate and onset  $T_m$  decreases. It is possible that the onset of the expansion seen in the HSM trace occurred at a lower temperature during the thermal treatment as a result of the increased heating rate. In conjunction with a potential onset temperature decrease, the furnace may have slightly overshoot approaching the target temperature. The expansion seen in the HSM trace and *HCe-S* disks suggest the chemical expansion. This is not observed in the other HSM traces and can therefore be attributed to the presence of Ce, despite the presence of Ce in the *YCe* disks for which a study by Li et al. may also support an explanation.<sup>205</sup> The reduction of  $Ce^{4+}$  to  $Ce^{3+}$  at higher temperatures (~1000°C) is associated with structural expansion of the ceria unit cell by 17% and creation of oxygen vacancies for charge compensation.<sup>206</sup> This combination likely produces the expansion seen in the *HCe-S* samples though inherent

differences in the molar volume between the glassy and crystalline phases may contribute as well.<sup>205</sup> This does not appear in the *YCe* HSM traces as Y has been shown to reduce the reduction of  $Ce^{4+}$  to  $Ce^{3+}$  as well as stabilize the transition.<sup>205</sup> Presence of Ce crystallites in the *HCe-S* glass-ceramic are observed under SEM at high magnification and confirmed by the identification of a sodium-cerium-oxide phase (suggesting Na was charge compensating in the glassy network) in the corresponding XRD patterns, both of which are only observed in the *HCe-S* disk; lending further support to the Ce reduction mediated expansion characteristic of the *HCe-S* disks. In addition, XRD patterns of *Con* samples show a primary sodium-strontium-silicate and secondary strontium-silicate phase, which can be compared to the sodium-calcium-silicate and calcium-silicate phases commonly generated during typical bioactive glass sintering<sup>119,122,124</sup>. This suggests that despite the crystallinity, dissolution and HCA layer formation may still occur, as seen in SBF studies with these analogous phases. SEM images support that *Con* is still significantly reactive based on surface morphology where *Con-A/S* disks have a reacted surface layer. While similar phases are prominent in each Y and Ce containing disk they have a surface of packed and sintered powder and varying degrees of Na rich surface crystallite growth. This suggests reduced reactivity in comparison with *Con* and which may be confirmed through analysis of ion release.

Ion release studies reveal *Con-A/S* disks are reactive in SBF and release significantly higher levels of Si and Na and lower levels of Sr than the Y and Ce containing disks. Si release approaching 1550  $\mu\text{g/mL}$  exceeds typical levels released by bioactive glasses where a solubility limit is reached at 120  $\mu\text{g/mL}$  up to a pH of 9; this is suggestive that the pH of the extracts are slightly higher where the solubility limit begins to increase exponentially.<sup>108,109</sup> The maximum value of Si release from the *Con* disks is 10x lower than that observed from the original glass powders, though a similar drop-off in concentration is observed after 7 days incubation. This suggests the Si release reaches the solubility limit after 7 days and proceeds to precipitate over the duration of the 14 day time period, though at a lower pH and corresponding concentration than that of the original glass powders.<sup>177</sup> Na is typically found in physiological fluids at concentrations ranging from 2,500-3,500  $\mu\text{g/mL}$ <sup>110,181</sup>; the original glass and *Con-A/S* disks release exceeds these levels with only a minor decrease associated with the thermal treatment,

though the rate of release was slowed reaching a maximum release at 14 days in comparison to after the first day.<sup>198</sup> Sr, which was released in excess at 100  $\mu\text{g/mL}$  from the original glasses decreased to 13-24  $\mu\text{g/mL}$  from the *Con-A/S* disks bringing it into the range found to support healthy bone mineralization.<sup>113,182</sup> Ion release levels for *Con* disks are still high but reduction of both Si and Sr release by a factor of 10 upon thermal treatment will likely reduce the associated toxicity to levels seen for the original Y and Ce containing glasses with similar release.<sup>198</sup> Si release from *HCe* disks decreased by a factor of 2 from the original glasses and showed only minimal decreases by *HY* and *YCe* disks. These levels were found to pose minimal toxicity to fibroblasts and osteoblasts through glass extract cell viability assays.<sup>198,199</sup> With the exception of *HCe-A*, Na released by the Y and Ce containing disks increases over the initial 7 days of incubation to a maximum of 630  $\mu\text{g/mL}$  which is well within physiological levels. Subsequently, precipitation in excess of the Na that was released, (drawing from the concentration in SBF) occurs in the following 7 days. Na release from *HCe-A* is the exception where release remains within physiological levels peaking at 1525  $\mu\text{g/mL}$  after 7 days of incubation. Sr release for the original glasses fell within the optimum range from 10.6 to 0.9  $\mu\text{g/mL}$ , however is released in dramatically higher levels from the Y and Ce containing disks. While Sr levels are excessive, any excess is excreted through the kidneys in the same manner as Ca, thereby reducing the potential for toxic effects.<sup>74,113</sup> In addition, disks treated at higher temperatures exceed the Sr concentrations of those treated at lower temperatures. This is indicative of effects relating to devitrification with thermal treatment. The crystalline phases generated in *Con* are analogous to those observed in the standard 45S5 glass, however with the addition of Y and Ce, the stoichiometric ratios will change as the crystalline phases are generated. For those samples containing Y and Ce, their incorporation into the sodium-strontium-silicate phase and the other phase variations may occur at the expense of Sr (considering ionic charge and size similarities), in which case the residual glass phase would be a Sr rich silicate.<sup>207,208</sup> The principle of bioactive glasses rests on their dissolution, and it is well known that crystalline phases are resistant to dissolution in comparison with their amorphous counterparts.<sup>209</sup> Therefore, a residual glassy phase rich in Sr after devitrification may account for the excess Sr released from the Y and Ce containing

samples in comparison with that observed from the parent glass. Further work is required to clarify the structural role of Sr in the network and describe the significantly increased propensity for dissolution from the glass-ceramic network. Y and Ce are retained in the glass-ceramics as seen with the original glasses and in agreement with the literature.<sup>116,202,210</sup>

Y and Ce were incorporated in the glass composition with the aim of developing structures within the glass network similar to those present in yttria and ceria nanoparticles shown to provide cell protection from oxidative stress. It is clear in both the ground disks and extracts from incubation in SBF *Con* samples show the greatest propensity for ROS scavenging. In addition, the antioxidant capacity associated with ground disks is double that of the extracts, and of the ground disks, *Con* disks have double the capacity of Y and Ce containing disks. Therefore, in these glass-ceramics Y and Ce can be considered inhibitors of ROS scavenging. Since Y and Ce are known to increase the rigidity of the glass network which leads to reduced solubility it may follow that the antioxidant capacity is related to the reactivity of both the surface and dissolution products.<sup>116,158,163,202,210</sup> The lack of Y or Ce in the extracts further eliminates them as a source for the ROS scavenging ability of these glass-ceramics. Therefore, it is likely due to the silanol surface and silicic acid species in the extracts.<sup>194-196</sup> The negatively charged surface or extract species may account for the neutralization of the ABTS radical cation through hydrogen bonding.<sup>180,196,197</sup> While the study by Preari et al. addressed silicic acid species in relation to hydrogen bonding, studies by Howard et al.<sup>211</sup> and multiple works by Spange et al.<sup>212-214</sup> further support the hydrogen bond donating (HBD) ability of surface and silica gel silanol groups. These studies found that, in comparison with unprocessed silica surfaces, those chemically modified to reduce the quantity of surface silanols, showed reduced polymer adsorption attributed to the reduced polarization parameter  $\alpha$  which is directly related to HBD ability. Therefore, the reduction of ABTS is likely attributable to the HBD ability of silanols on both the reacted particulate surfaces and of silicic acid species in the extracts.<sup>212-214</sup> Additional, work relating the surface conditions and silicate species in the extracts is will give insight into the proposed mechanisms.

#### 4.6 CONCLUSION

The thermal treatment of Y and Ce glasses were shown to produce glass-ceramics with varying degrees of crystallinity and associated shrinkage with the exception of the *HCe-S* samples which exhibits an expansion due to  $Ce^{4+}$  reduction. The resulting phases reduce Si and Sr release from *Con-A/S* samples while Na release remained consistent. Y and Ce containing disks shows a significant increase in release of Sr after thermal treatment, exceeding levels found to promote bone mineralization. Antioxidant capacity remained at mMTE for treated *Con* disks and fell to  $< 1$  mMTE for the Y and Ce glass-ceramics. Therefore, the formation of glass-ceramics partially reduces solubility, while maintaining antioxidant capacity. While solubility is maintained it is necessary to evaluate the potential for bioactivity.

Therefore, in the final chapter, deposition of a HCA layer, MC3T3 Osteoblast and sNF96.2 Schwann cell attachment of SBF incubated samples is evaluated through optical microscopy and SEM.

## CHAPTER 5 - BIOACTIVITY OF $Y_2O_3$ AND $CeO_2$ DOPED $SiO_2$ - $SrO$ - $Na_2O$ GLASS-CERAMICS.<sup>4</sup>

### 5.1 ABSTRACT

The bioactivity of Yttrium (Y) and Cerium (Ce) are investigated when substituted for Sodium (Na) in a  $0.52SiO_2-0.24SrO-0.24-xNa_2O-xMO$  glass-ceramics (where  $x = 0.08$  and  $MO = Y_2O_3$  or  $CeO_2$ ). Bioactivity is monitored through pH and Inductively Coupled Plasma-Optical Emission Spectrometry (ICP-OES) where pH of simulated body fluid (SBF) ranged from 7.5-7.6 and increased between 8.2 and 10.0 after 14 day incubation with the glass-ceramic disks. Calcium (Ca) and Phosphorous (P) levels in SBF after incubation with Y and Ce containing disks show a continual decline over the 14 day period. In contrast, *Con* disks (not containing Y or Ce) caused the elimination of Ca in solution after 1 day and throughout the incubation period, and initially showed a decline in P levels followed by an increase at 14 days. Scanning Electron Microscopy (SEM) and Energy Dispersive Spectrometry (EDS) confirmed the presence of Ca and P on the surface of the SBF incubated disks and showed precipitates on *Con* and *HCe* (8 mol% Ce) samples. Cell viability of MC3T3 Osteoblasts was not significantly affected at a 9% extract concentration. Optical microscopy after 24 hr cell incubation with disks showed *Con* samples do not support Osteoblast or Schwann cell growth, while all Y and Ce containing disks have direct contact with Osteoblasts spread across the wells. Schwann cells attached in all wells, but only showed spreading with the *HY-S* (8 mol% Y, heated to sintering temperature) and *YCe* (4 mol% Y and Ce) disks. SEM of the compatible disks shows Osteoblast and sNF96.2 Schwann cells attachment and spreading directly on the disk surfaces.

---

<sup>4</sup> Under review; Co-authors: Timothy J. Keenan, Anthony W. Wren.

## 5.2 INTRODUCTION

Bioactive glasses are defined by their ability to become securely bonded with host tissues *in vivo*. This characteristic arises from a reaction cascade beginning with the exchange of hydrogen ions ( $H^+$  or  $H_3O^+$ ) from physiological fluids with  $R^+$  and  $R^{2+}$  (commonly  $Na^+$  and  $Ca^{2+}$ ) modifying ions in the glass network. Subsequently, dissolution of the Si-O glass network creates a surface consisting of silanol (Si-OH) groups which proceeds to condensate to Si-O-Si and facilitates the deposition of an amorphous hydroxycarbonated apatite (HCA) layer.<sup>84,90,127</sup> The formation of the HCA layer on the biomaterial surface is essential for bonding with host tissues. As such, bioactivity is evaluated based on the formation of a HCA surface layer after incubation in physiological fluids, commonly simulated body fluid (SBF). SBF replicates the pH and ion content of blood plasma, of particular interest is the change in Ca and P content of SBF with initial concentrations at 2.5 mM and 1.0 mM, respectively.<sup>110</sup> The fluctuation of these ions in solution can be indicative of dissolution from the glass network, if the glass contains either element, or precipitation, potentially for the formation of an HCA layer. Aside from Ca and P, other dissolution products from silicate based bioactive glasses have been found to encourage the bonding of bioactive glasses with host tissues. These ions commonly activate or upregulate the cellular response to the HCA layer, and encourage osteogenesis; one example is Si, which is essential for metabolic processes relating to formation and calcification of the bone matrix and can improve bone mineral density.<sup>101,173</sup> Of particular interest in this work is Sr which has been shown to perform similarly to Calcium (Ca) in both the glass network and the body.<sup>74,101,113,114</sup> As such, it makes Sr an ideal candidate to replace the Ca component of typical bioactive glass compositions. One drawback to the replacement of Ca with Sr is the reduction of glass network solubility and changes in the formation and morphology of the HCA layer resulting in reduced bioactivity.<sup>93,94,142</sup> The replacement of Ca is considered due to the excessive Ca accumulation at the site of nerve injury and the dissolution behavior of bioactive glasses. Aside from the physical damage associated with nerve injury, loss of ionic homeostasis in the extracellular fluid occurs due to the influx of calcium and loss of Na. This Ca accumulation alone can cause excitotoxic necrosis in adjacent cells and tissue and limit the regeneration potential of nerve tissue, which already has limited

ability to reconnect over gaps of 5 mm, but also stimulates the production of radical oxygen species (ROS).<sup>21,34-37,68,86,146</sup> The presence of ROS and accompanied oxidative stress on neighboring cells and tissue, in addition to the impediments created by the inherent biological response further reduce the chance at successful regeneration and reconnection for functional recovery.<sup>33,86,144,149,174,175</sup>

Current techniques employed to aid in the regeneration and reconnection of nerves focus on Methylprednisolone Sodium Succinate (MPSS) to reduce the inflammatory response, or nerve guide conduits.<sup>146,175</sup> Conduits provide physical stabilization and axonal guidance, as well as having the capability to deliver and maintain growth factors at the site of regenerating axons.<sup>18</sup> Recently, bioactive glass fiber wraps have been considered for use as nerve conduits and have shown the potential to encourage neurite outgrowth, which can be extended to particulates in composite grafts with polymers, for improved flexibility and degradability.<sup>68,86,149,155,215</sup> Improvements on bioactive glasses for nerve conduit applications has been suggested through the removal of traditional ions such as Ca while maintaining Na to supplement the ionic fluctuations seen after injury. Additionally, for the purpose of encouraging functional recovery of nerves, the oxidative stress may also be addressed. Elimination of ROS is proposed through the addition of Y and Ce as dopants, where studies have found that 12 nm yttria and ceria nanoparticles (non-toxic up to 200  $\mu\text{g/mL}$ ) offered neuroprotection *via* direct dose dependent ROS scavenging.<sup>37,148</sup> Therefore, upon inclusion in the glass composition one or both elements may create a local coordination environment in the glass network that will allow it to act as an antioxidant. One consideration with the introduction of trivalent and tetravalent ions into the glass network is the effect on bioactivity. Studies by Leonelli et al. and Cacaina et al. revealed that Y and Ce have been successfully incorporated into bioactive glasses, however, bioactivity decreased with increasing Y and Ce content. The deposition of a HCA layer was delayed in these glasses forming after 7-14 days incubation in simulated body fluid (SBF).<sup>115,116</sup>

Previous work evaluating the effect of  $\text{Y}_2\text{O}_3$  and  $\text{CeO}_2$  on  $\text{SiO}_2\text{-SrO-Na}_2\text{O}$  glass structure and solubility found Y and Ce to perform as modifier ions within the glass network, though they produce an increase in rigidity and decrease the solubility due to ionic differences with Na for which they are being substituted.<sup>198,216</sup> Despite the reduced

solubility, the dissolution products still posed toxicity in osteoblast viability studies, so glasses were thermally treated to produce partially crystalline glass-ceramics and further reduce the solubility.<sup>199</sup> While partial crystallization reduces the solubility it has also been shown, through numerous studies, to reduce the bioactivity of bioactive glasses.<sup>119,124,126</sup> This work uses pH, Inductively Coupled Plasma-Optical Emission Spectroscopy (ICP-OES), Scanning Electron Microscopy (SEM), and Electron Dispersive Spectroscopy (EDS) to evaluate the bioactivity in terms of Ca and P presence on the surface of Y and Ce containing glass-ceramics heat treated at a high and low temperature, namely the first crystallization temperature ( $T_{c1}$ ) or 50°C above the glass transition ( $T_g$ ).

## 5.3 EXPERIMENTAL

### 5.3.1. Disk Synthesis

Four glasses of varying composition were formulated for this study, one containing yttrium (Y), *HY*, one with cerium (Ce), *HCe*, one glass containing both Y and Ce, *YCe*, and one SrO-Na<sub>2</sub>O-SiO<sub>2</sub> control glass, *Con*. The Y<sub>2</sub>O<sub>3</sub> and CeO<sub>2</sub> is incorporated into each glass, with the exception of the control, at the expense of Na<sub>2</sub>O. Glass compositions (mol%) can be found in Table 5-1.

Glass powders were prepared by weighing out appropriate amounts of analytical grade reagents (Fisher Scientific, PA, USA) and ball milling (1 h). The mix was then oven dried (100°C, 1 h), fired (1500°C, 1 h) in a platinum crucible and shock quenched in water. The resulting frit was dried, ground and sieved to retrieve glass particles <20µm. Glass powders were ball milled for 24 hrs with <75 µm polyvinyl alcohol (PVA) added at 10 wt% to act as a binder.

Glass powders (0.15 g/disk,  $n = 3$ ) were pressed at in a stainless steel die at a pressure of 4 tons and subsequently heat treated at two processing temperatures ( $T_{p1}$  and  $T_{p2}$ ), where the processing temperatures are included in Table 5-1. Disks were heated to  $T_{p1}$  at a rate of 10°C/min and held for 6 hrs, then heated at a rate of 1°C/min to  $T_{p2}$ , followed by an additional 6 hr hold and cool down at 5°C/min. Processing temperatures were selected at the glass transition ( $T_g$ ), 50°C above  $T_g$  ( $T_{g+50}$ ), or sintering ( $T_s$ ) and 1<sup>st</sup>

crystallization temperatures ( $T_{c1}$ ) for each glass individually, and are denoted by annealed disks (A) and sintered disks (S).

Table 5-1. Glass Compositions in mol% and Characteristic Temperatures ( $^{\circ}\text{C}$ )

		<u>Con</u>	<u>HY</u>	<u>YCe</u>	<u>HCe</u>
	<b>SiO<sub>2</sub></b>	52	52	52	52
	<b>SrO</b>	24	24	24	24
	<b>Na<sub>2</sub>O</b>	24	16	16	16
	<b>Y<sub>2</sub>O<sub>3</sub></b>	-	8	4	-
	<b>CeO<sub>2</sub></b>	-	-	4	8
<b>A</b>	<b>T<sub>g</sub></b>	497	661	625	566
	<b>T<sub>g+50</sub></b>	547	711	675	616
<b>S</b>	<b>T<sub>s</sub></b>	607	809	709	963
	<b>T<sub>c1</sub></b>	777	783	793	738

### 5.3.2. pH Analysis

Sterile liquid extracts were prepared by incubating glass-ceramic disks ( $n = 3/\text{time period}$ ) in sterile 15 mL centrifuge tubes with 5 mL simulated body fluid (SBF) prepared as described by Kokubo et al.<sup>110</sup> The tubes, including disk-free control samples, were sealed and incubated for 1, 7, and 14 days. Upon removal, each sample was filtered (Amicon Ultra-4 Centrifugal Filters, Fisher Scientific, PA, USA) to ensure particle free extracts. A 1.5 mL aliquot from each sample extract was removed into a sterile vial to be used for cytocompatibility studies.

The pH of each sample extract was measured using an Accumet® Excel XL 15 pH meter (Fisher Scientific, PA, USA). Prior to testing, the pH meter was calibrated using pH buffer standards  $4.00 \pm 0.02$ ,  $7.00 \pm 0.02$  and  $10.00 \pm 0.02$ . The probe was rinsed with DI water and allowed to stabilize in the pH 7 buffer between readings which were taken after the pH value stabilized for 10 s.

### 5.3.3. Inductively Coupled Plasma-Optical Emission Spectroscopy (ICP-OES)

The Ca and P ion content was measured axially using Inductively Coupled Plasma-Optical Emission Spectroscopy (ICP – OES) on a Perkin-Elmer Optima 8000 (Perkin Elmer, MA, USA) with a detection limit of  $0.1 \mu\text{g/mL}$ . ICP – OES calibration standards for Ca and P were prepared from stock solutions (Perkin-Elmer, MA and Fisher

Scientific, PA, USA) at 0.1, 1, 10  $\mu\text{g/mL}$  for samples diluted 1:10 after Ca and P concentrations in the SBF-only samples were found to be  $93.4\pm 1.5 \mu\text{g/mL}$  and  $38.0\pm 0.7 \mu\text{g/mL}$ , respectively. Ca and P precipitation from SBF solution after incubation with disks is reported based on the percent remaining in solution relative to that of the SBF-only controls using equation 5-1:

$$\% \text{ Ca or P remaining in SBF soln.} = \frac{[X]}{[\text{SBF}]} * 100 \quad (5.1)$$

where [X] is the ion concentration of the sample solution, and [SBF] is the ion concentration of the SBF-only samples.

#### 5.3.4. Osteoblast Viability

MC-3T3-E1 Osteoblasts (ATCC CRL-2593) were maintained on a regular feeding regime with Minimum Essential Medium (MEM) Alpha Media (w/L-glutamine, ribonucleosides, and deoxyribonucleosides), supplemented with 10% fetal bovine serum (FBS) in a cell culture incubator at  $37^{\circ}\text{C}/5\%\text{CO}_2/95\%\text{air}$  atmosphere (Fisher Scientific, PA, USA). Viability studies were conducted using cells seeded into 96-well plates at a density of  $10^4$  cells/well where after 24 hr incubation cells were confluent across the well surface. Confluency was not achieved with Schwann cells and therefore not used for viability studies. Glass/ceramic extracts and SBF controls, were added to the 100  $\mu\text{L}$  wells, 10  $\mu\text{L}$ /well, producing a final concentration by volume of 9%. After addition of the extracts the plates were incubated for an additional 24 hrs.

Cytocompatibility was tested using the methyl thiazolyl tetrazolium (MTT) assay. 10  $\mu\text{L}$  of MTT reagent was added to each well and incubated for 4 hrs ( $37^{\circ}\text{C}/5\%\text{CO}_2$ ). After incubation each well was aspirated and 100  $\mu\text{L}$  of MTT solubilization solution (10% Triton X-100 in acidic (0.1M HCl) Isopropanol) was added, and mixed by gently pipetting at half the well volume (50  $\mu\text{L}$ ). Once the crystals were fully dissolved, the absorbance was measured at 570 nm using a  $\mu\text{Quant}$  Microplate Spectrophotometer (Bio-tek Instruments Inc., VT, USA). Media wells with the SBF control samples were used to determine the background effect and a control cell population was assumed to represent 100% viability to normalize the readings. One-way analysis of variance (ANOVA) was

employed to compare the difference in cell viability relative to the control population and between time periods for each sample. Comparison of relevant means was performed using the post hoc Bonferroni test. Differences between groups was deemed significant when  $P < 0.05$ .

### **5.3.5. Bioactivity**

After SBF incubation, disks were removed, rinsed gently with DI water and stored in a desiccator. Any HCA deposition on the disk surface ( $n = 1$ ) was observed with a Quanta 200F Environmental Scanning Electron Microscope under a vacuum at a pressure of 0.60 torr. The electron beam was used at an accelerating voltage of 20 kV and a spot size of 3.0. Energy dispersive x-ray spectroscopy was carried out using an FEI EDAX system equipped with a silicon-drift detector.

### **5.3.6. Cell Adhesion**

MC-3T3-E1 Osteoblasts (ATCC CRL-2593) were maintained as described in section 2.4. sNF96.2 Schwann (ATCC CRL-2884) cells were maintained on a regular feeding regime with DMEM Low Media supplemented with 10% FBS in a cell culture incubator at 37°C/5%CO<sub>2</sub>/95%air atmosphere. Adhesion studies were conducted after allowing the glass-ceramic disks ( $n = 1$ ) to buffer for 24 hrs in Media with 3 exchanges. Osteoblast and Schwann cells were seeded onto individual disks in 24-well plates at a density of 10<sup>5</sup> cells/well and incubated for 24 hrs. Optical images of each disk/well were taken at 4x magnification. Osteoblasts were subsequently fixed using the procedure from Wang et al.<sup>155</sup> An additional milliliter of DMEM low media was added to each well for the schwann cell samples which were then incubated for an additional 72 hrs and fixed. SEM images were collected using the parameters given in section 5.3.5.

## **5.4 RESULTS**

### **5.4.1. pH Analysis**

pH (presented in Figure 5-1) of the SBF was found to be 7.5 increasing to 7.6 after 14 days. All disks produced an initial increase in pH after 1 day incubation and continued increase over the 14 day time period. *HCe-A* and *HCe-S* disks produced an initial pH increase of 8.2 and 7.8 increasing to 8.7 and 8.2 after 14 days. The *HY* and *YCe*

disk extracts fell within the *HCe-A/S* pH range, while for *Con* extracts pH was found to range from 9.0 to 10.0, with *Con-A* at a higher pH than *Con-S* at each time period.

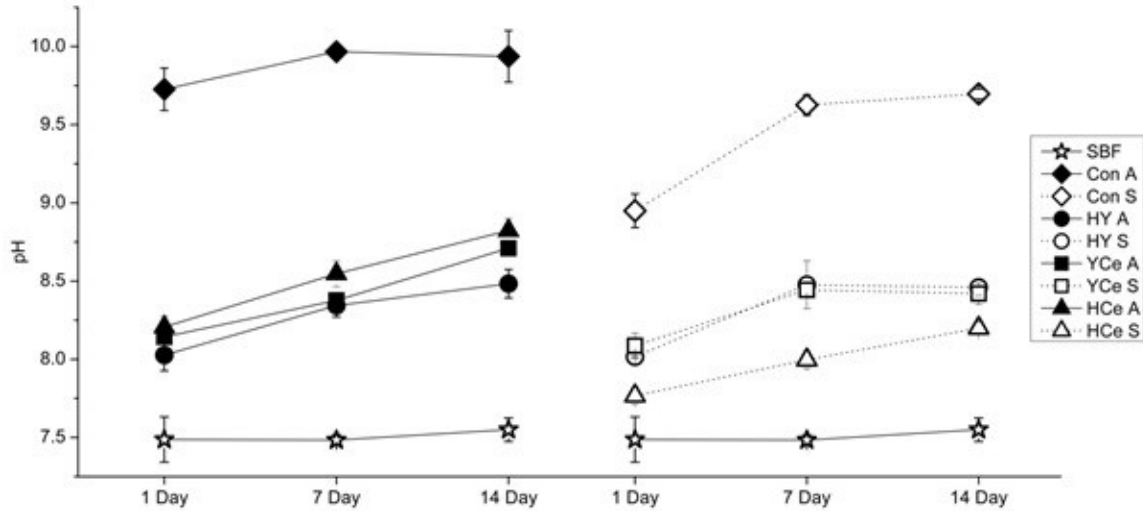


Figure 5-1. pH of liquid extracts from Y/Ce disk series over 1, 7 and 14 days incubation.

#### 5.4.2. Inductively Coupled Plasma-Optical Emission Spectroscopy (ICP-OES)

The percent of Ca and P content remaining in solution after disk incubation in SBF is shown in Figure 5-2 and Figure 5-3, respectively. It can be seen that over the 14 day incubation, the Ca in solution decreases for the Y and Ce containing disks, with the exception of *HY-S* which reaches a plateau after 7 days. An initial drop of 27%, 24% and 2% after 1 day occurs for *HY-S*, *YCe-S* and *HCe-S*, further decreasing to 49%, 51% and 27% after 14 days, respectively. The *A*-disks produce a greater Ca reduction in comparison with the *S*-disks, of 29%, 36% and 38% after 1 day to 92%, 64% and 100% after 14 days for *HY-A*, *YCe-A* and *HCe-A*, respectively. *Con* disks cause 100% decrease of Ca in solution after 1 day, however with P, causes a 75% and 66% decrease after one day, with a further decrease at 7 days, and a subsequent increase to 52% and 56% for *Con-A* and *Con-S* at 14 days. The Y and Ce containing disks do not follow this behavior but show continued decrease of P in solution over the 14 day incubation. Similar to Ca, *HCe-S* causes minimal change in P concentration at 1 day while the remaining samples

cause decrease between 22% and 69%. After 14 days a 73% to 94% decrease in P content is seen for all Y and Ce containing disks.

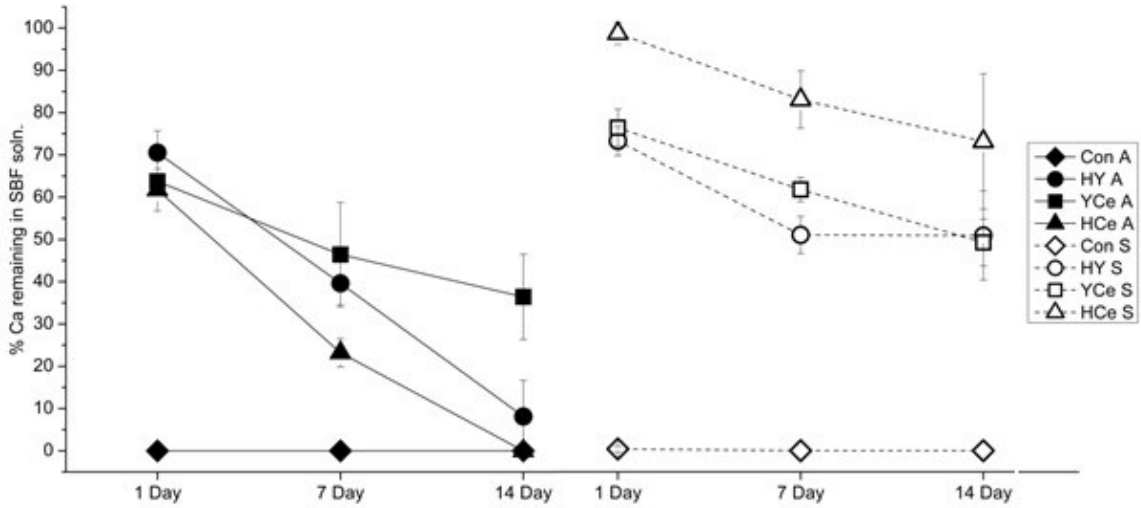


Figure 5-2. % Ca ions remaining in solution after 1, 7, and 14 day disk incubation relative to SBF-only samples.

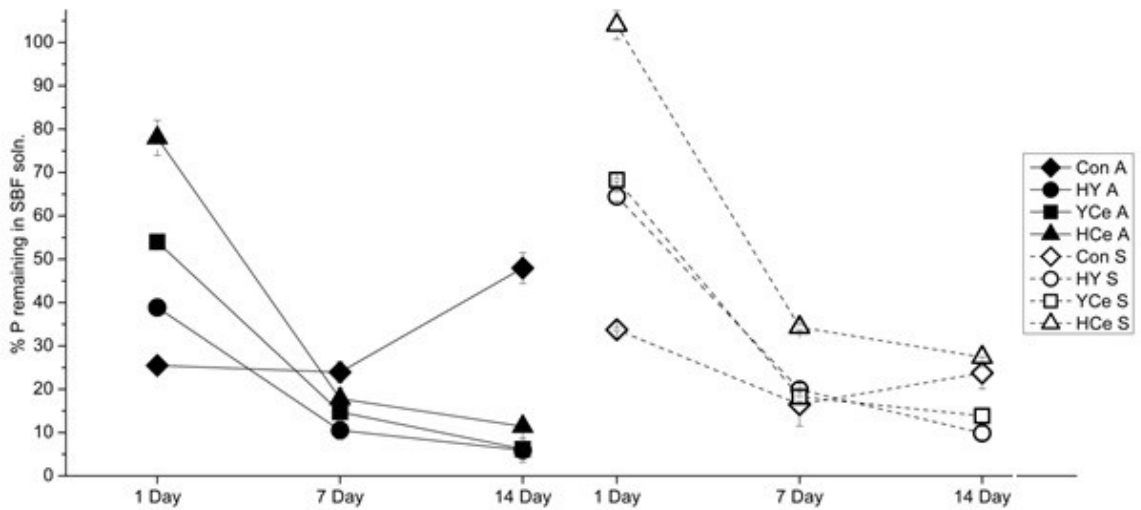


Figure 5-3. % P ions remaining in solution after 1, 7, and 14 day disk incubation relative to SBF-only samples.

### 5.4.3. Osteoblast Viability

Osteoblast cell viability was tested using liquid extract concentrations of 9% and the results are presented in Figure 5-4. This shows that viability does not differ significantly from the control population for any sample at any time. While statistical analysis did not find a significant increase associated with the *HY-A* 7 day (131%) or *HCe-A* 1 (126%) and 7 day (131%) samples, these samples showed viability higher than that of the control population.

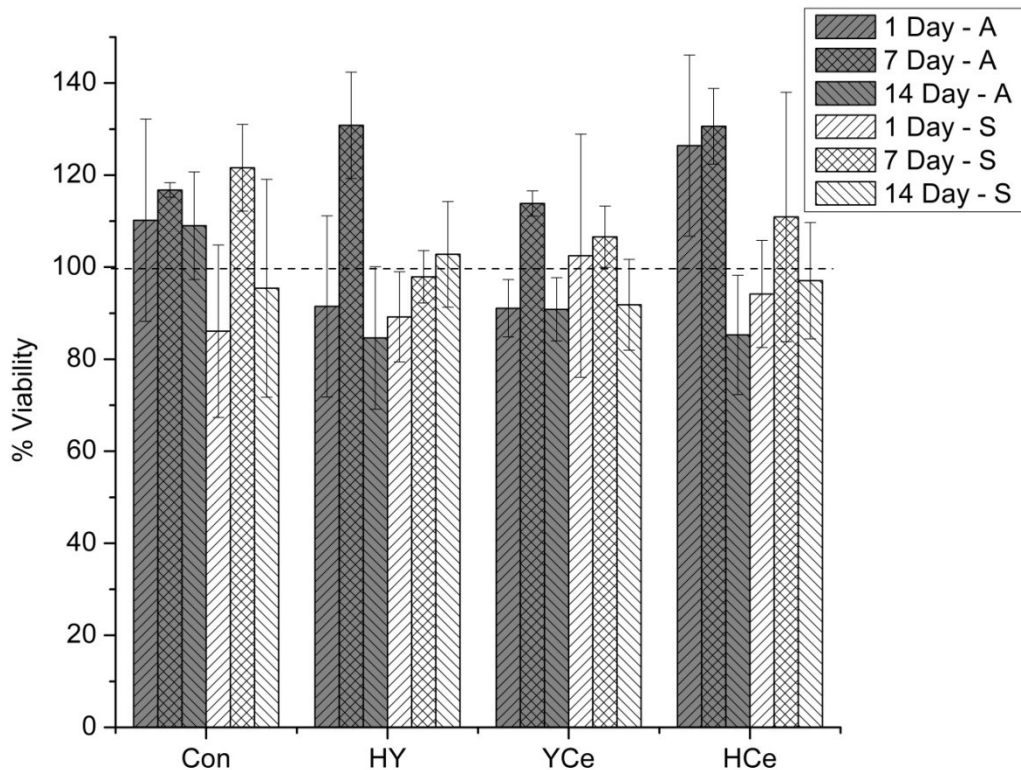


Figure 5-4. Osteoblast viability after incubation with disk extracts at 9%, 20% and 33% concentrations by volume over 1, 7 and 14 days. \* indicates a significant difference ( $P < 0.05$ ) between time periods for each sample.

### 5.4.4. Bioactivity

SEM images of the surface of each disk before ( $t = 0$ ) and after 1 and 14 day incubation in SBF are presented in Figures 5-5 through 5-8. Additionally, the EDS generated oxides are included for each disk. The  $t = 0$  *Con* disks both exhibit what appears to be a partially reacted surface and correspondingly a high concentration of

Na<sub>2</sub>O relative to SiO<sub>2</sub>. After incubation the ratio becomes comparable to the initial glass composition and the presence of quantities of CaO and P<sub>2</sub>O<sub>5</sub> are detected on the surface. Among *Con* samples, the *Con-A* 14 day sample was the only to detect SrO at the surface of the disk. The *HY* disks initially and after 14 day incubation each show a packed and sintered powder surface with SiO<sub>2</sub>, SrO, and Na<sub>2</sub>O content comparable to the original glass composition. EDS also detected small quantities of Ca on the surface of the *HY* disks, though no precipitates are observable. The *YCe* disk surfaces appear as a compacted/sintered powder surface without visible precipitates over the 14 day time period similar to those of the *HY* disks. EDS shows surface composition is comparable to that of the original glass, though for *YCe-A*, Na rich crystals present at t = 0 skews the ratio between Na<sub>2</sub>O and SiO<sub>2</sub>, and presence of Ca and P. *HCe-A*, t = 0 also shows significant presence of Na rich surface crystals which are reflected in the oxide ratios. After 1 and 14 day incubation precipitates form on the surface with Ca identified after 1 day and quantities of both Ca and P after 14 days. Similar trends are seen with the *HCe-S* disks though there is a localization of Ce at the surface, opposite that observed with *HCe-A* disks. In addition to increasing Ca and P precipitates, after 14 days cracks appear on the surface similar to those appearing on the *Con-A* disks over the same incubation period.

#### 5.4.5. Cell Adhesion

The optical images of the disk-cell interface after 24 hr incubation are shown in Figures 5-9 and 5-10. It can be seen that the 14 day incubated *Con* disks continue reacting when in contact with cell media causing it to gel and creating an inhospitable environment for cell attachment and survival. Y and Ce containing disks, while they may continue to react in cell media, allow the media to maintain its viscosity and clarity, and supports Osteoblast attachment and spreading with many cells directly contacting the disks. Schwann cells show reduced viability when incubated with the Y and Ce containing disks in comparison with the osteoblasts, though it can be seen that cell attachment has occurred. Despite the cell attachment, the majority of the cells adopt a spherical shape and in some cases appear to be ruptured. However, *HCe-S*, *YCe-A* and *YCe-S* show a small population of Schwann cells attached and spreading. Of the samples with attached and spreading Osteoblast and Schwann cells SEM images were collected after fixation and are presented in Figures 6 and 7. In Figure 5-11 it can be seen that the

disks containing Y and Ce all support osteoblast attachment and spreading. Schwann cells, at high magnification, are not as easily visible as osteoblasts, therefore Figure 5-12 includes 30X images showing the presence of Schwann cells (the darker spotting) across the *HY-S* and *YCe* disk surfaces.

## 5.5 DISCUSSION

The bioactivity of Y and Ce inclusive glass-ceramics for the reduction of oxidative stress generated by excess calcium and ROS upon nerve injury was evaluated after incubation in SBF for 1, 7, and 14 days. The increase in pH seen is similar to that observed in typical bioactive glasses,<sup>96</sup> where the *Con-A* glass saw the greatest spike from 9.7 after 1 day to 10.0 after 14 days. There is a direct relationship between the increase in pH and the dissolution of the glass network, relating to the initial exchange of hydrogen ions ( $H^+$ ) with  $Na^+$ . This exchange is most pronounced in the *Con* glass-ceramics as they contain the highest Na content. In addition, they lack the trivalent/tetravalent Y and Ce ions which reduce the mobility of Na through the network as a result of steric hindrance or charge compensation requirements, thereby reducing the Na content available for exchange upon glass dissolution.<sup>115,158,160,216</sup> As such, glass-ceramics containing Y and Ce show a maximum increase in pH of 8.7 which is below that observed for the *Con* glass-ceramics at any time period. The lower shift in pH observed with the Y and Ce containing glass ceramics may also influence cell viability studies and compatibility. Biological environments maintain pH for proper functioning of cells, and while moderate fluctuations in pH may be buffered within physiological fluids, greater shifts can lead to apoptosis in adjacent cells. Therefore, lower shifts in pH are desired with any biomaterial to minimize adverse effects on surrounding tissues. As such and regardless of thermal processing, the Y and Ce containing glass-ceramics elicit a lower pH than the *Con* glass-ceramics. In addition, *Con* glass-ceramics will likely have greater initial ion exchange, consistent with work on the solubility of these glass-ceramics which found the overall network solubility was significantly higher than that of the Y and Ce containing glass-ceramics.<sup>198</sup> Another trend is observed in the pH for *Con* and *HCe* glass-ceramics where samples processed at lower temperatures (*A*) show higher pH than those processed at higher temperatures (*S*). This is due to the degree of crystallinity imparted on the structures after thermal processing.

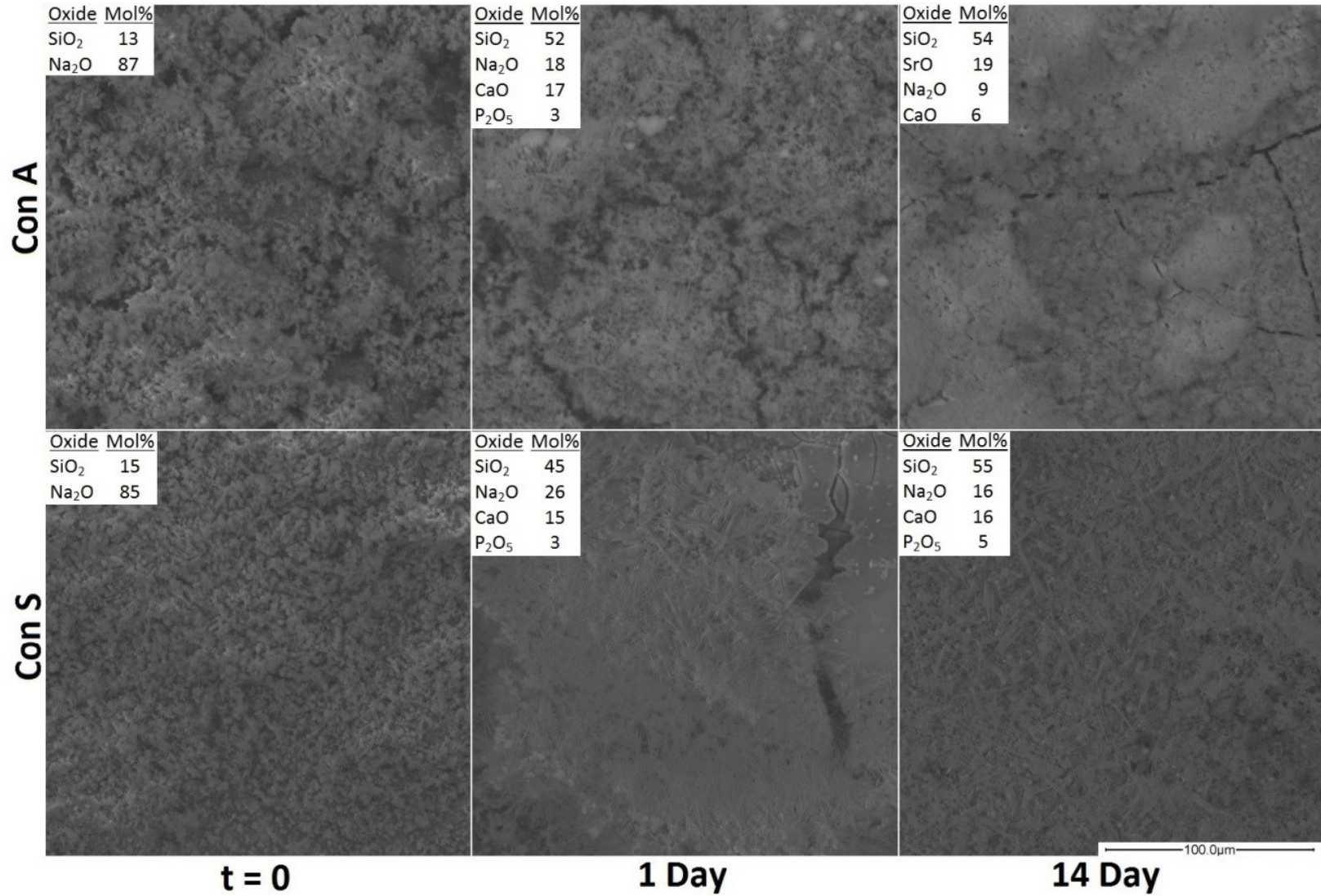


Figure 5-5. SEM images of t = 0, 1, and 14 day SBF incubated disks at 500X and EDX generated oxides list for *Con*.

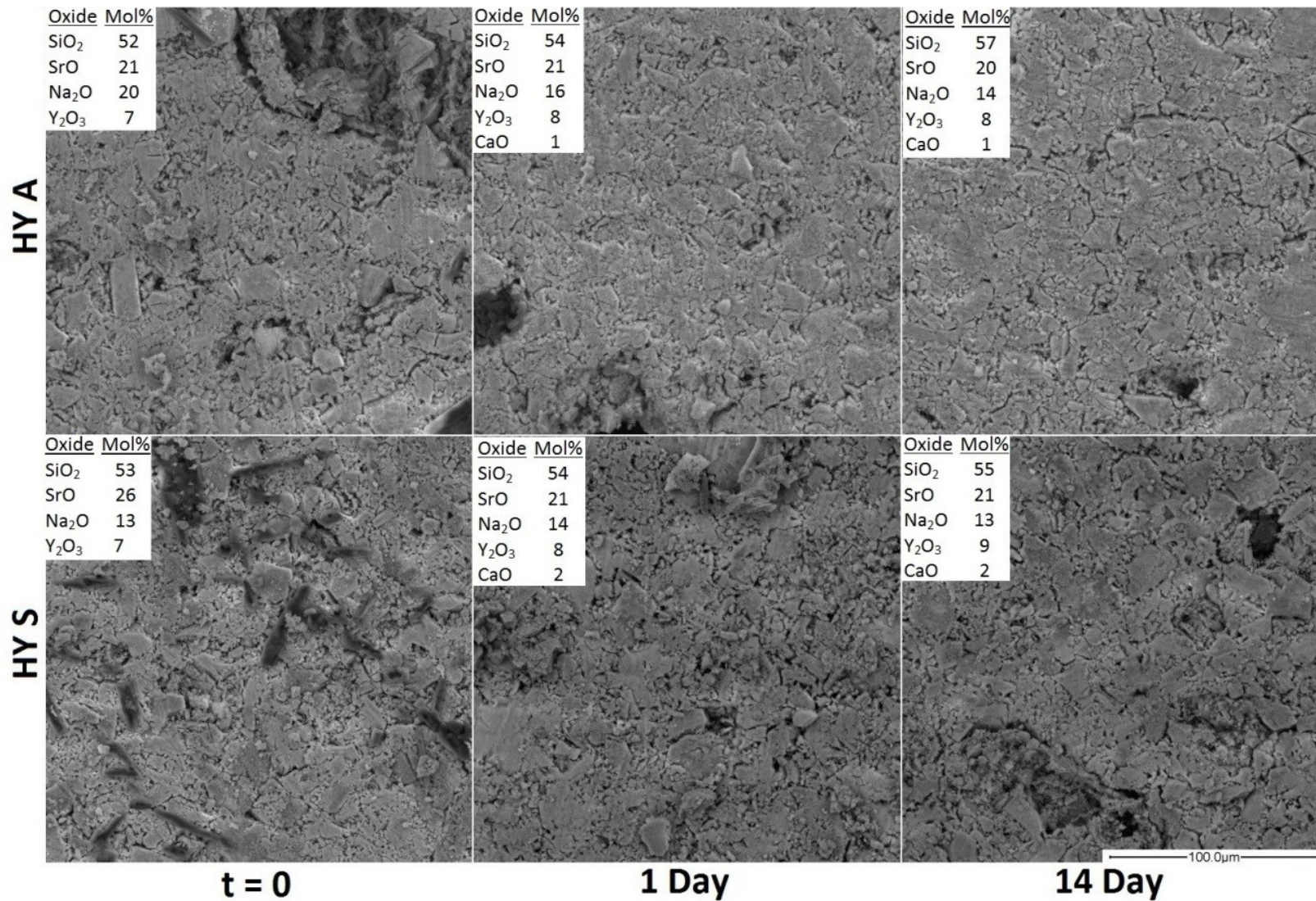


Figure 5-6. SEM images of t = 0, 1, and 14 day SBF incubated disks at 500X and EDX generated oxides list for *HY*.

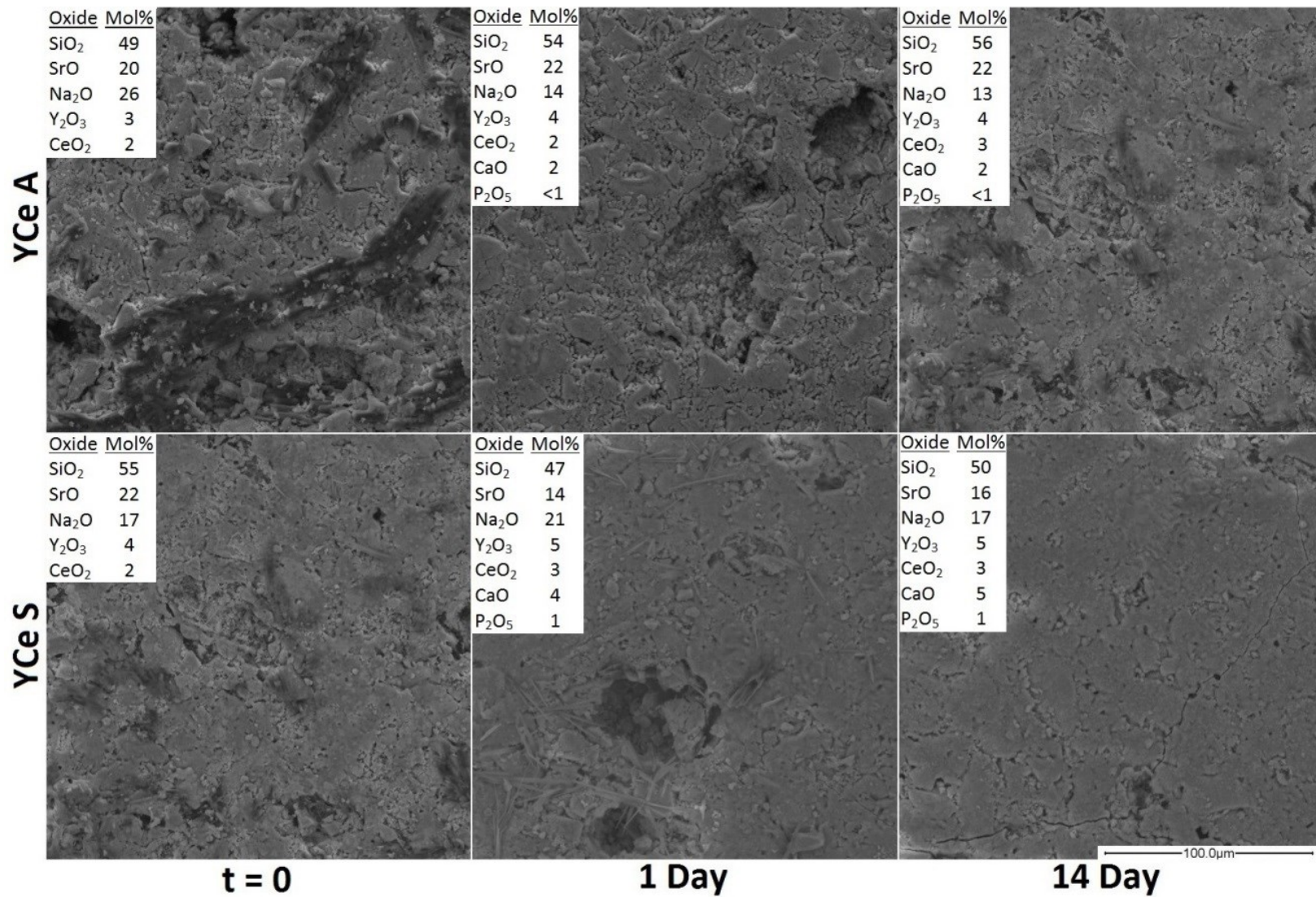


Figure 5-7. SEM images of t = 0, 1, and 14 day SBF incubated disks at 500X and EDX generated oxides list for YCe.

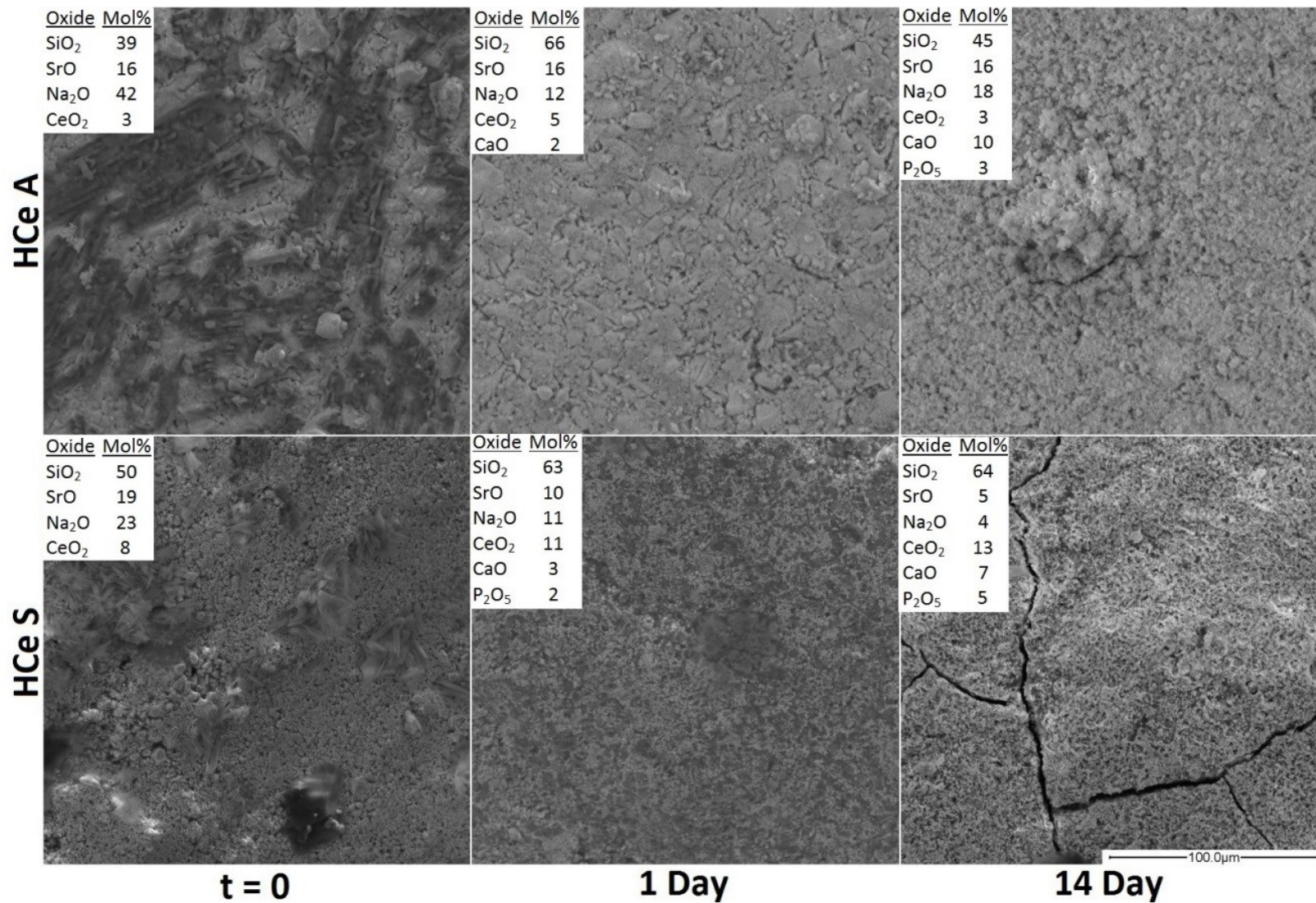


Figure 5-8. SEM images of t = 0, 1, and 14 day SBF incubated disks at 500X and EDX generated oxides list for *HCe*.

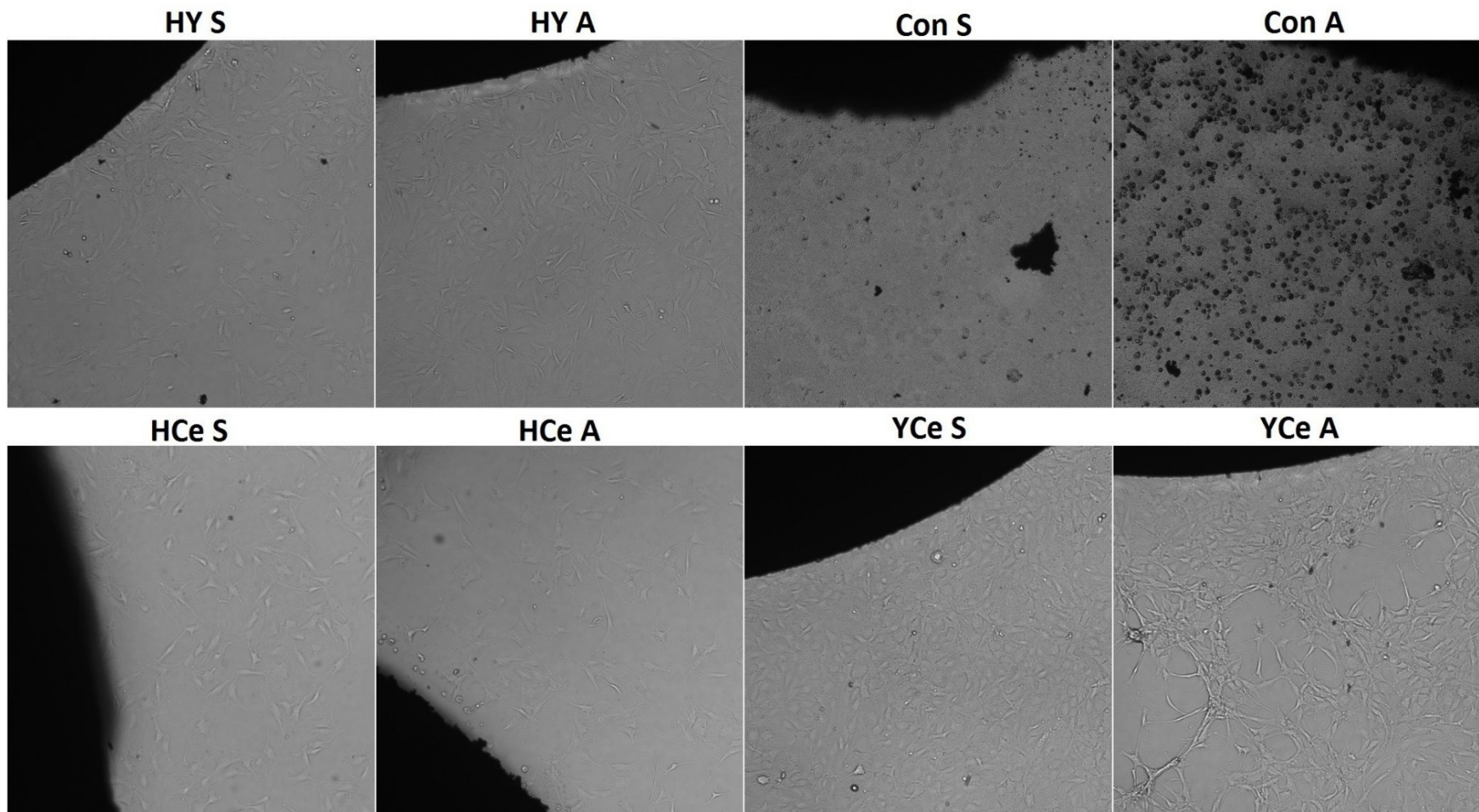


Figure 5-9. Optical images at 4X of 14 day incubated disk-Osteoblast interface after 24 hr incubation.

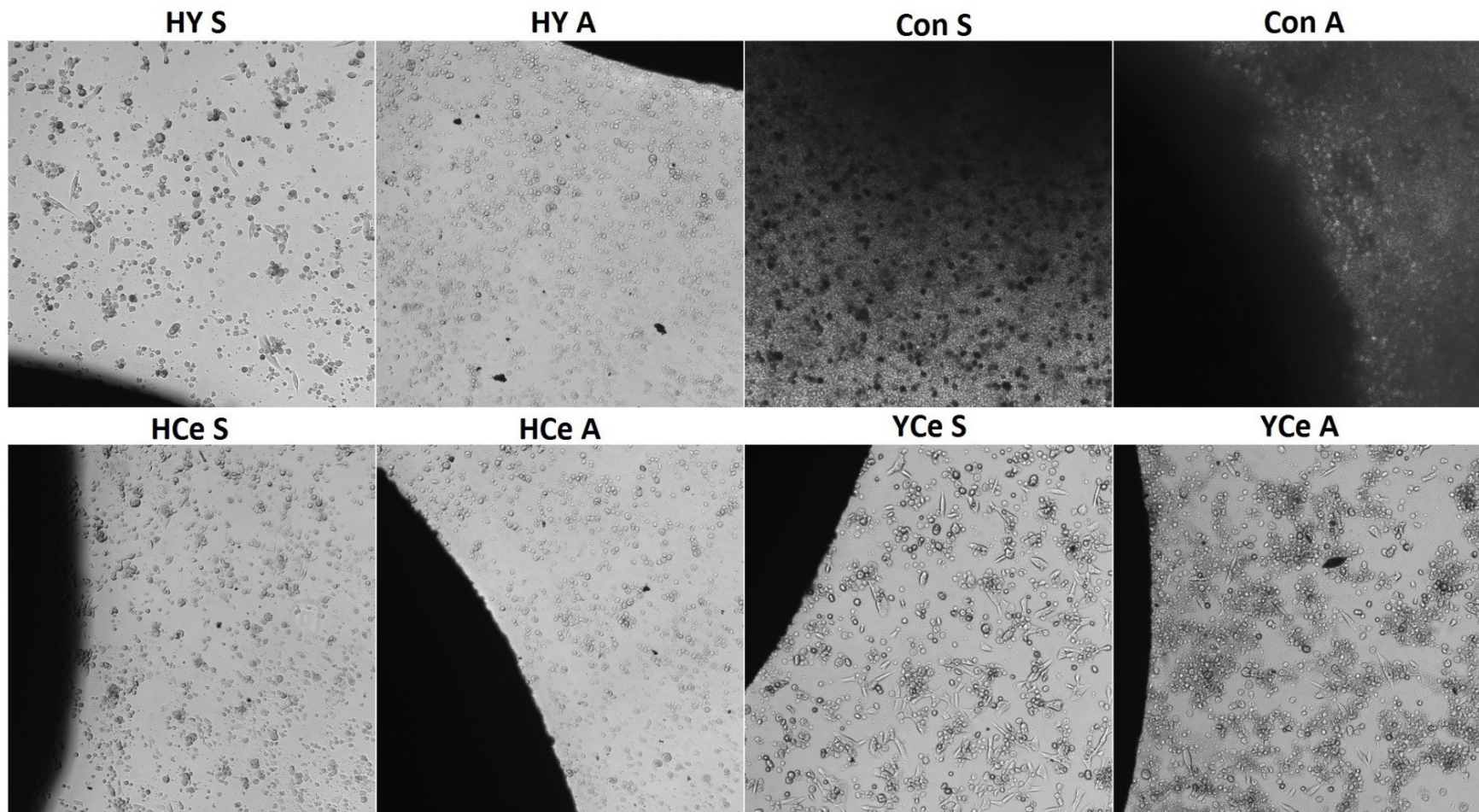


Figure 5-10. Optical images at 4X of 14 day incubated disk-Schwann interface after 24 hr incubation.

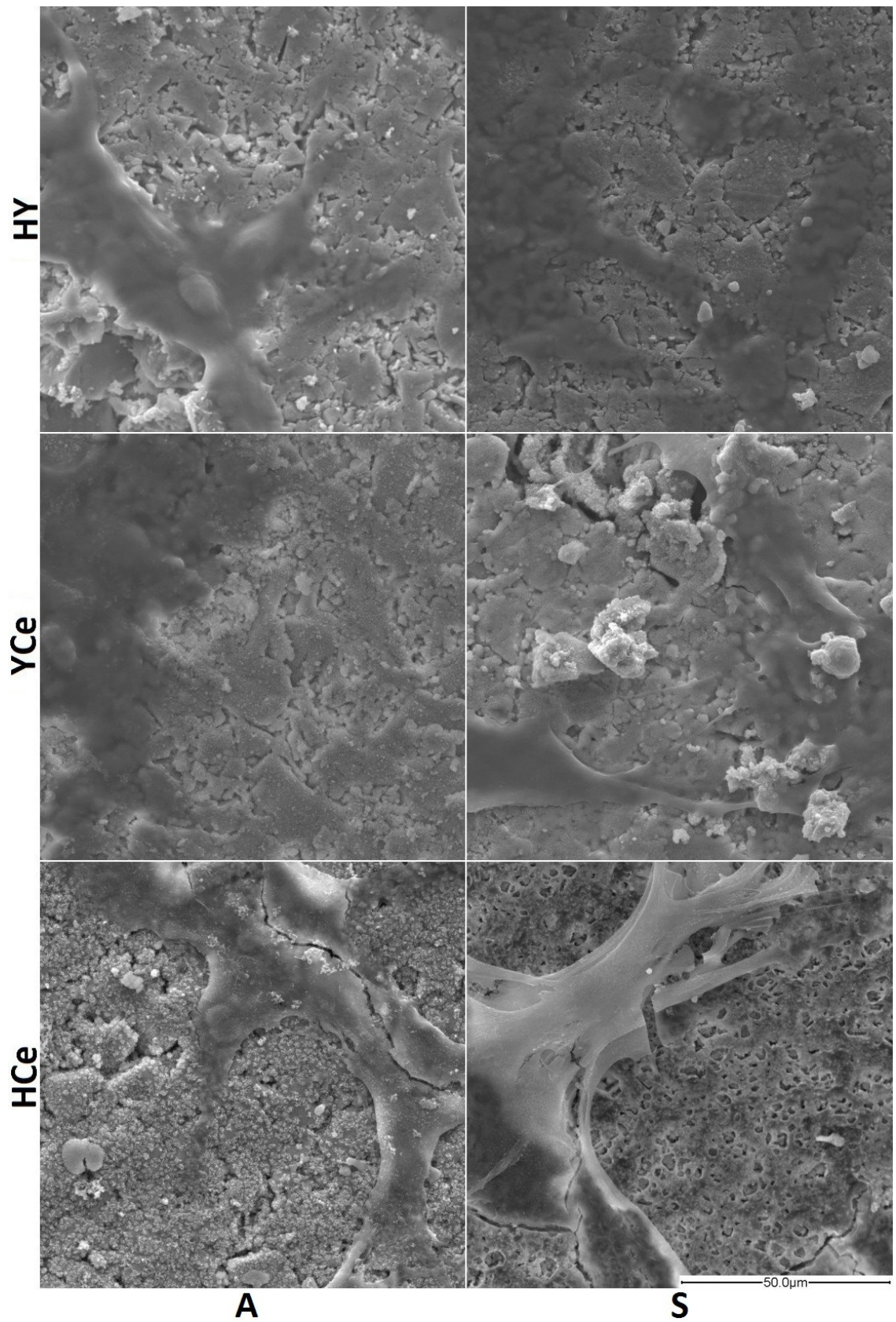


Figure 5-11. SEM images at 1kX after disk incubation with Osteoblasts and fixation.

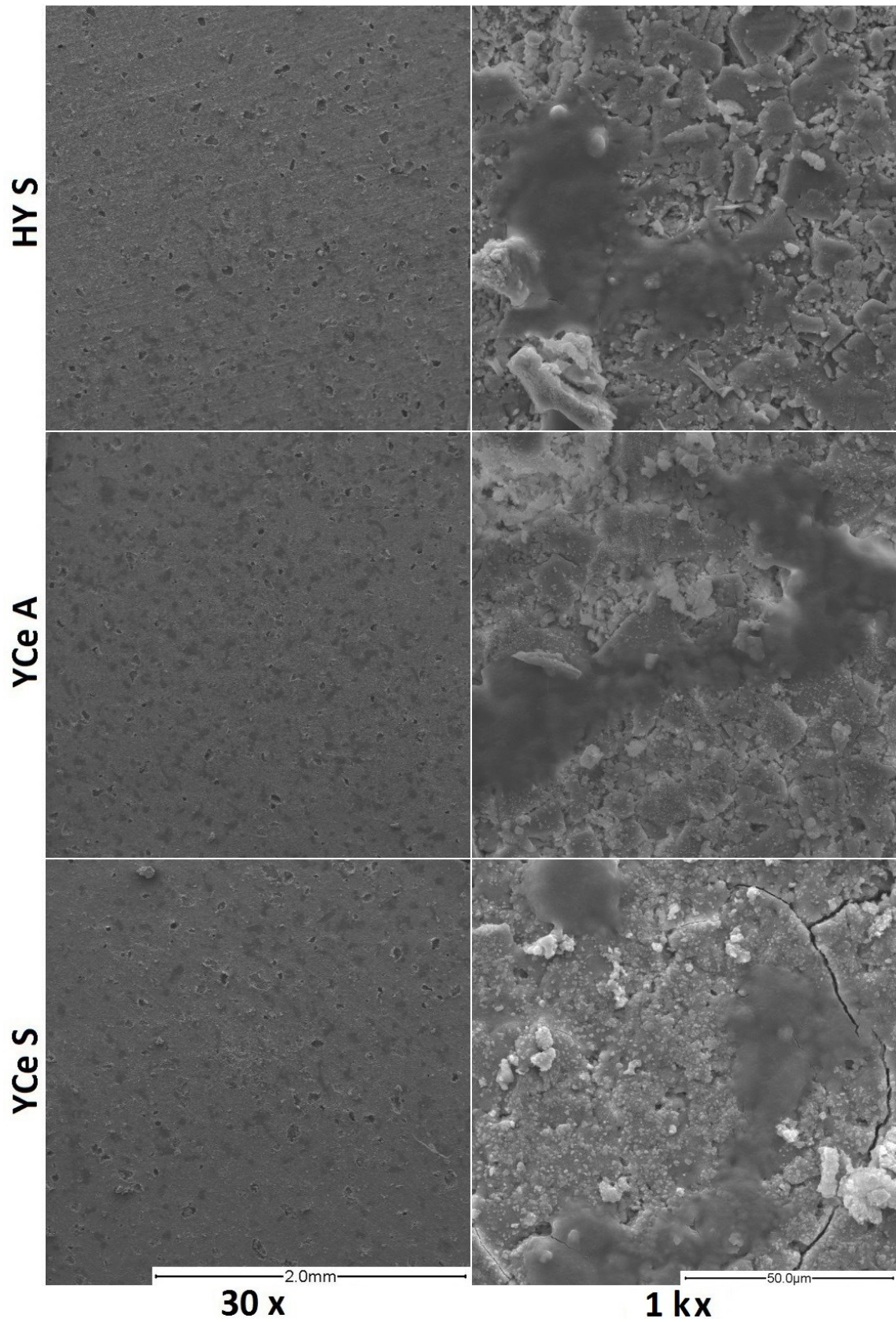


Figure 5-12. SEM images at after disk incubation with Schwann cells and fixation.

Glass quenching often freezes molecules with bond lengths that are not optimum and therefore stressed; thermal treatment at and above the  $T_g$  allows these bonds to relax and at higher temperatures reform in crystalline structures.<sup>91,119</sup> The presence of periodic atomic arrangement increases the rigidity of the material and decreases the solubility, and, in general, the greater degree of crystallinity the lower dissolution potential of a material.<sup>122,124</sup> *HY* and *YCe* glass-ceramics do not show a significant difference in pH increase at any time period throughout the SBF incubation. This is suggestive that their reactivity is inherently lower than that observed for *Con* and *HCe*, where initial studies evaluating the glass solubility in DI water found these glass compositions to have reduced solubility.<sup>198</sup> The high Y content (8 mol%) in the *HY* composition and the additive effects of 4 mol% of both Y and Ce in the *YCe* glasses, produce an increase in network rigidity attributed to the higher field strength of Y and Ce in comparison with Na. It was also found that while both Y and Ce have increased field strength Y produces greater network rigidity due to the presence of a single valence state and ability to partially stabilize the multiple valences adopted by Ce in the glass network. As a result of the multiple valences and coordination environments associated with the Ce ions, charge compensation, and field strength, local network rigidity around the Ce ions varies within the glass network. This results in slightly higher dissolution potential for Ce containing glass-ceramics in comparison with those containing Y.<sup>115,158,160,216</sup> Thus, while thermal treatments inducing crystallinity in the glasses should cause reduced reactivity in the *S* processed glass-ceramics, the rigidity of Y containing *A* samples must be at a level comparable to that observed for the crystalline phases generated through *S* temperature processing. While pH changes based on glass-ceramic dissolution does not show a significant difference between the *A* and *S* processed Y containing disks, there are differences in surface conditions indicated by Ca and P fluctuations in SBF over the incubation period.

The reduction in Ca content over the 14 day SBF incubation suggests adequate reactivity to produce surface conditions, specifically the proportion of negatively charged silanol groups, and encourage the association and chemisorption of Ca onto the surface, followed by  $PO_4$  for charge neutralization.<sup>95,162</sup> *Con*, with the highest pH, suggesting the greatest reactivity, shows elimination of Ca in solution for both *A* and *S* samples,

suggesting significant calcium precipitation on the sample surface. Since the reacted surface dictates the association with Ca ions and thus facilitates deposition; glass-ceramics processed at lower temperatures, with higher reactivity, would be expected to produce greater Ca reduction from solution, as seen for each of the *A* vs *S*, *Y* and *Ce* containing samples. However, considering the trends in pH and Ca content for the *Y* and *Ce* containing glasses and the effects of *Y* in comparison with *Ce* on rigidity, the reduced pH and minimal Ca deposition seen for the *HCe-S* glass-ceramic samples relates to a lower reactivity than expected. This is likely due to the presence of *Ce* crystallites at the surface of these samples, which is not observed in other *Ce* containing samples, and is attributed to the high sintering temperature of the *HCe* glass composition. The concentration of *Ce* crystallites likely impede surface reactions creating silanols (Si-OH), thereby reducing the potential for Ca deposition. *P* follows identical trends to that of Ca with the *Y* and *Ce* containing glass-ceramics where all samples cause a decrease in *P* content throughout the 14 day incubation period. *A* samples cause a greater *P* decrease than *S* and *HCe-S* demonstrates the lowest propensity to cause *P* precipitation, all of which can be accounted for through the same mechanisms. One difference of note is the precipitation rates of Ca and *P*, where Ca shows a linear decrease over the 14 days and *P* shows greater precipitation between the 1 and 7 days than between 7 and 14 days. The variation in rates may be accounted for by the ratio of Ca:*P* typically found in the amorphous HCA layer on bioactive materials which ranges from 1.54-1.73 with the optimum of 1.67.<sup>217</sup> As such, after 7 days it is likely that this ratio is approached and deposition rate is reduced. *Con* glass-ceramics do not show similar *P* trends to that of Ca, although it does show an initial decrease greater than that of any *Y* or *Ce* containing sample. However, after 14 days the *P* content increases from levels seen after 7 days suggesting re-release into solution. This may be indicative of continued degradation of the glass-ceramic as release of Na was found to continue throughout the 14 day incubation period.<sup>198</sup> EDS complements ICP-OES through relative comparison of surface species on the glass-ceramic disks, and may provide further insight into Ca and *P* deposition trends.

SEM images of the *Con* glass-ceramics correlate with the high reactivity suggested by pH and ICP-OES studies where the *t* = 0 disks show a reacted Na rich

surface layer. Once incubated the surface Na decreases, likely dissolving into the SBF and promoting the deposition of Ca and P which are significant after 1 day in correlation with the levels detected in SBF. In addition, after 14 days the *Con-A* samples show reduction of Ca on the surface and elimination of P, also consistent with the significant re-release of P observed through ICP-OES. This effect is less pronounced in the *Con-S* samples where 1 and 14 day Ca and P levels were comparable as listed by EDS. Visually the Ca and P deposition are presented as small meshed needle-like crystallites at higher Ca content and a porous amorphous deposition at lower concentrations. In contrast, visual depositions on the surfaces of *HY*, *YCe* and *HCe-A* glass-ceramics are nearly undetectable in the SEM images, however consistent with the reduction in both Ca and P in SBF, EDS detected small quantities of Ca, and in the case of *YCe* samples, P on the surfaces. Previous studies with Y and Ce containing bioactive glasses saw the delay of HCA formation up to 14 days based on the glass composition.<sup>115,116</sup> In addition to comparable quantities of Y and Ce in compositions used in this study, the resulting glasses were thermally treated to produce glass-ceramics, which can further reduce the bioactivity. Therefore, therefore it may require additional time for Ca and P deposition to form a visual HCA layer. This is supported by the visual deposits on the 14 day *HCe-A* samples, which have been shown to have reactivity between *Con* and other Y and Ce glass-ceramics through pH and ICP-OES. These deposits and relative Ca content appears to fall, visually, between the amorphous character of *Con-A*, 14 day deposits and the crystallites seen on samples with higher Ca content. *HCe-S* samples show incremental increase in the Ca and P content detected on the surface where deposition appears in a thin distribution across the disk surface. The presence of Ca and P detected on the surface of each disk indicates a degree of bioactivity for each, and potential for adherence of cells to these surfaces.

Cell attachment and morphology gives insight into the biocompatibility of a material. Optical microscopy of the *Con* glass-ceramic disks incubated for 24 hrs with cells show reduced clarity of the media associated with gelation and unattached spherical cells. The gelation of the liquid media upon incubation is suggestive of continued reactivity and significant silica release. When approaching the saturation limit silica can polymerize potentially causing an increase in media viscosity and an inhospitable

environment for Osteoblast and Schwann cell lines.<sup>178-180</sup> Y and Ce containing glasses with reduced reactivity do not cause this phenomena and, as such, cell attachment occurs in each well for these samples. In addition to attachment, Osteoblasts exhibit cell spreading and growth across the well, uninhibited by proximity to the disks. This correlates to the results obtained from osteoblast viability analysis conducted with the SBF incubated disk extracts. Statistical analysis revealed there was no significant difference between any of the sample incubated populations and the control population. These two observations show the Y and Ce containing glass-ceramics are not toxic to osteoblasts after processing at either temperature and therefore may have the potential for cell adhesion directly to the sample surfaces. Therefore, SEM was employed and shows the presence of osteoblast cells attached and spreading across each Y and Ce containing glass-ceramic. While there was no toxicity and favorable cell morphologies with Osteoblasts, they tend to be robust compared to Schwann cells. This is illustrated in the optical images of disk incubation with Schwann cells where cell attachment of spherical cells is observed in each well, but growth and spreading only occurs in the *HY-S*, and *YCe* disk sample wells and is limited to a fraction of the population. This indicates adverse effects on Schwann cells in proximity with the disks, possible toxicity over time, and may eliminate the potential for cell growth and attachment on the disk surface. However, when the best performing disks *HY-S*, *YCe-A*, and *YCe-S* were observed through SEM, low magnification images revealed the presence of cells that exhibited spreading across the surfaces. Cells do not form a connected network across the disks and are singular or in small groups. Schwann cells function in close proximity *in vivo* and therefore achieving a network as observed with the Osteoblasts would be beneficial and presents a direction for future research.

## 5.6 CONCLUSION

The ability of bioactive glasses to interact with physiological fluids and induce the deposition of a HCA layer is essential to the formation of a bond with host tissues. This work has shown *Con* glass-ceramics to have the greatest reactivity with the highest increase in pH and the greatest reduction in Ca content from SBF. In addition, Ca and P deposition appear as a mesh of needle like crystallites, however despite the lack of osteoblast toxicity observed through viability analysis when directly incubated with cells

*Con* samples cause complete toxicity to both cell populations. Y and Ce containing glasses show reduced reactivity with moderate pH increases in SBF upon incubation and reduction of Ca and P content and corresponding deposition. However, only *HCe-A* shows significant Ca and P deposition suggesting the bioactivity may be delayed by more than 14 days for the remaining Y and Ce containing glass-ceramics. Observation of cells in direct contact with Y and Ce containing glass ceramics suggest only *HY-S*, *YCe-A* and *YCe-S* are suitable surfaces for cell attachment of both Osteoblasts and Schwann cell types. While bioactivity was demonstrated for *Con* and *HCe-A* glass-ceramics, the combination of bioactivity and direct cell compatibility suggests *HY-S*, *YCe-A* and *YCe-S* may prove better candidates considering the sensitive nature of regenerating nerve tissues.

## CHAPTER 6 - SUMMARY

### 6.1 BASIS & HYPOTHESIS

Biological response after SCI can cause Ca mediated necrosis through excitotoxicity and oxidative stress to the damaged axon(s) and adjacent tissues effectively impeding nerve regeneration, reconnection, and recovery of sensory and/or motor function.

Glass-ceramics containing yttrium and/or cerium can serve as a bioactive framework for nerve growth, support restoration of ion homeostasis, and provide antioxidant protection.

### 6.2 THESIS OBJECTIVES

- Synthesize a series of Y and Ce containing  $\text{SiO}_2\text{-SrO-Na}_2\text{O}$  glasses.
- Determine the structural role of Y and Ce in the glass network.
- Determine glass solubility and cytocompatibility.
- Use thermal characteristics to develop profiles for thermal processing.
- Synthesize a glass ceramic series and determine phases present.
- Characterize the physical properties and reactivity of the glass-ceramic series.
- Assess antioxidant capacity of glass extracts, glass-ceramic particulate, and glass-ceramic extracts.
- Determine bioactivity of the glass-ceramics.
- Observe cell attachment on glass-ceramic surface.

### 6.3 THESIS CONCLUSIONS

#### 6.3.1. Ch. 2 Characterization of Glasses

- XRD confirmed all glasses are amorphous.
- $T_g$  increases with increasing Y and Ce content and shows a greater increase for Y containing glasses.

- $^{29}\text{Si}$  MAS-NMR shows minimal shift in Q-distribution between Y and the control glass ( $Q^2 - Q^3$ ).
- $^{29}\text{Si}$  MAS-NMR shows peak broadening and shifts toward  $Q^3$  species with an increasing  $Q^4$  shoulder for Ce containing glasses.
- HiRes XPS for Si 2p, Sr 3d, Na 1s, Y 3d, Ce 3d does not show significant peak shifting between glasses.
- HiRes XPS for Ce 3d reveals a multiplet of peaks with contributions from both Ce III and Ce IV where increasing Ce content increases Ce IV contributions.
- Addition of Y and Ce shifts the O 1s NBO and BO peaks to slightly higher BE.
- The ratio of BO:NBO decreases with increasing Y and Ce content.
- Schwann cells were able to attach and spread over polished bulk-glass surfaces.

### 6.3.2. Ch. 3 Solubility Cytocompatibility & Antioxidant Capacity of Glasses

- pH ranges from 11.2 to 12.7 when glasses are incubated from 1 – 30 days in DI water.
- Ion release is significantly higher from the *Con* glass which greatly exceeds levels seen in physiological fluids.
- Sr release from the Y and Ce containing glasses is in the optimum serum range for bone mineralization and decreases after 30 days, suggesting it is precipitating.
- *Con*, *LCe*, and *LY* glass extracts decreased viability of fibroblasts and osteoblasts, and significantly inhibited *E. coli* and *S. aureus* growth at all doses and time periods.
- *HCe* glass extracts exhibited dose dependent fibroblast and osteoblast toxicity as well as time dependent *E. coli* and *S. aureus* inhibition.
- *HY* and *YCe* glass extracts showed minimal cell toxicity and bacterial inhibition at all doses and time periods.
- All glass extracts show antioxidant capacity in a mMTE range.

### 6.3.3. Ch. 4 Effect of Crystallization on Solubility & Antioxidant Potential

- With the exception of *HCe-S* all glass-ceramics presented 1-7% shrinkage upon thermal processing.
- *HCe-S* experienced 17% shrinkage in diameter and a 60% expansion in thickness.

- *Con* glass-ceramics presented a primary  $\text{Na}_6\text{Sr}_3\text{Si}_6\text{O}_{18}$  phase.
- XRD and SEM shows the presence of sodium-(strontium)-yttrium-silicates for Y glass-ceramics and presence of sodium-cerium-silicates/oxide crystallites dispersed in a strontium-silicate phase in Ce glass-ceramics.
- Si ion release decreases with thermal processing though is still greater for the *Con* glass-ceramics in comparison with the Y and Ce glass-ceramics which are in the 127-325  $\mu\text{g}/\text{mL}$  range throughout the 14 day period.
- Sr release from *Con* glass-ceramics is reduced, while the Y and Ce glass ceramics release significantly greater quantities than those observed for their glassy counterparts.
- Na content precipitates from SBF after 14 day incubation with Y and Ce glass-ceramics.
- Antioxidant capacity of the un-incubated glass-ceramic particulates is higher than the 7 day incubated samples, and falls between the capacities of glass extracts and glass-ceramic extracts.
- Antioxidant capacity of the glass-ceramic extracts are reduced in comparison to the glass extracts.
- *Con* samples display significantly higher antioxidant capacity than Y and Ce samples.

#### 6.3.4. Ch. 5 Bioactivity and Cytocompatibility of Glass-Ceramics

- pH ranges from 7.8 to 10.0 when disks are incubated from 1 – 14 days in SBF where *A* samples produce slightly higher pH in comparison to *S*.
- Ca and P levels decrease over the 14 day incubation period.
- SEM shows a varying degree of amorphous and crystalline Ca and P deposited on the surfaces of *Con* and *HCe-A* glass-ceramics confirmed by EDS.
- EDS suggests there may be some deposition of Ca and P on *HY*, *YCe* and *HCe-S* glass-ceramics.
- Glass-ceramic extracts did not decrease osteoblast viability.
- Optical and SEM images show osteoblast compatibility and attachment on Y and Ce glass-ceramics.
- Optical and SEM images show Schwann cell compatibility and attachment on *HY-S* and *YCe* glass ceramics.

In the glasses, Y and Ce are acting as network modifiers while increasing the characteristic temperatures due to the differences in field strength with Na for which they are substituting. In a modifying role, NC and Si speciation distributed between  $Q^2$  and  $Q^3$  suggest the glass series will elicit a bioactive response. However, solubility resulted in ion release exceeding physiological levels and in combination with increasing the basicity of the incubation media caused dose dependent cytotoxicity. Despite the release related toxicity, Si release and polymerization to form silicic acid species, may be the mechanism for the observed mMTE antioxidant capacity. In addition, decreasing Sr levels further support potential biocompatibility when considering the similarities between Ca and Sr. Fibroblast/Osteoblast and bacterial compatibility is inverse to solubility and antioxidant capacity where glass cytocompatibility falls in the order: **Con** < *LCe* < *LY* < **HCe** < **YCe** < **HY**. The bolded glasses were elected for further study. Upon thermal treatment sintering and crystallization occurs where the generated phases may be analogous to those found to be bioactive after 45S5 crystallization. The generation of crystalline phases in the glasses reduces the solubility but maintains potential for bioactivity based on Ca and P ion content reduction in SBF and detection through SEM/EDS. In addition, while antioxidant capacity is reduced, ROS scavenging potential remains in the mMTE range. The potential for antioxidant capacity appears to correlate with the reactivity, further supporting that silanol and silicic acid species generated upon dissolution may provide the mechanism. Oppositely, cell compatibility favors the glass-ceramics demonstrating lower reactivity, where both osteoblasts and Schwann cells were able to attach and spread across the *HY-S* and *YCe* glass-ceramic surfaces. While Y and Ce do not appear to impart similar antioxidant scavenging capability to these bioactive glass/glass-ceramics, the capacity is shown and therefore the potential to alleviate oxidative stress after SCI exists with further development.

#### 6.4 FUTURE WORK

There are two aspects within this work for which the mechanism behind the behaviour is not clear and therefore should be addressed. The first is the significant increase of Sr release upon crystallization from the Y and Ce glass-ceramics while the *Con* sample release was significantly reduced. The second relates to the mechanism behind the observed antioxidant behaviour, where factors, such as ionic species relative

to pH should be evaluated in a manner where the effect of each may be distinguished from the system through a designed experiment. Another direction for future work is the surface modification of these glass ceramics, to evaluate the extent the surface chemistry and charge affects the cellular attachment. Related work would involve the incorporation of these glass-ceramics in PLGA fibre sheets or creation of similar glass fibres which could then be and thermally processing to generate crystalline phases. With these composite fibre sheets Dorsal Root Ganglion (DRG) studies can be completed to evaluate the compatibility and extension of spinal nerve tissue with the bioactive glass-ceramic. Additionally scaffolds could be produced and evaluated in terms of mechanical properties for use as a potential structural support and cell seeding and migration can be assessed as a delivery device.

## REFERENCES

1. E. C. B. Hall-Craggs, *Anatomy as a Basis for Clinical Medicine*, 3ed.; p. 587. Williams & Wilkins, Baltimore, MD, 1995. Image accessed at <<http://www.emory.edu/ANATOMY/AnatomyManual/back.html>>
2. M. Headworth, "Anatomy of the Spine" (2016) Mayfield Clinic. Accessed at <<http://www.mayfieldclinic.com/PE-AnatSpine.htm>>
3. Reprinted from *Prog Neurobiol*, **114**, N. A. Silva, N. Sousa, R. L. Reis, and A. J. Salgado, "From Basics to Clinical: A Comprehensive Review on Spinal Cord Injury," 25-57 (2014) with permission from Elsevier.
4. Reprinted from *Anaesth Intens Care Med*, **7** [11], H. Ellis, "Anatomy of the Spinal Nerves and Dermatomes," 405-6 (2006) with permission from Elsevier.
5. C. Rey, C. Combes, C. Drouet, and M. J. Glimcher, "Bone Mineral: Update on Chemical Composition and Structure," *Osteoporosis Int*, **20** [6] 1013-21 (2009).
6. B. Wopenka and J. D. Pasteris, "A Mineralogical Perspective on the Apatite in Bone," *Mater Sci Eng C*, **25** [2] 131-43 (2005).
7. F. H. Martini, J. L. Nath, and E. F. Bartholomew, "Intervertebral Articulations"; p. 264 in *Fundamentals of Anatomy & Physiology*. 9<sup>th</sup> Edition, ©2012. Printed and electronically reproduced by permission of Pearson Education, Inc., Upper Saddle River, NJ.
8. Reprinted from *Medical Engineering & Physics*, **20** [2], J.-Y. Rho, L. Kuhn-Spearing, and P. Zioupos, "Mechanical Properties and the Hierarchical Structure of Bone," 92-102 (1998) with permission from Elsevier.
9. R. Z. Le Geros and J. P. Le Geros, "Dense Hydroxyapatite"; pp. 39-180 in *An Introduction to Bioceramics*. Edited by L. L. Hench and J. Wilson. World Scientific, Singapore, 1993.
10. C. M. Kielty and M. E. Grant, "The Collagen Family: Structure, Assembly, and Organization in the Extracellular Matrix"; pp. 103-47 in *Connective Tissue and Its Heritable Disorders*. Edited by P. M. Royce and B. U. Steinmann. Wiley-Liss, New York, 1993.
11. K. A. Hing, "Bone Repair in the Twenty-First Century: Biology, Chemistry or Engineering?," *Philos Trans R Soc A*, **362** [1825] 2821-50 (2004).
12. Reprinted from *J Biotech*, **156** [4], S. Sprio, A. Ruffini, F. Valentini, T. D'Alessandro, M. Sandri, S. Panseri, and A. Tampieri, "Biomimesis and

- Biomorphic Transformations: New Concepts Applied to Bone Regeneration," 347-55 (2011) with permission from Elsevier.
13. M. Owen, "Histogenesis of Bone Cells," *Calcified Tissue Int*, **25** [1] 205-7 (1978).
  14. F. P. Ross, "Cytokine Regulation of Osteoclast Formation and Function," *J Musculoskelet Neuronal Interact*, **3** [4] 282-6 (2003).
  15. W. T. Butler, "Noncollagenous Proteins of Bone and Dentin: A Brief Overview"; pp. 137-41 in *Chemistry and Biology of Mineralized Tissue*. Edited by M. Goldberg, A. Boskey and C. Robinson. American Academy of Orthopedic Surgeons, Rosemont, IL, 2000.
  16. L. C. Gerstenfeld, S. Shih, C. George, S. Mizumo and J. Glowacki, "Effect of Overexpression of Bone Sialoprotein on Osteosarcoma Tissue Growth and Mineralization"; pp. 143-8 in *Chemistry and Biology of Mineralized Tissue*. Edited by M. Goldberg, A. Boskey and C. Robinson. American Academy of Orthopedic Surgeons, Rosemont, IL, 2000.
  17. P. Yang and Z. Yang, "Enhancing Intrinsic Growth Capacity Promotes Adult Cns Regeneration," *J Neurol Sci*, **312** [1-2] 1-6 (2012).
  18. C. Tohda and T. Kuboyama, "Current and Future Therapeutic Strategies for Functional Repair of Spinal Cord Injury," *Pharm Therap*, **132** [1] 57-71 (2011).
  19. F. Sun and Z. He, "Neuronal Intrinsic Barriers for Axon Regeneration in the Adult Cns," *Curr Opin Neurobiol*, **20** [4] 510-8 (2010).
  20. M. T. Fitch and J. Silver, "Cns Injury, Glial Scars, and Inflammation: Inhibitory Extracellular Matrices and Regeneration Failure," *Exp Neurol*, **209** [2] 294-301 (2008).
  21. T. A. Ferguson and Y. J. Son, "Extrinsic and Intrinsic Determinants of Nerve Regeneration," *J Tissue Eng*, **2** [1] (2011).
  22. N. S. C. I. S. Center, "Facts and Figures at a Glance" (2015) University of Alabama at Birmingham. Accessed on: Available at <[www.uab.edu/nscisc](http://www.uab.edu/nscisc)>
  23. L. H. S. Sekhon and M. G. Fehlings, "Epidemiology, Demographics, and Pathophysiology of Acute Spinal Cord Injury," *Spine*, **26** [24S] S2-12 (2001).
  24. Reprinted by permission from Macmillan Publishers Ltd: [*Nat Rev Neurosci* ] (J. Silver and J. H. Miller, "Regeneration Beyond the Glial Scar," *Nat Rev Neurosci*, **5** [2] 146-56) copyright (2004).

25. G. Mandolesi, F. Madeddu, Y. Bozzi, L. Maffei, and G. M. Ratto, "Acute Physiological Response of Mammalian Central Neurons to Axotomy: Ionic Regulation and Electrical Activity," *FASEB J*, **18** [15] 1934-6 (2004).
26. A. Ghosh-Roy, Z. Wu, A. Goncharov, Y. Jin, and A. D. Chisholm, "Calcium and Cyclic Amp Promote Axonal Regeneration in *Caenorhabditis Elegans* and Require Dlk-1 Kinase," *J Neurosci*, **30** [9] 3175-83 (2010).
27. M. Hammarlund, P. Nix, L. Hauth, E. M. Jorgensen, and M. Bastiani, "Axon Regeneration Requires a Conserved Map Kinase Pathway," *Science*, **323** [5915] 802-6 (2009).
28. C. C. Stichel and H. W. Müller, "Experimental Strategies to Promote Axonal Regeneration after Traumatic Central Nervous System Injury," *Prog Neurobiol*, **56** [2] 119-48 (1998).
29. C. H. Tymianski and M. Tator, "Normal and Abnormal Calcium Homeostasis in Neurons: A Basis for the Pathophysiology of Traumatic and Ischemic Central Nervous System Injury," *Neurosurgery*, **38** [6] 1176-95 (1996).
30. L. Dugan, S. Sensi, L. Canzoniero, S. Handran, S. Rothman, T. Lin, M. Goldberg, and D. Choi, "Mitochondrial Production of Reactive Oxygen Species in Cortical Neurons Following Exposure to N-Methyl-D-Aspartate," *J Neurosci*, **15** [10] 6377-88 (1995).
31. X. Lu and P. M. Richardson, "Inflammation near the Nerve Cell Body Enhances Axonal Regeneration," *J Neurosci*, **11** [4] 972-8 (1991).
32. T. Miao, D. Wu, Y. Zhang, X. Bo, M. C. Subang, P. Wang, and P. M. Richardson, "Suppressor of Cytokine Signaling-3 Suppresses the Ability of Activated Signal Transducer and Activator of Transcription-3 to Stimulate Neurite Growth in Rat Primary Sensory Neurons," *J Neurosci*, **26** [37] 9512-9 (2006).
33. D. Bartholdi and M. E. Schwab, "Degeneration and Regeneration of Axons in the Lesioned Spinal Cord," *Physiol Rev*, **76** [2] 319-70 (1996).
34. D. W. Choi, "Calcium and Excitotoxic Neuronal Injury," *Ann NY Acad Sci*, **747** [1] 162-71 (1994).
35. J. A. Wolf, P. K. Stys, T. Lusardi, D. Meaney, and D. H. Smith, "Traumatic Axonal Injury Induces Calcium Influx Modulated by Tetrodotoxin-Sensitive Sodium Channels," *J Neurosci*, **21** [6] 1923-30 (2001).
36. R. M. LoPachin and E. J. Lehning, "Mechanism of Calcium Entry During Axon Injury and Degeneration," *Toxicol Appl Pharm*, **143** [2] 233-44 (1997).

37. D. Schubert, R. Dargusch, J. Raitano, and S.-W. Chan, "Cerium and Yttrium Oxide Nanoparticles Are Neuroprotective," *Biochem Biophys Res Com*, **342** [1] 86-91 (2006).
38. M. B. Bracken, M. J. Shepard, K. G. Hellenbrand, W. F. Collins, L. S. Leo, D. F. Freeman, F. C. Wagner, E. S. Flamm, H. M. Eisenberg, J. H. Goodman, P. L. Perot, B. A. Green, R. G. Grossman, J. N. Meagher, W. Young, B. Fischer, G. L. Clifton, W. E. Hunt, and N. Rifkinson, "Methylprednisolone and Neurological Function 1 Year after Spinal Cord Injury," *J Neurosurgery*, **63** [5] 704-13 (1985).
39. M. B. Bracken, M. J. Shepard, W. F. Collins, T. R. Holford, W. Young, D. S. Baskin, H. M. Eisenberg, E. Flamm, L. Leo-Summers, J. Maroon, L. F. Marshall, P. L. Perot, J. Piepmeier, V. K. H. Sonntag, F. C. Wagner, J. E. Wilberger, and H. R. Winn, "A Randomized, Controlled Trial of Methylprednisolone or Naloxone in the Treatment of Acute Spinal-Cord Injury," *N Eng J Med*, **322** [20] 1405-11 (1990).
40. M. T. Filbin, "Myelin-Associated Inhibitors of Axonal Regeneration in the Adult Mammalian Cns," *Nat Rev Neurosci*, **4** [9] 703-13 (2003).
41. M. S. Chen, A. B. Huber, M. E. van der Haar, M. Frank, L. Schnell, A. A. Spillmann, F. Christ, and M. E. Schwab, "Nogo-a Is a Myelin-Associated Neurite Outgrowth Inhibitor and an Antigen for Monoclonal Antibody in-1," *Nature*, **403** [6768] 434-9 (2000).
42. Z. M. Varga, M. E. Schwab, and J. G. Nicholls, "Myelin-Associated Neurite Growth-Inhibitory Proteins and Suppression of Regeneration of Immature Mammalian Spinal Cord in Culture," *Proc Natl Acad Sci U S A*, **92** [24] 10959-63 (1995).
43. M. G. Fehlings, N. Theodore, J. Harrop, G. Maurais, C. Kuntz, C. I. Shaffrey, B. K. Kwon, J. Chapman, A. Yee, A. Tighe and L. McKerracher, "A Phase I/IIa Clinical Trial of a Recombinant Rho Protein Antagonist in Acute Spinal Cord Injury," *J Neurotrauma*, **28** [5] 787-96 (2011).
44. E. J. Bradbury, L. D. F. Moon, R. J. Popat, V. R. King, G. S. Bennett, P. N. Patel, J. W. Fawcett and S. B. McMahon, "Chondroitinase Abc Promotes Functional Recovery after Spinal Cord Injury," *Nature*, **416** [6881] 636-40 (2002).
45. N. J. Tester and D. R. Howland, "Chondroitinase Abc Improves Basic and Skilled Locomotion in Spinal Cord Injured Cats," *Exp Neurology*, **209** [2] 483-96 (2008).
46. F. H. Geisler, W. P. Coleman, G. Grieco, D. Poonian, and t. S. S. Group, "The Sygen® Multicenter Acute Spinal Cord Injury Study," *Spine*, **26** [24S] S87-S98 (2001).

47. V. W. Yong, J. Wells, F. Giuliani, S. Casha, C. Power, and L. M. Metz, "The Promise of Minocycline in Neurology," *Lancet Neurology*, **3** [12] 744-51 (2004).
48. D. P. Stirling, K. Khodarahmi, J. Liu, L. T. McPhail, C. B. McBride, J. D. Steeves, M. S. Ramer, and W. Tetzlaff, "Minocycline Treatment Reduces Delayed Oligodendrocyte Death, Attenuates Axonal Dieback, and Improves Functional Outcome after Spinal Cord Injury," *J Neurosci*, **24** [9] 2182-90 (2004).
49. E. A. Sribnick, S. Samantaray, A. Das, J. Smith, D. D. Matzelle, S. K. Ray, and N. L. Banik, "Postinjury Estrogen Treatment of Chronic Spinal Cord Injury Improves Locomotor Function in Rats," *J Neurosci Res*, **88** [8] 1738-50 (2010).
50. J. Voda, T. Yamaji, and B. G. Gold, "Neuroimmunophilin Ligands Improve Functional Recovery and Increase Axonal Growth after Spinal Cord Hemisection in Rats," *J Neurotrauma*, **22** [10] 1150-61 (2005).
51. E. Woodhall, A. K. West, and M. I. Chuah, "Cultured Olfactory Ensheathing Cells Express Nerve Growth Factor, Brain-Derived Neurotrophic Factor, Glia Cell Line-Derived Neurotrophic Factor and Their Receptors," *Molec Brain Res*, **88** [1-2] 203-13 (2001).
52. L. M. Ramer, E. Au, M. W. Richter, J. Liu, W. Tetzlaff, and A. J. Roskams, "Peripheral Olfactory Ensheathing Cells Reduce Scar and Cavity Formation and Promote Regeneration after Spinal Cord Injury," *J Comp Neurol*, **473** [1] 1-15 (2004).
53. M. Sasaki, K. L. Lankford, M. Zemedkun, and J. D. Kocsis, "Identified Olfactory Ensheathing Cells Transplanted into the Transected Dorsal Funiculus Bridge the Lesion and Form Myelin," *J Neurosci*, **24** [39] 8485-93 (2004).
54. T. Osada, M. Watanabe, A. Hasuo, M. Imai, K. Suyama, D. Sakai, H. Kawada, M. Matsumae, and J. Mochida, "Efficacy of the Coadministration of Granulocyte Colony-Stimulating Factor and Stem Cell Factor in the Activation of Intrinsic Cells after Spinal Cord Injury in Mice," *J Neurosurg Spine*, **13** [4] 516-23 (2010).
55. E. Syková, A. Homola, R. Mazanec, H. Lachmann, K. Langkramer, imona, P. Kobylka, R. Pádr, J. Neuwirth, í, V. Komrska, V. Vávra, J. tulík, and M. Bojar, "Autologous Bone Marrow Transplantation in Patients with Subacute and Chronic Spinal Cord Injury," *Cell Trans*, **15** [8-1] 675-87 (2006).
56. J. E. Davies, C. Huang, C. Proschel, M. Noble, M. Mayer-Proschel and S. J. A. Davies, "Astrocytes Derived from Glial-Restricted Precursors Promote Spinal Cord Repair," *J Biol*, **5** [3] 7 (2006).
57. J. E. Herrmann, T. Imura, B. Song, J. Qi, Y. Ao, T. K. Nguyen, R. A. Korsak, K. Takeda, S. Akira, and M. V. Sofroniew, "Stat3 Is a Critical Regulator of

- Astrogliosis and Scar Formation after Spinal Cord Injury," *J Neurosci*, **28** [28] 7231-43 (2008).
58. E. C. Tsai, A. V. Krassioukov, and C. H. Tator, "Corticospinal Regeneration into Lumbar Grey Matter Correlates with Locomotor Recovery after Complete Spinal Cord Transection and Repair with Peripheral Nerve Grafts, Fibroblast Growth Factor 1, Fibrin Glue, and Spinal Fusion," *J Neuropath Exp Neur*, **64** [3] 230-44 (2005).
  59. M. Tadie, S. Liu, R. Robert, P. Guiheneuc, Y. Pereon, B. Perrouin-Verbe, and J. F. Mathe, "Partial Return of Motor Function in Paralyzed Legs after Surgical Bypass of the Lesion Site by Nerve Autografts Three Years after Spinal Cord Injury," *J Neurotrauma*, **19** [8] 909-16 (2002).
  60. C. Lima, P. Escada, J. Pratas-Vital, C. Branco, C. A. Arcangeli, G. Lazzeri, C. A. Maia, C. Capucho, A. Hasse-Ferreira, and J. D. Peduzzi, "Olfactory Mucosal Autografts and Rehabilitation for Chronic Traumatic Spinal Cord Injury," *Neurorehabil Neural Repair*, **24** [1] 10-22 (2010).
  61. N. N. Madigan, S. McMahon, T. O'Brien, M. J. Yaszemski, and A. J. Windebank, "Current Tissue Engineering and Novel Therapeutic Approaches to Axonal Regeneration Following Spinal Cord Injury Using Polymer Scaffolds," *Respir Physiol Neurobiol*, **169** [2] 183-99 (2009).
  62. D. E. Discher, P. Janmey, and Y. L. Wang, "Tissue Cells Feel and Respond to the Stiffness of Their Substrate," *Science*, **310** [5751] 1139-43 (2005).
  63. L. F. Reynolds, M. C. Bren, B. C. Wilson, G. D. Gibson, M. S. Shoichet, and R. J. L. Murphy, "Transplantation of Porous Tubes Following Spinal Cord Transection Improves Hindlimb Function in the Rat," *Spinal Cord*, **46** [1] 58-64 (2008).
  64. M. J. Moore, J. A. Friedman, E. B. Lewellyn, S. M. Mantila, A. J. Krych, S. Ameenuddin, A. M. Knight, L. Lu, B. L. Currier, R. J. Spinner, R. W. Marsh, A. J. Windebank, and M. J. Yaszemski, "Multiple-Channel Scaffolds to Promote Spinal Cord Axon Regeneration," *Biomaterials*, **27** [3] 419-29 (2006).
  65. A. Khademhosseini and R. Langer, "Microengineered Hydrogels for Tissue Engineering," *Biomaterials*, **28** [34] 5087-92 (2007).
  66. L. E. Kokai, A. M. Ghaznavi, and K. G. Marra, "Incorporation of Double-Walled Microspheres into Polymer Nerve Guides for the Sustained Delivery of Glial Cell Line-Derived Neurotrophic Factor," *Biomaterials*, **31** [8] 2313-22 (2010).
  67. S. Madduri and B. Gander, "Growth Factor Delivery Systems and Repair Strategies for Damaged Peripheral Nerves," *J Control Release*, **161** [2] 274-82 (2012).

68. S. Bunting, L. Di Silvio, S. Deb, and S. Hall, "Bioresorbable Glass Fibres Facilitate Peripheral Nerve Regeneration," *J Hand Surg*, **30B** [3] 242-7 (2005).
69. P. Nagaraja Upadhyaya and G. Kishore, "Glass Ionomer Cement – the Different Generations," *Trends Biomater Artif Organs*, **18** [2] 158-65 (2005).
70. S. G. Griffin and R. G. Hill, "Influence of Glass Composition on the Properties of Glass Polyalkenoate Cements. Part I: Influence of Aluminium to Silicon Ratio," *Biomaterials*, **20** [17] 1579-86 (1999).
71. H. W. Roberts, K. S. Vandewalle, and D. G. Berzins, "Fracture Resistance of Amalgam/Glass-Polyalkenoate Open Sandwich Class II Restorations: An in Vitro Study," *J Dent*, **36** [11] 873-7 (2008).
72. O. Clarkin, D. Boyd, and M. R. Towler, "Strontium-Based Glass Polyalkenoate Cements for Luting Applications in the Skeleton," *J Biomater Appl*, **24** [6] 483-502 (2010).
73. G. Lewis, Towler M.R., Boyd D., German M.J., Wren A.W., Clarkin O.M., Yates A. , "Evaluation of Two Novel Aluminum-Free, Zinc-Based Glass Polyalkenoate Cements as Alternatives to Pmma Bone Cement for Use in Vertebroplasty and Balloon Kyphoplasty," *J Mater Sci Mater Med*, **21** [1] 59-66 (2010).
74. M. D. O'Donnell, P. L. Candarlioglu, C. A. Miller, E. Gentleman, and M. M. Stevens, "Materials Characterisation and Cytotoxic Assessment of Strontium-Substituted Bioactive Glasses for Bone Regeneration," *J Mater Chem*, **20** [40] 8934-41 (2010).
75. M. J. Tyas and M. F. Burrow, "Adhesive Restorative Materials: A Review," *Aust Dent J*, **49** [3] 112-21 (2004).
76. Y. Yoshida, B. VanMeerbeek, Y. Nakayama, J. Snauwaert, L. Hellemans, P. Lambrechts, G. Vanherle, and K. Wakasa, "Evidence of Chemical Bonding at Biomaterial-Hard Tissue Interfaces," *J Dent Res*, **79** [2] 709-14 (2000).
77. W. Gao, R. J. Smales, and M. S. Gale, "Fluoride Release/Uptake from Newer Glass-Ionomer Cements Used with the Art Approach," *Am J Dent*, **13** [4] 201-4 (2000).
78. A. Coughlan, D. Boyd, C. W. I. Douglas, and M. R. Towler, "Antibacterial Coatings for Medical Devices Based on Glass Polyalkenoate Cement Chemistry," *J Mater Sci Mater Med*, **19** [12] 3555-60 (2008).

79. D. Boyd, O. M. Clarkin, A. Wren and M. R. Towler, "Zinc-Based Glass Polyalkenoate Cements with Improved Setting Times and Mechanical Properties," *Acta Biomater*, **4** [2] 425-31 (2008).
80. J. Sawai, "Quantitative Evaluation of Antibacterial Activities of Metallic Oxide Powders (Zno, Mgo and Cao) by Conductimetric Assay," *J Microbiol Methods*, **54** [2] 177-82 (2003).
81. P. Whittaker, "Iron and Zinc Interactions in Humans," *Am J Clin Nutr*, **68** [S] 442S-6S (1998).
82. D. Boyd, M. R. Towler, A. Wren and O. M. Clarkin, "Comparison of an Experimental Bone Cement with Surgical Simplex P, Spineplex and Cortoss," *J Mater Sci Mater Med*, **19** [4] 1745-52 (2008).
83. P. J. Marie, "Strontium Ranelate: A Physiological Approach for Optimizing Bone Formation and Resorption," *Bone*, **38** [2, Supplement 1] 10-4 (2006).
84. W. Cao and L. L. Hench, "Bioactive Materials," *Ceram Int*, **22** [19] 439-507 (1996).
85. J. Van der Stok, E. M. M. Van Lieshout, Y. El-Massoudi, G. H. Van Kralingen and P. Patka, "Bone Substitutes in the Netherlands - a Systematic Literature Review," *Acta Biomater*, **7** [2] 739-50 (2011).
86. L. A. Jeans, T. Gilchrist, and D. Healy, "Peripheral Nerve Repair by Means of a Flexible Biodegradable Glass Fibre Wrap: A Comparison with Microsurgical Epineurial Repair," *J Plast Reconstr Aes*, **60** [12] 1302-8 (2007).
87. Reproduced from A. Tilocca, "Models of Structure, Dynamics and Reactivity of Bioglasses: A Review," *J Mater Chem*, **20** [33] 6848-58 (2010) with permission of THE Royal Society of Chemistry.
88. W. D. Kingery, H. K. Bowen, and D. R. Uhlmann, "Structure of Glasses"; pp. 91-123 in *The Science and Technology of Materials, Introduction to Ceramics*. Wiley-Interscience, New York, 3, 1976.
89. R. Mathew, B. Stevansson, A. Tilocca, and M. Edén, "Toward a Rational Design of Bioactive Glasses with Optimal Structural Features: Composition–Structure Correlations Unveiled by Solid-State Nmr and Md Simulations," *J Phys Chem B*, **118** [3] 833-44 (2014).
90. J. M. Oliveira, R. N. Correia, and M. H. Fernandes, "Effects of Si Speciation on the in Vitro Bioactivity of Glasses," *Biomaterials*, **23** [2] 371-9 (2002).

91. I. Elgayar, A. E. Aliev, A. R. Boccaccini, and R. G. Hill, "Structural Analysis of Bioactive Glasses," *J Non-Cryst Solids*, **351** [2] 173-83 (2005).
92. R. G. Hill and D. S. Brauer, "Predicting the Bioactivity of Glasses Using the Network Connectivity or Split Network Models," *J Non-Cryst Solids*, **357** [24] 3884-7 (2011).
93. J. Massera, L. Hupa, and M. Hupa, "Influence of the Partial Substitution of Cao with Mgo on the Thermal Properties and in Vitro Reactivity of the Bioactive Glass S53p4," *J Non-Cryst Solids*, **358** [18–19] 2701-7 (2012).
94. J. Massera and L. Hupa, "Influence of Sro Substitution for Cao on the Properties of Bioactive Glass S53p4," *J Mater Sci Mater Med*, **25** [3] 657-68 (2014).
95. L.-C. Gerhardt and A. R. Boccaccini, "Bioactive Glass and Glass-Ceramic Scaffolds for Bone Tissue Engineering," *Materials*, **3** [7] 3867 (2010).
96. M. Cerruti, D. Greenspan, and K. Powers, "Effect of Ph and Ionic Strength on the Reactivity of Bioglass® 45s5," *Biomaterials*, **26** [14] 1665-74 (2005).
97. L. L. Hench, "Bioceramics: From Concept to Clinic," *J Amer Ceram Soc*, **74** [7] 1487-510 (1991).
98. A. Bigi, G. Cojazzi, S. Panzavolta, A. Ripamonti, N. Roveri, M. Romanello, K. Noris Suarez, and L. Moro, "Chemical and Structural Characterization of the Mineral Phase from Cortical and Trabecular Bone," *J Inorg Biochem*, **68** [1] 45-51 (1997).
99. J. E. Shelby, *Introduction to Glass Science and Technology*, 2nd ed.; p. 291. Royal Society of Chemistry, Cambridge, UK, 2005.
100. S. Ali, I. Farooq, and K. Iqbal, "A Review of the Effect of Various Ions on the Properties and the Clinical Applications of Novel Bioactive Glasses in Medicine and Dentistry," *The Saudi Dental Journal*, **26** [1] 1-5 (2014).
101. A. Hoppe, N. S. Güldal, and A. R. Boccaccini, "A Review of the Biological Response to Ionic Dissolution Products from Bioactive Glasses and Glass-Ceramics," *Biomaterials*, **32** [11] 2757-74 (2011).
102. G. F. Van Landeghem, M. E. De Broe, and P. C. D'Haese, "Al and Si: Their Speciation, Distribution, and Toxicity," *Clinical Biochemistry*, **31** [5] 385-97 (1998).
103. R. Jugdaohsingh, "Silicon and Bone Health," *J Nutr Health Aging*, **11** [2] 99-110 (2007).

104. E. M. Carlisle, "Silicon: A Possible Factor in Bone Calcification," *Science*, **167** [3916] 279-80 (1970).
105. D. M. Reffitt, N. Ogston, R. Jugdaohsingh, H. F. J. Cheung, B. A. J. Evans, R. P. H. Thompson, J. J. Powell, and G. N. Hampson, "Orthosilicic Acid Stimulates Collagen Type 1 Synthesis and Osteoblastic Differentiation in Human Osteoblast-Like Cells in Vitro," *Bone*, **32** [2] 127-35.
106. M.-H. Kim, Y.-J. Bae, M.-K. Choi, and Y.-S. Chung, "Silicon Supplementation Improves the Bone Mineral Density of Calcium-Deficient Ovariectomized Rats by Reducing Bone Resorption," *Biol Trace Elem Res*, **128** [3] 239-47 (2008).
107. J. E. Gough, J. R. Jones, and L. L. Hench, "Nodule Formation and Mineralisation of Human Primary Osteoblasts Cultured on a Porous Bioactive Glass Scaffold," *Biomaterials*, **25** [11] 2039-46 (2004).
108. S. Plettinck, L. Chou, and R. Wollast, "Kinetics and Mechanisms of Dissolution of Silica at Room Temperature and Pressure," *Mineral Mag A*, **58** 728-9 (1994).
109. L. S. Dent Glasser and N. Kataoka, "The Chemistry of 'Alkali-Aggregate' Reaction," *Cement Concrete Res*, **11** [1] 1-9 (1981).
110. T. Kokubo and H. Takadama, "How Useful Is Sbf in Predicting in Vivo Bone Bioactivity?," *Biomaterials*, **27** [15] 2907-15 (2006).
111. M. P. Blaustein and W. J. Lederer, "Sodium/Calcium Exchange: Its Physiological Implications," *Physiol Rev*, **79** [3] 763-854 (1999).
112. R. M. Reynolds, P. L. Padfield, and J. R. Seckl, "Disorders of Sodium Balance," *Brit Med J*, **332** [7543] 702-5 (2006).
113. S. Pors Nielsen, "The Biological Role of Strontium," *Bone*, **35** [3] 583-8 (2004).
114. M. D. O'Donnell and R. G. Hill, "Influence of Strontium and the Importance of Glass Chemistry and Structure When Designing Bioactive Glasses for Bone Regeneration," *Acta Biomater*, **6** [7] 2382-5 (2010).
115. D. Cacaina, H. Ylanen, M. Hupa, and S. Simon, "Study of Yttrium Containing Bioactive Glasses Behaviour in Simulated Body Fluid.," *J Mater Sci Mater Med*, **17** [8] 709-16 (2006).
116. C. Leonelli, G. Lusvardi, G. Malavasi, L. Menabue, and M. Tonelli, "Synthesis and Characterization of Cerium-Doped Glasses and in Vitro Evaluation of Bioactivity," *J Non-Cryst Solids*, **316** [2-3] 198-216 (2003).

117. H. Owada, K. Yamashita, T. Umegaki, T. Kanazawa, and M. Nagai, "Humidity-Sensitivity of Yttrium Substituted Apatite Ceramics," *Solid State Ionics*, **35** [3–4] 401-4 (1989).
118. B. A. E. Ben-Arfa, "Diopside-Calcium Pyrophosphate Bioglasses Doped with Some Additives"; Master in Biomedical Materials Thesis. University of Aveiro, University of Aveiro, 2011.
119. L. Lefebvre, J. Chevalier, L. Gremillard, R. Zenati, G. Thollet, D. Bernache-Assolant, and A. Govin, "Structural Transformations of Bioactive Glass 45s5 with Thermal Treatments," *Acta Materialia*, **55** [10] 3305-13 (2007).
120. Q. Z. Chen, I. D. Thompson, and A. R. Boccaccini, "45s5 Bioglass®-Derived Glass–Ceramic Scaffolds for Bone Tissue Engineering," *Biomaterials*, **27** [11] 2414-25 (2006).
121. D. C. Clupper and L. L. Hench, "Crystallization Kinetics of Tape Cast Bioactive Glass 45s5," *J Non-Cryst Solids*, **318** [1–2] 43-8 (2003).
122. O. Bretcanu, X. Chatzistavrou, K. Paraskevopoulos, R. Conradt, I. Thompson, and A. R. Boccaccini, "Sintering and Crystallisation of 45s5 Bioglass® Powder," *J Euro Ceram Soc*, **29** [16] 3299-306 (2009).
123. M. Oscar Prado, E. Dutra Zanotto, and R. Müller, "Model for Sintering Polydispersed Glass Particles," *J Non-Cryst Solids*, **279** [2–3] 169-78 (2001).
124. H. A. ElBatal, M. A. Azooz, E. M. A. Khalil, A. Soltan-Monem, and Y. M. Hamdy, "Characterization of Some Bioglass–Ceramics," *Mater Chem Phy*, **80** [3] 599-609 (2003).
125. D. C. Clupper, J. J. Mecholsky Jr, G. P. LaTorre, and D. C. Greenspan, "Bioactivity of Tape Cast and Sintered Bioactive Glass-Ceramic in Simulated Body Fluid," *Biomaterials*, **23** [12] 2599-606 (2002).
126. O. Peitl Filho, G. P. LaTorre, and L. L. Hench, "Effect of Crystallization on Apatite-Layer Formation of Bioactive Glass 45s5," *J Biomed Mater Res*, **30** [4] 509-14 (1996).
127. O. Peitl, E. Dutra Zanotto, and L. L. Hench, "Highly Bioactive P2o5–Na2o–Cao–Sio2 Glass-Ceramics," *J Non-Cryst Solids*, **292** [1–3] 115-26 (2001).
128. B. D. Boyan, T. W. Hummert, D. D. Dean, and Z. Schwartz, "Role of Material Surfaces in Regulating Bone and Cartilage Cell Response," *Biomaterials*, **17** [2] 137-46 (1996).

129. K. C. Dee, D. A. Puleo, and R. Bizios, "Biomaterial Surfaces and the Physiological Environment"; pp. 149-72 in *An Introduction to Tissue-Biomaterial Interactions*. John Wiley & Sons, Inc., 2003.
130. P. T. Ohara and R. C. Buck, "Contact Guidance in Vitro: A Light, Transmission, and Scanning Electron Microscopic Study," *Exp Cell Res*, **121** [2] 235-49 (1979).
131. P. Clark, P. Connolly, A. S. Curtis, J. A. Dow, and C. D. Wilkinson, "Topographical Control of Cell Behaviour: Ii. Multiple Grooved Substrata," *Development*, **108** [4] 635-44 (1990).
132. V. Karageorgiou and D. Kaplan, "Porosity of 3d Biomaterial Scaffolds and Osteogenesis," *Biomaterials*, **26** [27] 5474-91 (2005).
133. K. T. Bowers, J. C. Keller, B. A. Randolph, D. G. Wick, and C. M. Michaels, "Optimization of Surface Micromorphology for Enhanced Osteoblast Responses in Vitro," *Int J Oral Max Impl*, **7** [3] 302-10 (1992).
134. P. Li, C. Ohtsuki, T. Kokubo, K. Nakanishi, N. Soga, T. Nakamura, and T. Yamamuro, "Apatite Formation Induced by Silica Gel in a Simulated Body Fluid," *J Am Ceram Soc*, **75** [8] 2094-7 (1992).
135. W. Norde, "The Behavior of Proteins at Interfaces, with Special Attention to the Role of the Structure Stability of the Protein Molecule," *Clinical Materials*, **11** [1-4] 85-91 (1992).
136. N. Olmo, Martí, amp, x, A. I. n, A. J. Salinas, J. Turnay, R. Vallet, Marí, and M. A. Lizarbe, "Bioactive Sol-Gel Glasses with and without a Hydroxycarbonate Apatite Layer as Substrates for Osteoblast Cell Adhesion and Proliferation," *Biomaterials*, **24** [20] 3383-93 (2003).
137. A. W. Wren, A. Coughlan, K. E. Smale, S. T. Mixture, B. P. Mahon, O. M. Clarkin, and M. R. Towler, "Fabrication of Cao-Nao-Sio2/Tio2 Scaffolds for Surgical Applications," *J Mater Sci Mater Med*, **23** [12] 2881-91 (2012).
138. J. Serra, P. González, S. Liste, C. Serra, S. Chiussi, B. León, M. Pérez-Amor, H. O. Ylänen, and M. Hupa, "Ftir and Xps Studies of Bioactive Silica Based Glasses," *J Non-Cryst Solids*, **332** [1-3] 20-7 (2003).
139. M. Vallet-Regi, A. J. Salinas, J. Roman, and M. Gil, "Effect of Magnesium Content on the in Vitro Bioactivity of Cao-Mgo-Sio2-P2o5 Sol-Gel Glasses," *J Mater Chem*, **9** [2] 515-8 (1999).
140. A. W. Wren, A. Coughlan, L. Placek, and M. R. Towler, "Gallium Containing Glass Polyalkenoate Anti-Cancerous Bone Cements: Glass Characterization and Physical Properties," *J Mater Sci Mater Med*, **23** [8] 1823-33 (2012).

141. T. J. Keenan, L. M. Placek, T. L. McGinnity, M. R. Towler, M. M. Hall, and A. W. Wren, "Relating Ion Release and Ph to in Vitro Cell Viability for Gallium-Inclusive Bioactive Glasses," *J Mater Sci*, **51** [2] 1107-20 (2016).
142. A. A. Gorustovich, T. Steimetz, R. L. Cabrini, and J. M. Porto Lopez, "Osteoconductivity of Strontium-Doped Bioactive Glass Particles: A Histomorphometric Study in Rats," *J Biomed Mater Res A*, **92** [1] 232-7 (2010).
143. S. G. Griffin and R. G. Hill, "Influence of Glass Composition on the Properties of Glass Polyalkenoate Cements. Part I: Influence of Aluminium to Silicon Ratio," *Biomaterials*, **20** [17] 1579-86 (1999).
144. V. Miguez-Pacheco, L. L. Hench, and A. R. Boccaccini, "Bioactive Glasses Beyond Bone and Teeth: Emerging Applications in Contact with Soft Tissues," *Acta Biomater*, **13** [0] 1-15 (2015).
145. S. Kehoe, X. F. Zhang, and D. Boyd, "Fda Approved Guidance Conduits and Wraps for Peripheral Nerve Injury: A Review of Materials and Efficacy," *Injury*, **43** [5] 553-72 (2012).
146. R. Midha, "Emerging Techniques for Nerve Repair: Nerve Transfers and Nerve Guidance Tubes," *Clin Neur*, **53** 185-90 (2006).
147. P. J. Marie, P. Ammann, G. Boivin, and C. Rey, "Mechanisms of Action and Therapeutic Potential of Strontium in Bone," *Calcif Tissue Int*, **69** [3] 121-9 (2001).
148. M. Das, S. Patil, N. Bhargava, J.-F. Kang, L. M. Riedel, S. Seal, and J. J. Hickman, "Auto-Catalytic Ceria Nanoparticles Offer Neuroprotection to Adult Rat Spinal Cord Neurons," *Biomaterials*, **28** [10] 1918-25 (2007).
149. L. M. Marquardt, D. Day, S. E. Sakiyama-Elbert, and A. B. Harkins, "Effects of Borate-Based Bioactive Glass on Neuron Viability and Neurite Extension," *J Biomed Mater Res A*, **102** [8] 2767-75 (2014).
150. R. G. Hill and D. S. Brauer, "Predicting the Glass Transition Temperature of Bioactive Glasses from Their Molecular Chemical Composition," *Acta Biomater*, **7** [10] 3601-5 (2011).
151. M. D. O'Donnell, "Predicting Bioactive Glass Properties from the Molecular Chemical Composition: Glass Transition Temperature," *Acta Biomater*, **7** [5] 2264-9 (2011).
152. P. Zhang, C. Dunlap, P. Florian, P. J. Grandinetti, I. Farnan, and J. F. Stebbins, "Silicon Site Distributions in an Alkali Silicate Glass Derived by Two-

- Dimensional  $^{29}\text{Si}$  Nuclear Magnetic Resonance," *J Non-Cryst Solids*, **204** [3] 294-300 (1996).
153. M. W. G. Lockyer, D. Holland, and R. Dupree, "Nmr Investigation of the Structure of Some Bioactive and Related Glasses," *J Non-Cryst Solids*, **188** [3] 207-19 (1995).
  154. L. Marsich, L. Moimas, V. Sergo, and C. Schmid, "Raman Spectroscopic Study of Bioactive Silica-Based Glasses; the Role of the Alkali/Alkali Earth Ratio on the Non-Bridging Oxygen/Bridging Oxygen (Nbo/Bo) Ratio," *Spectroscopy*, **23** [3-4] (2009).
  155. H. B. Wang, M. E. Mullins, J. M. Cregg, C. W. McCarthy, and R. J. Gilbert, "Varying the Diameter of Aligned Electrospun Fibers Alters Neurite Outgrowth and Schwann Cell Migration," *Acta Biomater*, **6** [8] 2970-8 (2010).
  156. E. Yildirim and R. Dupree, "Investigation of Al–O–Al Sites in an Na-Aluminosilicate Glass," *Bull Mater Sci*, **27** [3] 269-72 (2004).
  157. A. W. Wren, T. Keenan, A. Coughlan, F. R. Laffir, D. Boyd, M. R. Towler, and M. M. Hall, "Characterisation of  $\text{Ga}_2\text{O}_3\text{--Na}_2\text{O--CaO--ZnO--SiO}_2$  Bioactive Glasses," *J Mater Sci*, **48** [11] 3999-4007 (2013).
  158. J. Du, L. Kokou, J. L. Rygel, Y. Chen, C. G. Pantano, R. Woodman, and J. Belcher, "Structure of Cerium Phosphate Glasses: Molecular Dynamics Simulation," *J Amer Ceram Soc*, **94** [8] 2393-401 (2011).
  159. T. Schaller and F. J. Stebbins, "The Structural Role of Lanthanum and Yttrium in Aluminosilicate Glasses: A  $^{27}\text{Al}$  and  $^{17}\text{O}$  Mas Nmr Study," *J Phys Chem B*, **102** [52] 10690-7 (1998).
  160. J. K. Christie and A. Tilocca, "Short-Range Structure of Yttrium Alumino-Silicate Glass for Cancer Radiotherapy: Car-Parrinello Molecular Dynamics Simulations," *Adv Eng Mater*, **12** [7] B326-B30 (2010).
  161. J. K. Christie, R. I. Ainsworth, and N. H. de Leeuw, "Investigating Structural Features Which Control the Dissolution of Bioactive Phosphate Glasses: Beyond the Network Connectivity," *J Non-Cryst Solids*, **In Press** (2015).
  162. J. R. Jones, "Review of Bioactive Glass: From Hench to Hybrids," *Acta Biomater*, **9** [1] 4457-86 (2013).
  163. J. K. Christie and A. Tilocca, "Aluminosilicate Glasses as Yttrium Vectors for in Situ Radiotherapy: Understanding Composition-Durability Effects through Molecular Dynamics Simulations," *Chem Mater*, **22** [12] 3725-34 (2010).

164. J. K. Christie, J. Malik, and A. Tilocca, "Bioactive Glasses as Potential Radioisotope Vectors for in Situ Cancer Therapy: Investigating the Structural Effects of Yttrium," *Phys Chem Chem Phys*, **13** [39] 17749-55 (2011).
165. D. Cacaina, H. Ylanen, S. Simon, and M. Hupa, "The Behaviour of Selected Yttrium Containing Bioactive Glass Microspheres in Simulated Body Environments," *J Mater Sci Mater Med*, **19** [3] 1225-33 (2008).
166. F. J. B. Calleja, D. S. Sanditov, and V. P. Privalko, "Review: The Microhardness of Non-Crystalline Materials," *J Mater Sci*, **37** [21] 4507-16 (2002).
167. M. M. Smedskjaer, "Topological Model for Boroaluminosilicate Glass Hardness," *Front Mater*, **1** (2014).
168. M. M. Smedskjaer, J. C. Mauro, and Y. Yue, "Prediction of Glass Hardness Using Temperature-Dependent Constraint Theory," *Phys Rev Lett*, **105** [11] 115503 (2010).
169. M. Magi, E. Lippmaa, A. Samoson, G. Engelhardt, and A. R. Grimmer, "Solid-State High-Resolution Silicon-29 Chemical Shifts in Silicates," *J Phy Chem*, **88** [8] 1518-22 (1984).
170. S. Gavarini, M. J. Guittet, P. Trocellier, M. Gautier-Soyer, F. Carrot, and G. Matzen, "Cerium Oxidation During Leaching of Ceysialo Glass," *J Nucl Mater*, **322** [2-3] 111-8 (2003).
171. V. 4.1. NIST X-ray Photoelectron Spectroscopy Database (National Institute of Standards and Technology, Gaithersburg, 2012).
172. G. P. Serra J., Liste S., Chiussi S., León B., Pérez-Amor M., Ylänen H. O., Hupa M., "Influence of the Non-Bridging Oxygen Groups on the Bioactivity of Silicate Glasses," *J Mater Sci Mater Med*, **13** [12] 1221-5 (2002).
173. L. M. Jurkić, I. Cepanec, S. K. Pavelić, and K. Pavelić, "Biological and Therapeutic Effects of Ortho-Silicic Acid and Some Ortho-Silicic Acid-Releasing Compounds: New Perspectives for Therapy," *Nutr Metab*, **10** [2] 1-12 (2013).
174. K. Blinzinger and G. Kreutzberg, "Displacement of Synaptic Terminals from Regenerating Motoneurons by Microglial Cells," *Z Zellforsch Mikrosk Anat*, **85** [2] 145-57 (1968).
175. Y. Zeng, M. Xiong, H. Yu, N. He, Z. Wang, Z. Liu, H. Han, and S. Chen, "Clinical Effect of Methylprednisolone Sodium Succinate and Mouse Nerve Growth Factor for Injection in Treating Acute Spinal Cord Injury and Cauda Equina Injury," *Zhongguo Xiu Fu Chong Jian Wai Ke Za Zhi*, **24** [10] 1208-11 (2010).

176. Y. Xiao and A. C. Lasaga, "Ab Initio Quantum Mechanical Studies of the Kinetics and Mechanisms of Quartz Dissolution:  $\text{OH}^-$  Catalysis," *Geochim Cosmochim Acta*, **60** [13] 2283-95 (1996).
177. B. A. Fleming, "Kinetics of Reaction between Silicic Acid and Amorphous Silica Surfaces in NaCl Solutions," *J Colloid Interf Sci*, **110** [1] 40-64 (1986).
178. H. P. Rothbaum and A. G. Rohde, "Kinetics of Silica Polymerization and Deposition from Dilute Solutions between 5 and 180°C," *J Colloid Interf Sci*, **71** [3] 533-59 (1979).
179. G. A. Icopini, S. L. Brantley, and P. J. Heaney, "Kinetics of Silica Oligomerization and Nanocolloid Formation as a Function of Ph and Ionic Strength at 25°C," *Geochim Cosmochim Acta*, **69** [2] 293-303 (2005).
180. S. H. Chan, "A Review on Solubility and Polymerization of Silica," *Geothermics*, **18** [1] 49-56 (1989).
181. R. Mandal, A. C. Guo, K. K. Chaudhary, P. Liu, F. S. Yallou, E. Dong, F. Aziat, and D. S. Wishart, "Multi-Platform Characterization of the Human Cerebrospinal Fluid Metabolome: A Comprehensive and Quantitative Update," *Genome Med*, **4** [4] 38- (2012).
182. S. C. Verberckmoes, M. E. De Broe, and P. C. D'Haese, "Dose-Dependent Effects of Strontium on Osteoblast Function and Mineralization," *Kidney Int*, **64** [2] 534-43 (2003).
183. P. Valerio, M. M. Pereira, A. M. Goes, and M. F. Leite, "The Effect of Ionic Products from Bioactive Glass Dissolution on Osteoblast Proliferation and Collagen Production," *Biomaterials*, **25** [15] 2941-8 (2004).
184. Y. C. Fredholm, N. Karpukhina, D. S. Brauer, J. R. Jones, R. V. Law, and R. G. Hill, "Influence of Strontium for Calcium Substitution in Bioactive Glasses on Degradation, Ion Release and Apatite Formation," *J R Soc Interface*, **9** [70] 880-9 (2012).
185. I. A. Silver, J. Deas, and M. Erecińska, "Interactions of Bioactive Glasses with Osteoblasts in Vitro: Effects of 45s5 Bioglass®, and 58s and 77s Bioactive Glasses on Metabolism, Intracellular Ion Concentrations and Cell Viability," *Biomaterials*, **22** [2] 175-85 (2001).
186. P. Small, D. Blankenhorn, D. Welty, E. Zinser, and J. L. Slonczewski, "Acid and Base Resistance in Escherichia Coli and Shigella Flexneri: Role of Rpos and Growth Ph," *J Bacteriol*, **176** [6] 1729-37 (1994).

187. N. M. Parhad and N. U. Rao, "Effect of Ph on Survival of Escherichia Coli," *J Water Pollut Control Fed*, **46** [5] 980-6 (1974).
188. A. C. Baird-Parker, "The Staphylococci: An Introduction," *Soc Appl Bacteriol Symp Ser*, **19** 1S-8S (1990).
189. R. C. Whiting, S. Sackitey, S. Calderone, K. Morely, and J. G. Phillips, "Model for the Survival of Staphylococcus Aureus in Nongrowth Environments," *Int J Food Microbiol*, **31** [1-3] 231-43 (1996).
190. M. I. Halpin-Dohnalek and E. H. Marth, "Staphylococcus Aureus: Production of Extracellular Compounds and Behavior in Foods : A Review," *J Food Protect AGRIS*, **52** [4] (1989).
191. A. Jøssang and E. Stange, "A New Predictive Activity Model for Aqueous Salt Solutions," *Fluid Phase Equilibr*, **181** [1-2] 33-46 (2001).
192. B. J. Marshall, D. F. Ohye, and J. H. B. Christian, "Tolerance of Bacteria to High Concentrations of Nacl and Glycerol in the Growth Medium," *Appl Microbiol*, **21** [2] 363-4 (1971).
193. E. R. Olson, "Influence of Ph on Bacterial Gene Expression," *Mol Microbiol*, **8** [1] 5-14 (1993).
194. S. A. Greenberg and D. Sinclair, "The Polymerization of Silicic Acid," *J Phys Chem*, **59** [5] 435-40 (1955).
195. K. Goto, "Effect of Ph on Polymerization of Silicic Acid," *J Phys Chem*, **60** [7] 1007-8 (1956).
196. T. Coradin and J. Livage, "Effect of Some Amino Acids and Peptides on Silicic Acid Polymerization," *Colloid Surface B*, **21** [4] 329-36 (2001).
197. M. Preari, K. Spinde, J. Lazic, E. Brunner, and K. D. Demadis, "Bioinspired Insights into Silicic Acid Stabilization Mechanisms: The Dominant Role of Polyethylene Glycol-Induced Hydrogen Bonding," *J Am Chem Soc*, **136** [11] 4236-44 (2014).
198. L. Placek and A. W. Wren, "Characterization and Solubility of Y2O3 and CeO2 Containing Bioactive Glasses to Aid Spinal Cord Recovery "; in *NEBEC Conference Proceedings* 2014.
199. L. Placek and A. Wren, "Cytocompatibility of Y2O3 and CeO2 Containing Bioactive Glasses to Aid Spinal Cord Recovery"; in *NEBEC Conference Proceedings* 2015.

200. A. A. El-Kheshen, F. A. Khaliifa, E. A. Saad, and R. L. Elwan, "Effect of Al<sub>2</sub>O<sub>3</sub> Addition on Bioactivity, Thermal and Mechanical Properties of Some Bioactive Glasses," *Ceram Int*, **34** [7] 1667-73 (2008).
201. E. Gentleman, Y. C. Fredholm, G. Jell, N. Lotfibakhshaiesh, M. D. O'Donnell, R. G. Hill, and M. M. Stevens, "The Effects of Strontium-Substituted Bioactive Glasses on Osteoblasts and Osteoclasts in Vitro," *Biomaterials*, **31** [14] 3949-56 (2010).
202. L. M. Placek, T.J. Keenan, F. Laffir, A. Coughlan, A.W. Wren, "Characterization of Y<sub>2</sub>O<sub>3</sub> and CeO<sub>2</sub> Doped SiO<sub>2</sub>-SrO-Na<sub>2</sub>O Bioactive Glasses," *Biomedical Glasses*, **1** [1] (2015).
203. M. Bains and E. D. Hall, "Antioxidant Therapies in Traumatic Brain and Spinal Cord Injury," *BBA-Mol Basis Dis*, **1822** [5] 675-84 (2012).
204. A. Y. Estevez, S. Pritchard, K. Harper, J. W. Aston, A. Lynch, J. J. Lucky, J. S. Ludington, P. Chatani, W. P. Mosenthal, J. C. Leiter, S. Andreescu, and J. S. Erlichman, "Neuroprotective Mechanisms of Cerium Oxide Nanoparticles in a Mouse Hippocampal Brain Slice Model of Ischemia," *Free Radical Biol Med*, **51** [6] 1155-63 (2011).
205. Z.-P. Li, T. Mori, F. Ye, D. Ou, G. J. Auchterlonie, J. Zou, and J. Drennan, "Cerium-Reduction-Induced Defects Clustering, Ordering, and Associated Microstructure Evolution in Yttrium-Doped Ceria," *J Phys Chem C*, **116** [9] 5435-43 (2012).
206. D. Marrocchelli, S. R. Bishop, H. L. Tuller, and B. Yildiz, "Understanding Chemical Expansion in Non-Stoichiometric Oxides: Ceria and Zirconia Case Studies," *Adv Funct Mater*, **22** [9] 1958-65 (2012).
207. J. Qian, Y. Kang, Z. Wei, and W. Zhang, "Fabrication and Characterization of Biomimetic 45S5 Bioglass Scaffold from Sugarcane," *Mater Sci Eng C*, **29** [4] 1361-4 (2009).
208. L.-C. Huang, C.-C. Lin, and P. Shen, "Crystallization and Stoichiometry of Crystals in Na<sub>2</sub>CaSi<sub>2</sub>O<sub>6</sub>-P<sub>2</sub>O<sub>5</sub> Based Bioactive Glasses," *Mater Sci Eng A*, **452-453** 326-33 (2007).
209. L. R. Pinckney and G. H. Beall, "Microstructural Evolution in Some Silicate Glass-Ceramics: A Review," *J Am Ceram Soc*, **91** [3] 773-9 (2008).
210. D. Cacaina, H. Ylanen, M. Hupa, and S. Simon, "Study of Yttrium Containing Bioactive Glasses Behaviour in Simulated Body Fluid.," *Journal of Materials Science: Materials in Medicine*, **17** [8] 709-16 (2006).

211. G. J. Howard and P. McConnell, "Adsorption of Polymers at the Solution-Solid Interface. I. Polyethers on Silica," *J Phys Chem*, **71** [9] 2974-81 (1967).
212. S. Spange, Y. Zimmermann, and A. Graeser, "Hydrogen-Bond-Donating Acidity and Dipolarity/Polarizability of Surfaces within Silica Gels and Mesoporous Mcm-41 Materials," *Chem Mater*, **11** [11] 3245-51 (1999).
213. S. Spange and E. Vilsmeier, "Solvatochromic Studies on the Hydrogen-Bond Donating and Dipolarity/Polarizability Properties of the Polyethylene Oxide/Silica Interface," *Colloid Poly Sci*, **277** [7] 687-93.
214. S. Spange and A. Reuter, "Hydrogen-Bond Donating and Dipolarity/Polarizability Properties of Chemically Functionalized Silica Particles," *Langmuir*, **15** [1] 141-50 (1999).
215. A. Hurtado, J. M. Cregg, H. B. Wang, D. F. Wendell, M. Oudega, R. J. Gilbert, and J. W. McDonald, "Robust Cns Regeneration after Complete Spinal Cord Transection Using Aligned Poly-L-Lactic Acid Microfibers," *Biomaterials*, **32** [26] 6068-79 (2011).
216. L. Placek, T. Keenan, A. Coughlan, and A. Wren, "Solubility, Cytocompatibility and Antioxidant Capacity of Y<sub>2</sub>O<sub>3</sub> and CeO<sub>2</sub> Doped SiO<sub>2</sub>-SrO-Na<sub>2</sub>O Glasses," (Under Review 2016).
217. S. R. Radin and P. Ducheyne, "Effect of Bioactive Ceramic Composition and Structure on in Vitro Behavior. Iii. Porous Versus Dense Ceramics," *J Biomed Mater Res*, **28** [11] 1303-9 (1994).